

博士論文

**Gate-induced Superconductivity and
Nonreciprocal Transport in Chiral Nanotubes**

(カイラルナノチューブにおける電界誘起超伝導と非相反輸送現象)

秦 峰

Abstract

1. Introduction and motivation

Scaling down the dimensionality of a system is always interesting in the research field of condensed matter physics, due to various fascinating phases emerging from the competition between condensations and fluctuations. For instance, superconductivity, the most famous condensed phase in materials, shows totally different behaviors when scaling down the system dimensions and finally disappears in one dimension due to strong quantum fluctuations. Therefore, Two Dimensional (2D) superconductors in atomically thin metals, mechanically exfoliated 2D materials and various hetero interfaces recently have attracted lots of interest.

Beyond those 2D materials, nanotube (NT) should be a new platform for the nano-scaled superconductor because of its unique geometry with intermediate dimension. Moreover, compared with usual materials, NT has a distinct topology indicating novel properties originating from quantum interference along the NT circumference. The relations between geometry of materials and superconductivity are highly anticipated to yield unexpected quantum phenomena. Hence, the superconducting NT, once realized, will be a potential material for searching exotic phenomena and nontrivial superconductivity due to its uniqueness in geometry.

So far, the superconductivity in NTs has not been well-studied because of the lack of suitable materials. Although there are intensive studies of superconductivity in carbon NTs in the past years, those researches have only investigated properties of superconductivity in the assembled form of NTs. Until now the superconducting properties reflecting the unique geometry, such as curvature and chirality of individual NT, have remained elusive.

Above all, we are focusing on another NT made of tungsten disulfide (WS_2) based on three reasons. First, WS_2 NT is famous and well-characterized, because it is the first

inorganic NT synthesized in 1992, just one year after the birth of carbon NT. Second, WS_2 is a member of Transition Metal Dichalcogenides (TMDs) family, and TMD materials are currently thought to be 2D materials beyond graphene. Recently TMD materials are attracting significant attention because of novel properties and prospective applications for electronics, photonics, spin-tronics, mechanics as well as valley-tronics. Third, recent systematic studies have clarified that a lot of TMDs, including WS_2 , are semiconductors without carrier doping, exhibit superconductivity under the ionic liquid gating technique. Hence, WS_2 NT is a promising candidate to realize superconductivity with novel properties and broad applications in the future.

Thus, in this study, we have measured the transport properties of individual WS_2 NT under ionic liquid gating. From the perspective of material science, we aim to realize superconductivity in individual WS_2 NTs, and from the perspective of physics, we aim to clarify the novel properties arising from its peculiar tubular and chiral structure of WS_2 NTs.

2. Experiment and sample characterization

In the recent experimental advances of our study, by replacing the solid dielectric with polymer electrolyte or ionic gel/liquid, a new type of Field Effect Transistor (FET), called Electrical Double Layer Transistor (EDLT), has been demonstrated to have the capability to accumulate over ten times higher carrier density ($> 10^{14} \text{ cm}^{-2}$) even at low gate bias voltages, compare to the conventional solid gate FET. Such ionic liquid gating technique is a powerful technique to realize electrostatics doping onto the surface of sample, and thus manipulate electronic properties of sample. Very recently in our experiment, a new gate-induced electronic modulation technique has been realized and systematically studied. Beyond electrostatic carrier doping, it realizes electrochemical doping induced by ionic liquid gating, which demonstrated that the positive ions diffuse into the interlayer of the bulk materials and thus realizing extremely high carrier doping not onto the surface but into the whole bulk. Therefore, we adopted this novel gate-induced electronic modulation technique in our experiment.

We have performed transmission electron microscope image of a single WS_2 NT, in which the tube has multi-wall structure with an outer diameter ranging from tens to hundreds nanometers. According to previous work, the tube part has a $2H$ -polymorph-layered structure of WS_2 , where each tungsten atom is surrounded by six

sulfur atoms in trigonal bipyramid coordination (space group $P6_3/mmc$). From the electron diffraction pattern of a single WS_2 NT, most of tubes contain multi-type chirality.

3. Gate-induced superconductivity in individual NTs

In our study, the carrier density of WS_2 NT was successfully tuned by liquid gate technique, and a repeatable and reversible ambipolar transfer curve of the source drain current I_{ds} with a high on/off ratio ($>10^2$) was observed for both hole and electron sides. In addition to the electrostatic doping in EDL region, the electrochemical doping was realized. During the intercalation process, the source drain current I_{ds} increased more than two orders difference and the intercalated WS_2 NTs displayed well-metallic properties and thus performed superconductivity in low temperature. This is the first observation of superconductivity in individual NTs.

The anisotropic superconducting properties in individual WS_2 NT were also observed in our experiment. The superconductivity rapidly disappeared with the increase of the external magnetic field perpendicular to the NT axis, while the superconductivity was robust against the change of the external magnetic field in the parallel case. The anisotropic superconductivity was also confirmed by angular dependence and temperature dependence of the upper critical field. Besides the anisotropic properties of superconductivity, the possible staging phase and nontrivial pairing mechanism was also discussed. The results of our experiment could be inspiring for researchers to further explore new superconductors by ionic liquid gating, and offering them a great opportunity to investigate exotic properties originating from a peculiar structure.

4. Little-Parks oscillations and diameter-dependent of T_c

When the external magnetic field was applied parallel to the tube axis, the magnetoresistance at fix temperatures have shown the periodic oscillation during the superconducting transition, known as Little-Parks effect, originating from the quantum interference of the supercurrent along the circumference of NT and thus resultant oscillation of critical temperature, from which the diameter of certain NT was estimated. Our result provides solid evidence that the superconductivity occurs in the nanoscaled cylindrical structure, and attracts a great amount of interest in the superconducting NT.

Furthermore, our study of diameter-dependent of superconductivity is the first systematic study of superconducting NT research field, and was discussed by summarizing multiple observation of superconductivity in multiple tubes with different diameters. The critical temperature (T_c) of superconductivity decreases linearly as a function of the inverse diameter of the NT, which implies that the superconductivity is affected by the tube diameter, that is, curvature effect of the NT. By carefully ruling out other possibilities affecting T_c such as carrier density or wall thickness, the observed systematic relation is consequently considered as purely curvature effect of the NT. Our present results provide crucial information for understanding the microscopic origin of superconductivity in an individual NT.

5. Chirality and nonlinear transport properties

Our study is the first experimental discovery that is demonstrated on the nonreciprocity of superconductivity. An unambiguous evidence of the superconductivity reflecting chiral structure of NT was observed, in which the forward and backward supercurrent flows were not equivalent because of inversion symmetry breaking. The observed nonreciprocal signal was significantly enhanced within the superconducting state due to the highly coherence nature of superconductivity, and became negligibly small in the normal state. In addition, the nonreciprocal signal was associated with unprecedented quantum Little-Parks oscillation. Furthermore, it was interesting that the nonreciprocal signal displayed stepwise behavior at low temperature, affected by the flux quanta passing through the tube. Our current results could be inspiring for researchers to further pursue the research on the microscopic origin of nonreciprocal superconductivity and pairing symmetry in chiral or noncentrosymmetric structure.

6. Summary

In this study, basic superconducting properties of individual WS_2 NT are investigated. The study demonstrates of high performance of field effect on individual WS_2 NT by liquid gating technique, and discovers of a new type superconducting material. For the knowledge of basic physics, both the curvature effect and chirality effect on the superconductivity are revealed for the first time. In the view of wealthy family of materials, this study implies the TMD NT should be a new platform for the researches on nanoscaled devices beyond 2D TMD materials and carbon NT.

Acknowledgements

This thesis is a short summary of part of my experimental results in the past five years. I would not be possible to finalize it without the help and support from my advisor, lab members, my co-authors, and all of my friends surrounding me. Thus, I would like to highlight their kind help and support, and to express my deeply appreciation to all of them.

First of all, I would like to deliver my greatest thanks to Professor Yoshihiro Iwasa. In June, 2014, he visited to Tsinghua University for a workshop, and I was attracted by his presentation about the gate-induced superconductivity in layer materials. I highly appreciated that he offered me an opportunity to start my Ph.D. course under his supervision in the University of Tokyo after I graduated from Tsinghua University, and working on the gate-induced superconductivity in individual WS_2 NTs. He taught me a lot during my Ph.D. course, not only scientific knowledge, but also the method of critical thinking. There is one impressive sentence from him that I kept it in my mind, which is “Please think before doing experiment”. From his attitude toward science and research, I learned a lot of things. It is my great honor under his supervision.

Second, I would like to thank all of lab members. I highly appreciate to Dr. Wu Shi and Dr. Masaro Yoshida, that they taught me basic skill of device fabrication and transport measurement. Especially for Shi-san, he firstly realized gate-induced superconductivity in individual WS_2 NTs at the end of his stay here, which was the very beginning of this whole work. And I appreciate Dr. Toshiya Ideue, for the fruitful discussion and helpful guidance in both physics and writing skills. Also I appreciate Prof. Masaki Nakano, Dr. Yu Saito, Mr. Masaru Onga, Mr. Yuji Nagakawa, and Mr. Yue Wang, not only for their experimental assist, but also for their kind help in my daily life. As a foreign student here, I obtained great support from all the lab members. And thus I would like to thank to Ms. Keiko Yashima, Ms. Fumiko Yamaura, Dr. Yijin Zhang, Dr. Ryuji Suzuki, Mr. Shota Koshigawa, Mr. Hedeki Matsuoka, Mr. Yuki Itahashi, Mr. Takatoshi Akamatsu, Mr. Yuki Tanaka, Mr. Yuki Majima, Mr. Tatsuru Kubota, Mr. Ibuki Watanabe, Mr. Yu Dong, Ms. Chihiro Goto, Mr. Eimei Zaitzu, Mr. Yuta

Kashiwabara, Mr. Daiki Shin, Mr. Hiroaki Taiko, Mr. Takahiro Kurosu, Mr. Takashi Gokuden, Dr. Hiroki Shioya, Mr. Takahiko Iizuka, Mr. Takato Hada, Mr. Jun Miyazaki. It was a great pleasure for me to be a member in Iwasa group.

And then, I would like to thank to my co-authors, especially for Prof. Reshef Tenne, and Prof. Alla Zak. I appreciate that they sent us WS₂ NT sample for my experiment. And I highly appreciate their revision when I wrote the manuscript. They had revised my sentence to become more logical, carefully checked my mistake in grammar, and gave me important advice to improve my paper. I am also grateful to Prof. Daisuke Hashizume, Dr. Tomoka Kikitsu, and Dr. Daishi Inoue, for their great technique of transmission electron microscopy. Also I would like to thank to Dr. Xiao-xiao Zhang, for the fruitful discussion in theoretical physics and scientific computing. As a former student in this department, he also helped me a lot in my daily life in Tokyo.

Next, I would like to thank to all of my friends. Especially, I would like to think to all members of the basketball team TOKYO DELUXE. Most of them are graduated and social people with various jobs and positions. From them I learned to be social and lively, and experienced human society. They shared lots of happiness to me, supporting me passed all the difficult days in the past years.

At the last, I would like to thank my parents and my whole family. They supported me to study abroad, and encouraged me to enter the academia field. I hope this thesis is not the end of my thinking, but the very beginning of my future academic career.

Sincerely

秦 峰 (Feng Qin)

2020/01/09

At the University of Tokyo

Contents

Abstract	I
Acknowledgements	V
Contents	VII
List of Figures	XI
List of Tables	XIV
Chapter 1	
Introduction	1
1-1 From the bulk to atomic layers	1
1-1-1 Graphene and scotch tape method	1
1-1-2 Transition metal dichalcogenides	4
1-2 From the solid gate to the liquid gate.....	8
1-2-1 Electronic phase control.....	8
1-2-2 Electric double layer transistor.....	9
1-2-3 Electric field induced superconductivity.....	10
1-2-4 Electrostatic and electrochemical doping.....	12
1-3 From the 2D materials to quasi-1D NTs	14
1-3-1 Carbon NTs.....	14
1-3-2 WS ₂ NTs.....	14
1-3-3 Transport properties of WS ₂ NTs.....	15
1-4 Purpose of this study	16
1-4-1 Motivation to this work.....	16
1-4-2 Organization of this thesis.....	18
Chapter 2	
Experiment	20
2-1 Sample preparations.....	20
2-1-1 Sample synthesis.....	20

2-1-2 Sample preservation.....	22
2-2 Device fabrications	23
2-2-1 WS ₂ NT sample dispersion.....	24
2-2-2 WS ₂ NT device Micro-fabrication.....	25
2-2-3 Wire bonding	29
3-2-4 Ionic liquid droplet putting.....	30
2-3 Transport measurements.....	31
2-3-1 The four-terminal measurement	31
2-3-2 Measurement systems	33
2-3-3 Method of transport measurement	35
 Chapter 3	
Sample characterization	37
3-1 Transmission electron microscope image.....	37
3-2 Diameter distribution of the WS ₂ NT sample	41
3-3 Electron diffraction analysis	42
3-4 Scanning electron microscope image of WS ₂ NT device	46
 Chapter 4	
Ionic liquid gating on WS₂ NT.....	47
4-1 From the solid gate to the liquid gate transistor on WS ₂ NT	47
4-1-1 Field effect transistor on WS ₂ NT.....	47
4-1-2 A proposal of EDLT on TMD NTs.....	48
4-2 Electrostatic doping by ionic liquid medium	49
4-2-1 Ambipolar transfer curve and electron hole symmetry	50
4-2-2 Temperature dependence of ambipolar transfer curve	51
4-2-3 Temperature dependence of resistance.....	53
4-3 Ionic liquid gating driven intercalation	54
4-4 Superconductivity induced by the intercalation	55
4-5 Staging effect in gate induced superconductivity	56
 Chapter 5	
Superconductivity in individual WS₂ NT.....	60
5-1 Introduction to the superconductivity	60
5-1-1 The zero resistance and the Meissner effect.....	61
5-1-2 The Bardeen-Cooper-Schrieffer theory of superconductivity	62
5-1-3 The upper critical field of superconductivity	63

5-1-4 The Ginzburg-Landau model.....	65
5-1-5 The Tinkham model	66
5-1-6 Angular dependence of the upper critical field.....	68
5-2 Anisotropic superconductivity.....	69
5-2-1 The superconducting transition	69
5-2-2 The magnetoresistance during superconducting transition	70
5-3 Intermediate state.....	71
5-4 Upper critical field and Pauli limit	72
 Chapter 6	
Little-Parks oscillation	75
6-1 Introduction	75
6-2 Magnetoresistance oscillation during superconducting transition	76
6-3 Magnetic flux quantization inside superconducting cylinder	78
 Chapter 7	
Diameter-dependent critical temperature T_c	81
7-1 Diameter of NTs.....	81
7-2 Critical temperature.....	84
7-3 Dimensionality of superconductivity.....	87
 Chapter 8	
Nonreciprocal superconductivity in chiral WS₂ NTs.....	90
8-1 Introduction to nonreciprocity	90
8-1-1 Invariance property breaking due to symmetry breaking	90
8-1-2 Chiral scattering.....	93
8-1-3 Magnetic self field	95
8-1-4 Relativistic effect.....	98
8-1-5 Measurement technique	100
8-2 Nonlinear voltage response and photovoltaic effect	101
8-3 Phenomenological description.....	103
8-4 The nonreciprocity in parallel magnetic field.....	105
8-4-1 General discussion	105
8-4-2 The symmetric nonreciprocal signal	108
8-4-3 The antisymmetric nonreciprocal signal	109
8-5 The nonreciprocity in perpendicular magnetic field	111
8-5-1 Nonreciprocal signal in perpendicular magnetic field	111

8-5-2 Possible Weber blockade phenomenon	113
Chapter 9	
Summary	115
Reference	117
List of Publications	124
Curriculum Vitae	125

List of Figures

Figure 1-1: The crystal structure of graphite and graphene, and electron band structure of graphene.....	2
Figure 1-2: The electric field transistor of graphene and anomalous integer Hall effect in graphene.....	2
Figure 1-3: Scotch tape method and strategies beyond graphene.....	3
Figure 1-4: The atomic structures of TMD materials.	5
Figure 1-5: The electronic structure depending on the atomic structures.	6
Figure 1-6: The electronic band structure from the bulk down to the monolayer.	6
Figure 1-7: The MoS ₂ single layer transistor.....	7
Figure 1-8: Spin-orbital coupling and valley degree of freedom.	7
Figure 1-9: Phase control by carrier doping.	8
Figure 1-10: Principle of electric double layer transistor.....	9
Figure 1-11: Phase transition controlled by electric double layer transistor.	10
Figure 1-12: Superconducting dome and Ising pairing in ionic liquid gated MoS ₂	11
Figure 1-13: Electrochemical doping induced superconductivity.	13
Figure 1-14: Figures of WS ₂ NTs.	14
Figure 1-15: High-resolution TEM image of WS ₂ NTs.	15
Figure 1-16: The transport properties of WS ₂ NTs.....	15
Figure 2-1: The growth mechanism of WS ₂ NTs.....	21
Figure 2-2: The procedure of WS ₂ NT dispersion into IPA solvent.	23
Figure 2-3: Schematic figure of spin-coating PMMA resist layer.	24
Figure 2-4: Figure of spin-coater (left) and hot-plate (right).	25
Figure 2-5: The procedure of DELT device micro-fabrication.....	27
Figure 2-6: The photo of e-beam machine.	28
Figure 2-7: The photo of evaporation machine.	28
Figure 2-8: The photo of scribing machine	28
Figure 2-9: The schematic figure of the WS ₂ NT device.	29
Figure 2-10: The photo of wire bonding machine.	30
Figure 2-11: The schematic figure of the WS ₂ NT device with ionic liquid.	30
Figure 2-12: Schematic equivalent circuit of usual two-terminal measurement.	32

Figure 2-13: Schematic equivalent circuit of usual four-terminal measurement.	33
Figure 2-14: The transport measurement system.....	34
Figure 2-15: The schematic figure of sensitive measurements system.....	34
Figure 2-16: The horizontal rotator.....	35
Figure 2-17: The schematic figure of the phase sensitive measurement.	36
Figure 3-1: The TEM figure of WS ₂ NT sample.	39
Figure 3-2: TEM-EDS (Energy Dispersive X-ray Spectroscopy) component analysis.	40
Figure 3-3: The distribution of the outer diameter of the WS ₂ NT sample.....	41
Figure 3-4: The schematic figure of electron diffraction pattern.....	43
Figure 3-5: The electron diffraction pattern of tube A.	44
Figure 3-6: The electron diffraction pattern of tube B.....	44
Figure 3-7: The electron diffraction pattern of tube C.....	45
Figure 3-8: The electron diffraction pattern of tube D.....	45
Figure 3-9: SEM image of a WS ₂ NT device.	46
Figure 4-1: The results of the FET on WS ₂ NT.	48
Figure 4-2: The schematic figure of solid gate (left) and the liquid gate (right) on NT configuration.....	49
Figure 4-3: The ambipolar transfer curve of WS ₂ NT EDLT device.	51
Figure 4-4: The ambipolar transfer curve of WS ₂ NT EDLT device at different temperature.	52
Figure 4-5: The hysteresis of temperature dependence of ambipolar transfer curve.....	53
Figure 4-6: Temperature dependence of resistance modulated by gate voltage.....	54
Figure 4-7: A typical intercalation process.....	55
Figure 4-8: Superconductivity induced by the intercalation.	56
Figure 4-9: The electronic state of lithium-intercalated TaS ₂	57
Figure 4-10: The phase diagram of potassium-intercalated WS ₂	58
Figure 4-11: Similar T_c in multiple gating processes for both two channels.	59
Figure 5-1: The schematic figures of superconducting transition and the phase diagram of type-II superconductor.....	62
Figure 5-2: Conductors (left) and superconductors (right) in external magnetic field. ..	63
Figure 5-3: The schematic figure of vortex state in type-II superconductor.	64
Figure 5-4: The schematic phenomenological description on the Ginzburg-Landau model.	66
Figure 5-5: The schematic phenomenological description on the Tinkham model.	67
Figure 5-6: A schematic figure to represent the direction of external magnetic field. ...	68

Figure 5-7: Two-dimensional superconductivity in ionic liquid gated MoS ₂	69
Figure 5-8: The superconducting transition under the external magnetic field.	70
Figure 5-9: The magnetoresistance during superconducting transition.	71
Figure 5-10: The magnetoresistance during superconducting transition.	72
Figure 5-11: Phase diagram of upper critical field in parallel and perpendicular magnetic field.	73
Figure 6-1: The historic figure of the observation of Little-Parks effect.	75
Figure 6-2: Magnetoresistance oscillation during superconducting transition.	77
Figure 6-3: The magnetoresistance oscillation of two samples.	78
Figure 6-4: Magnetic flux quantization inside superconducting cylinder.	79
Figure 6-5: The schematic figure of the results of Little-Parks experiments.	80
Figure 7-1: Normalized Little-Parks oscillation and peak plot.	82
Figure 7-2: AFM images of four NT samples measured after transport experiments. ...	83
Figure 7-3: Diameter dependence of superconductivity.	84
Figure 7-4: Upper critical field and dimensionality of each NT sample.	86
Figure 7-5: Upper critical field and dimensionality of superconductivity.	87
Figure 7-6: Contour plot of power index versus geometric parameters for different anisotropy.	89
Figure 8-1: Electric magnetochiral anisotropic resistance of distorted bismuth wire. ...	94
Figure 8-2: The schematic figures of handed molecules and composited crystal.	94
Figure 8-3: Effects of nonreciprocal electric transport.	95
Figure 8-4: The nonreciprocal resistance of bismuth helices.	97
Figure 8-5: The nonreciprocal transport in CNT.	97
Figure 8-6: The nonreciprocal transport originating from the relativistic effect.	99
Figure 8-7: The schematic figure of expected nonreciprocal signal.	104
Figure 8-8: Nonreciprocal superconducting transport measured by the second harmonic signal in AC magnetoresistance.	107
Figure 8-9: The symmetrized nonreciprocal superconducting transport signals.	109
Figure 8-10: The antisymmetrized nonreciprocal superconducting transport signals. .	110
Figure 8-11: The observed nonreciprocal signal in perpendicular magnetic field.	111
Figure 8-12: Symmetrized and antisymmetrized nonreciprocal signal.	112
Figure 8-13: The schematic figure of Weber blockade.	113

List of Tables

Table 3-1: The quantitative analysis of both A part and B part.	40
Table 7-1: The NT diameters measured by AFM and by Little-Parks oscillations.	82
Table 8-1: Typical orders of the nonreciprocal parameters in different materials.	100
Table 8-2: The γ tensor for the C_{3V} symmetry group.	102

Chapter 1

Introduction

1-1 From the bulk to atomic layers

1-1-1 Graphene and scotch tape method

Scaling down the dimensionality of a system is always an interesting route for the research in the field of condensed matter physics, due to various fascinating phases emerging from competition between condensations and fluctuations. Thus, the dimensionality plays a significant role in determining the physical properties of materials. Among them, the most famous example is graphene, the “single layered graphite”, which exhibits exotic phenomenon distinct from the bulk graphite [1][2][3]. The discovery of graphene was published in October of 2004 in the journal of *Science* [1] and then awarded the Nobel Prize Award in 2010 [4] “for groundbreaking experiments regarding the two-dimensional material graphene”.

The electronic band structure of graphene, shown in Figure 1-1, has a linear dispersion relation near the K points, known as Dirac cones because the electrons can be described as massless Dirac fermions [5][6][7], leading to the extreme high electric [1] and thermal [8] conductivity for future applications [9][10][11], and providing abundant new physics [2][3], such as integer quantum Hall effect (IQHE) shown in Figure 1-2, predicted theoretically [12] and measured experimentally [13][14] even at room temperature [15], distinct from the previous observation of IQHE at low temperature [16]. In addition, the IQHE is special for the Dirac fermion [12][14] by its unique dispersion relation and electronic density of state.

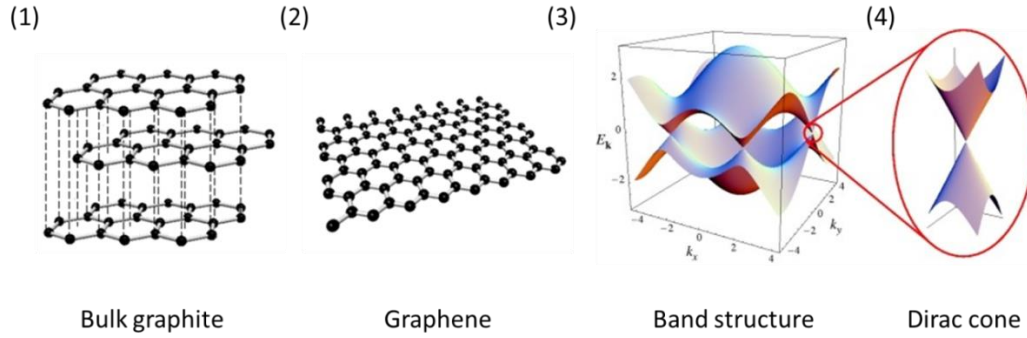


Figure 1-1: The crystal structure of graphite and graphene, and electron band structure of graphene.

(1) The schematic figure of crystal structure of graphite which is hexagonal with lattice constant $a = 2.461 \text{ \AA}$ and $c = 6.708 \text{ \AA}$. (2) The schematic figure of the crystal structure of graphene, which is an atomic scaled honeycomb lattice. Each atom has three neighbors about 1.42 \AA apart. (3) The calculated electronic band structure of graphene through tight binding model. [2] (4) The magnified band structure of one of the six Dirac cones.

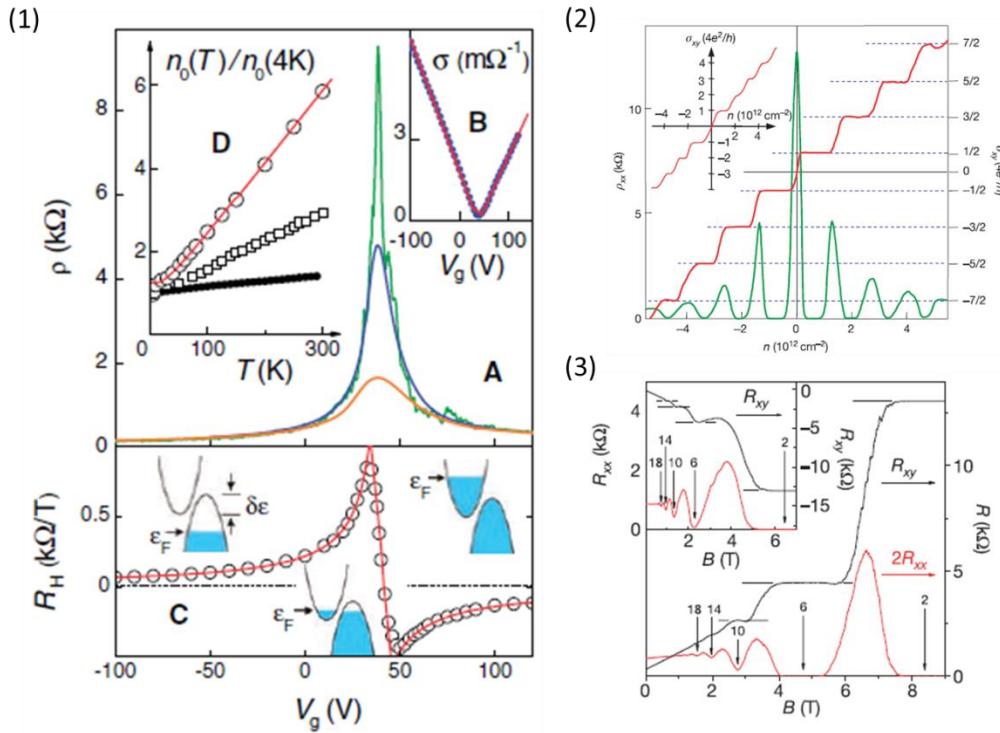


Figure 1-2: The electric field transistor of graphene and anomalous integer Hall effect in graphene.

(1) The Graphene field effect transistor device. (2) The integer quantum Hall effect. (3) The longitude and transverse resistance depending on magnetic field.

Furthermore, what people have learnt from that work is much more than the properties of graphene itself. People have learnt an important, effective but simple method to mechanically exfoliate thin layers from the bulk with Scotch tape and then transfer onto the substrate. The Scotch tape method was reported in 1999 for the first time [17] but became well-known from then on [1]. This remarkable Scotch tape method, as shown in Figure 1-3, combining with nowadays micro device fabrication technique by electron beam lithography, leads people to start the adventure in the two-dimensional world, even beyond graphene [18][19][20][21].

Beyond graphene, people have been researching on more and more creative materials, such as silicone [22][23][24], germanene [25][26], even stanine [27] very recently, and also a rapid rising material named black phosphorus [28][29]. On the other hand, most of the researches are focusing on the transition metal dichalcogenides compounds [30][31][32], which have been thought as the most promising candidates beyond graphene for the future application [19][20][21][33].

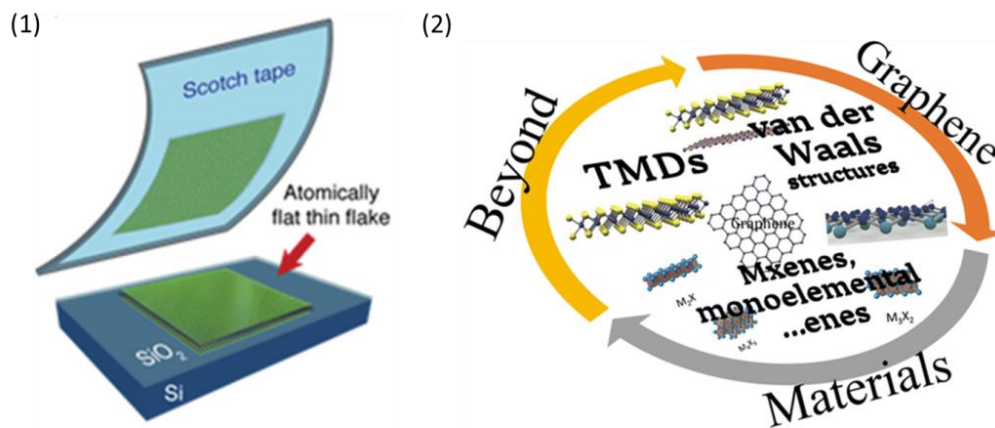


Figure 1-3: Scotch tape method and strategies beyond graphene.

(1) The schematic figure of the Scotch tape method. (2) Three potential routes beyond graphene, including TMD materials, *MX*enes and other mono-elemental-enes, and van der Waals heterostructure for new functionalities [19].

1-1-2 Transition metal dichalcogenides

The transition metal dichalcogenides (TMD) materials, expressed as MX_2 that M is a transition metal ranging from group 4 to 10 and X is a chalcogenide belong to group 16, have layered structure as shown in Figure 1-4. For each layer of TMD materials, there is one layer of M atom sandwiched between two layers of X atoms.

The electronic structure of TMD strongly depends on the atomic structures [31]. In general, d -orbitals of M atoms are located within the gap between bonding (σ) and antibonding (σ^*) M - X bonds, as illustrated in Figure 1-5. Where the bond splitting of d -orbitals of M atoms due to the crystal field are also shown. Because of the crystal field, the d -orbitals of M atoms form degenerate d_{z^2} , $d_{x^2-y^2}$ (e_g) and d_{yz} , d_{zx} , d_{xy} (t_{2g}) orbitals in D_{3d} structure, while the d -orbitals of M atoms with D_{3h} structure split into three groups as d_{z^2} (a_1), $d_{x^2-y^2}$ and d_{xy} (e), as well as d_{yz} and d_{zx} (e') [31][34].

On the other hand, the electronic structures of TMD are also strongly dependent on the layer number. When scaling the TMD materials from bulk down to the monolayer, there is a remarkable electronic state transition, from an indirect gap to a direct gap [30][31].

As an example shown in Figure 1-6, the bond structures MoS_2 have been theoretically calculated from the bulk down to the monolayer [35]. And finally in the case of monolayer, at K -points, there is a direct gap, which has been fully discussed for the optical applications [32].

One of the most important applications of semiconductors is for transistor. Hence, the on/off ratio plays an important role in the research field about field effect transistor. A breakthrough came from the MoS_2 single layer transistor [36], as shown in Figure 1-7. The MoS_2 single layer transistor shows the electron mobility as more than $200 \text{ cm}^2\text{V}^{-1}\text{s}^{-1}$ at room temperature with an on-off ratio of higher than 10^8 , which indicates the TMD Field Effect Transistor (FET) has bright prospects of future applications [19][20][21][33].

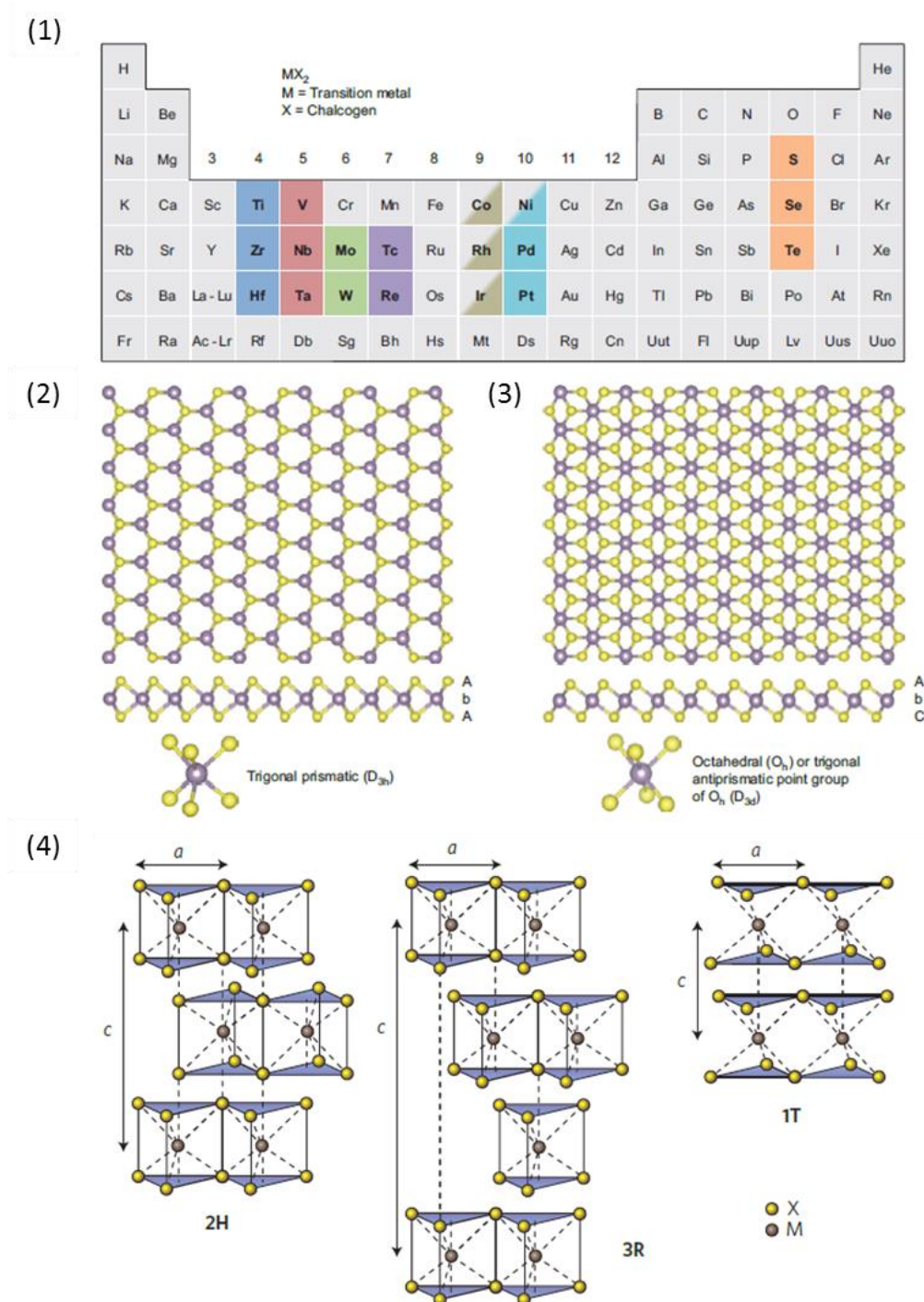


Figure 1-4: The atomic structures of TMD materials.

(1) Chemical compounds of TMD materials. (2)(3) The crystal structures of single layer TMD materials from top view, side view, and the unit cell of TMD materials. (2) The trigonal prismatic structure of group D_{3h} . (3) The octahedral structure of group D_{3d} . (4) Basic layered stacking order of TMD materials, from left to right are 2H, 3R and 1T, respectively.

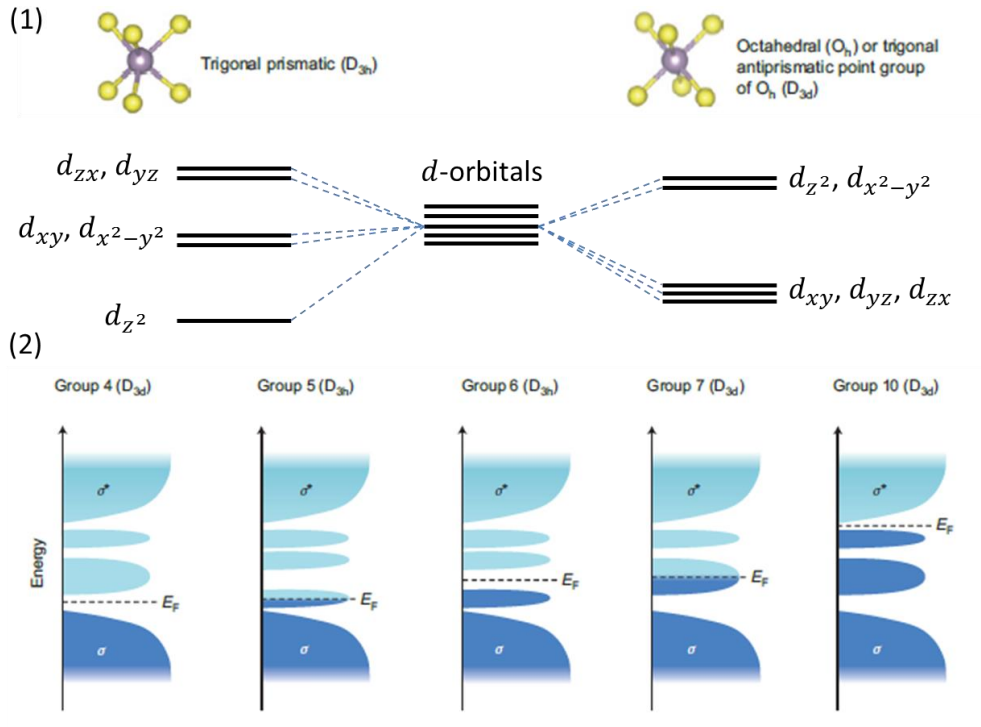


Figure 1-5: The electronic structure depending on the atomic structures.

- (1) The schematic figure of bond splitting of d -orbitals of M atoms due to the crystal field.
- (2) The schematic figure of electronic density of states and also the filling level of d -orbitals of M atoms for different compounds.

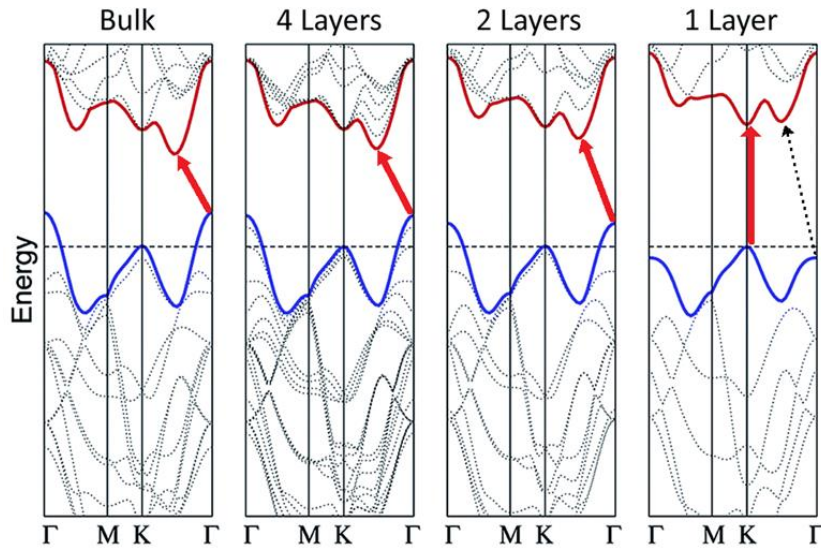


Figure 1-6: The electronic band structure from the bulk down to the monolayer.

From the bulk down to 2 layers, there are indirect band gaps located at Γ -point. However, at monolayer case, the monolayer MoS_2 exhibits a direct band gap at K -points.

As introduced before, the monolayer TMD materials have a direct band gap at K -points, because monolayer TMD materials has no inversion symmetry, which allows additional degree of freedom of electron controlled by light, named as valley degree of freedom [37][38][39][40][41][42]. In addition, because the M atoms are heavy, the valence bond, made of d -orbitals, shows large spin-orbital interaction, while the conduction bond made of s -orbitals displays negligible spin-orbital interaction, as shown in Figure 1-8. The six valleys are separated into two groups, K and $-K$ valley, of which the Berry curvature are opposite and also the Zeeman spin splitting observed in the valence band are opposite [41], leading to valley-selected excitation [38] and also controllable chiral light emission [42]. All of these researches are leading to various optical applications in the future.

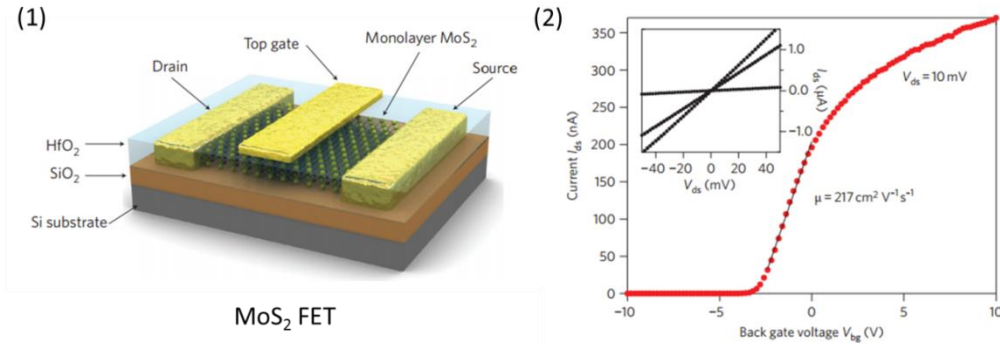


Figure 1-7: The MoS₂ single layer transistor.

(1) The schematic figure of the MoS₂ single layer transistor. (2) The performance of the MoS₂ single layer transistor, indicating extreme high mobility as $\mu = 217 \text{ cm}^2 \text{ V}^{-1} \text{ s}^{-1}$.

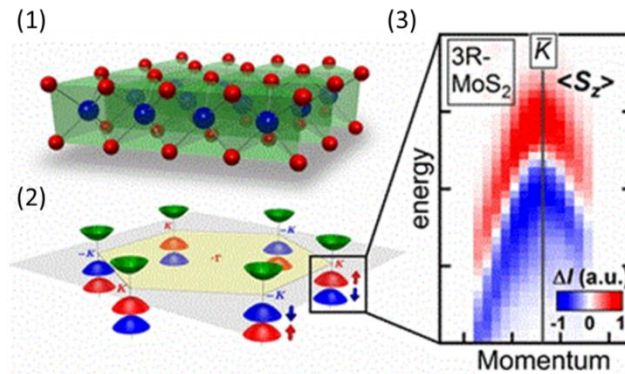


Figure 1-8: Spin-orbital coupling and valley degree of freedom.

(1) The schematic figure of monolayer MoS₂. (2) The schematic figure of direct band gap at K -points. The six valleys are separated into two groups, K and $-K$ valley. (3) The observation of spin splitting in valence band.

1-2 From the solid gate to the liquid gate

1-2-1 Electronic phase control

In materials, different electron doping level makes materials display distinct properties, as shown in Figure 1-9. Chemical doping is the most effective method and commonly used for searching new electronic states in various materials [43]. But it also has some drawbacks. It induces disorders and cannot be reversibly tuned. We have to prepare at least one batch of samples for each doping level [44]. Field-effect doping is an alternative way to accumulate carries without the destruction of crystal structures or the induction of any randomness. Moreover, the doping level can be continuously modulated via gate control. However, the maximum attainable carrier density ($< 10^{13} \text{ cm}^{-2}$), using conventional solid gate dielectrics like SiO_2 , is usually not sufficient even for inducing metallic conductions in insulators.

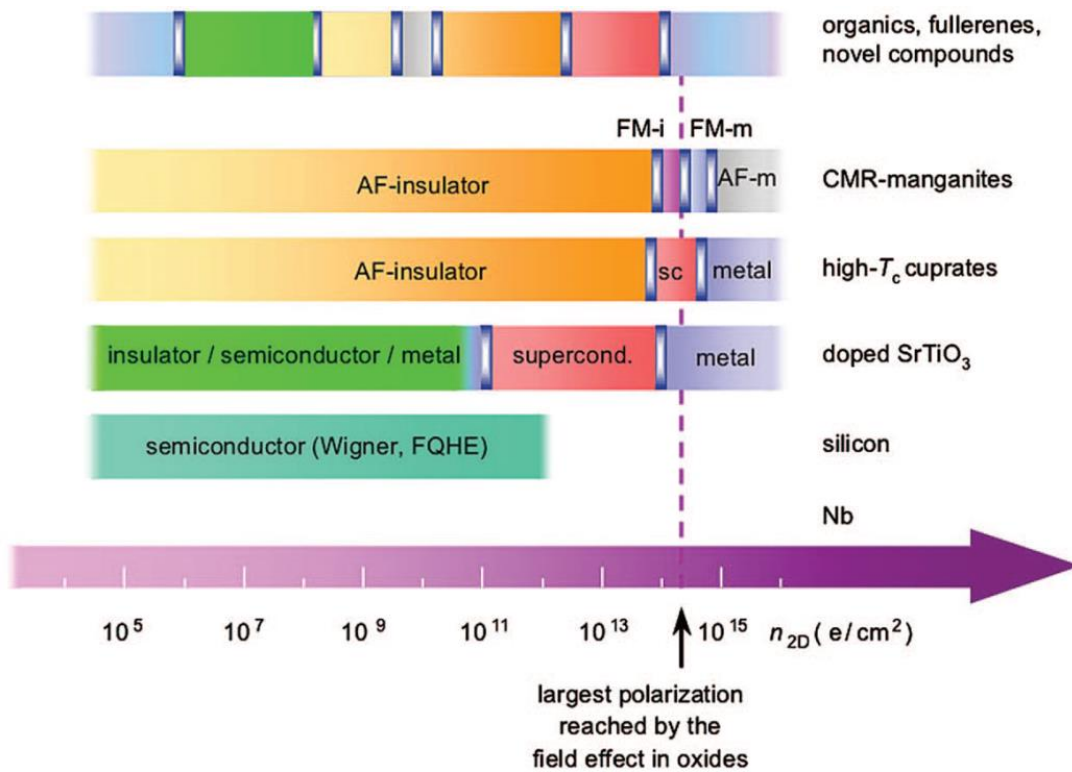


Figure 1-9: Phase control by carrier doping.

In different materials, different carrier density doping level affects the electronic state in materials. By tuning the carrier density through gate, the electronic states can be controllable.

1-2-2 Electric double layer transistor

In recent exciting advances, by replacing the solid dielectric with polymer electrolyte or ionic gel/liquid, a new type of transistor, called electrical double layer transistor (EDLT), has been demonstrated to have the capability to accumulate over ten times higher carrier density ($> 10^{14} \text{ cm}^{-2}$) even at low bias voltages [45]. The implementation of EDLTs based on ionic gating has enabled the modulation of novel electronic properties on oxides and chalcogenides, such as ferromagnetism [46], ambipolar transport [47][48], and field-induced metal-insulator transition, even the superconducting transition [49][50][51][52].

As shown in Figure 1-10, the schematic figure of EDLT device is shown, and the principle of high performance of carrier doping is explained by Figure 1-10 (2). Usually, liquids, especially the ionic liquids, behave much larger dielectric constant than solids, which is crucial for the solid gate, just simply because the ions can freely move under the external electric field. On the other hand, since the ions are accumulated on the top surface of the sample, at the same time, large carriers are doped on the top surface of sample. Thus there is an electric double layer as the interface between the sample and the ionic liquid. With those large carriers doped into materials, it behaves to be a kind of FET. And it is the origin of the name of EDLT. Indeed, the development of EDLT techniques expands the research on electronic phase in materials into a different stage.

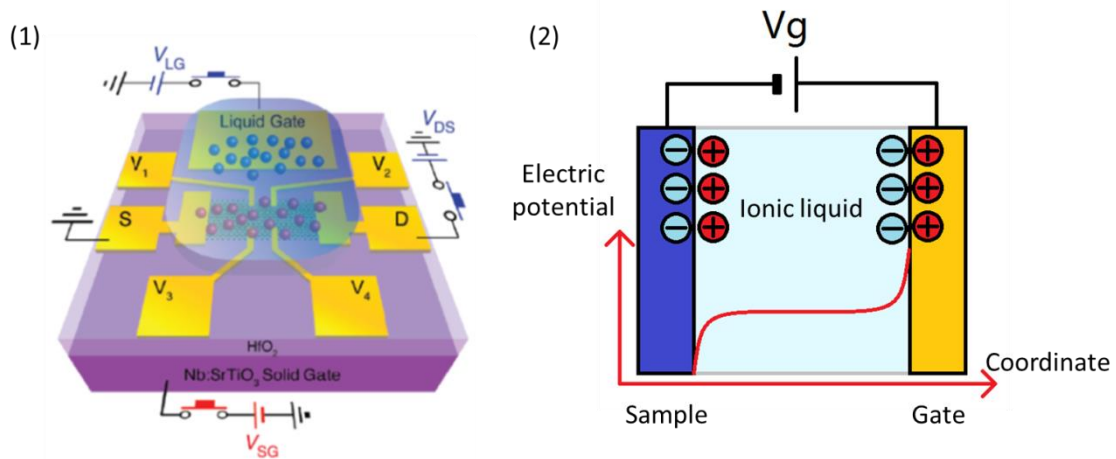


Figure 1-10: Principle of electric double layer transistor.

(1) The schematic figure of electric double layer transistor device. (2) The schematic figure of high performance of carrier doping.

Because EDLT is an efficient method to tune the carrier density in materials, while the electronic states are sensitive to the carrier density in the strongly correlated metals, then electronic states of the material can be easily controlled by EDLT. As shown in Figure 1-11, the Peierls phase transition in VO_2 [53] and the charge density wave transition in TaS_2 [54][55] are strongly dependent on the carrier doping level in the materials which is exactly half-filling the energy band. Hence, by applying EDLT, people can successfully control the phase transition in various layered materials.

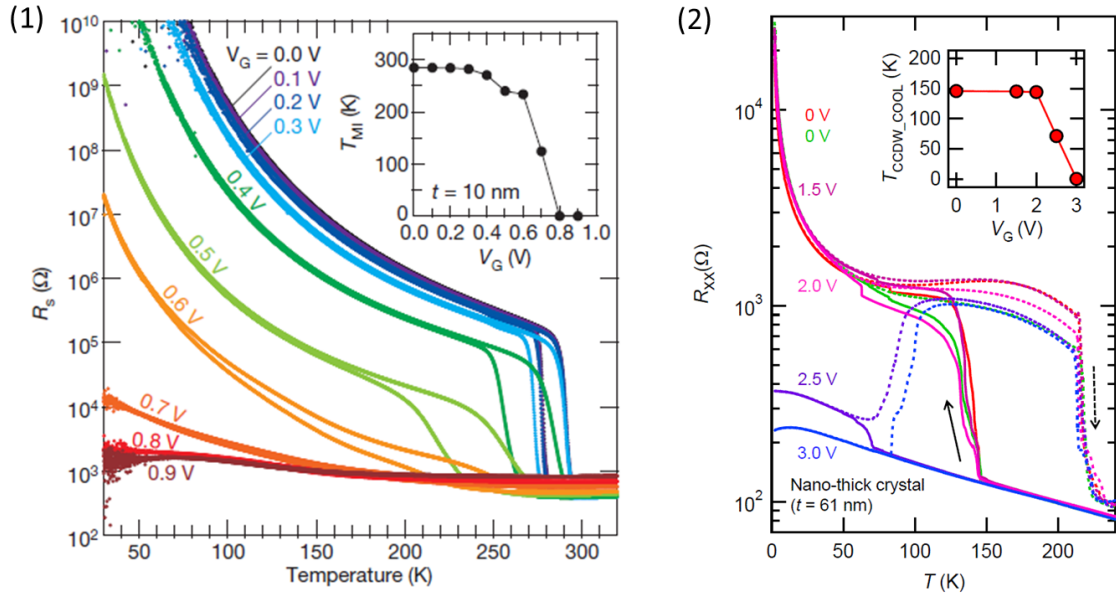


Figure 1-11: Phase transition controlled by electric double layer transistor.

(1) The Peierls phase transition in VO_2 . (2) The charge density wave transition in TaS_2 . Both phase transition are sensitive to the carrier doping level, and thus controllable by the electric double layer transistor.

1-2-3 Electric field induced superconductivity

Since the EDLT performs high carrier doping level, there exists possibilities to induce superconductivity in non-superconducting materials, such as superconducting transition realized in insulator SrTiO_3 [49], in atomic flat ZrNCl film [50][56], in KTaO_3 [51] and even large band gapped MoS_2 [57][58][59] and other TMD materials [59][60]. Among them, the realized superconductivity exhibits unconventional properties because of the two-dimensional nature of accumulated carriers and strong spin-orbital coupling [61], as shown in Figure 1-12.

There exhibits the critical temperature dome as increasing the carrier density. Because the superconductivity is induced by ionic liquid gating, it exhibits the two-dimensional carrier doping and thus results in the two-dimensional nature of superconductivity, confirmed by angular dependence of the upper critical field. In addition, the upper critical field is observed to be much enhanced, which is possible because of the spin-orbital coupling and thus forming Ising type electrons pairing [57][58]. Similar physics has been demonstrated in another material of NbSe₂ [62].

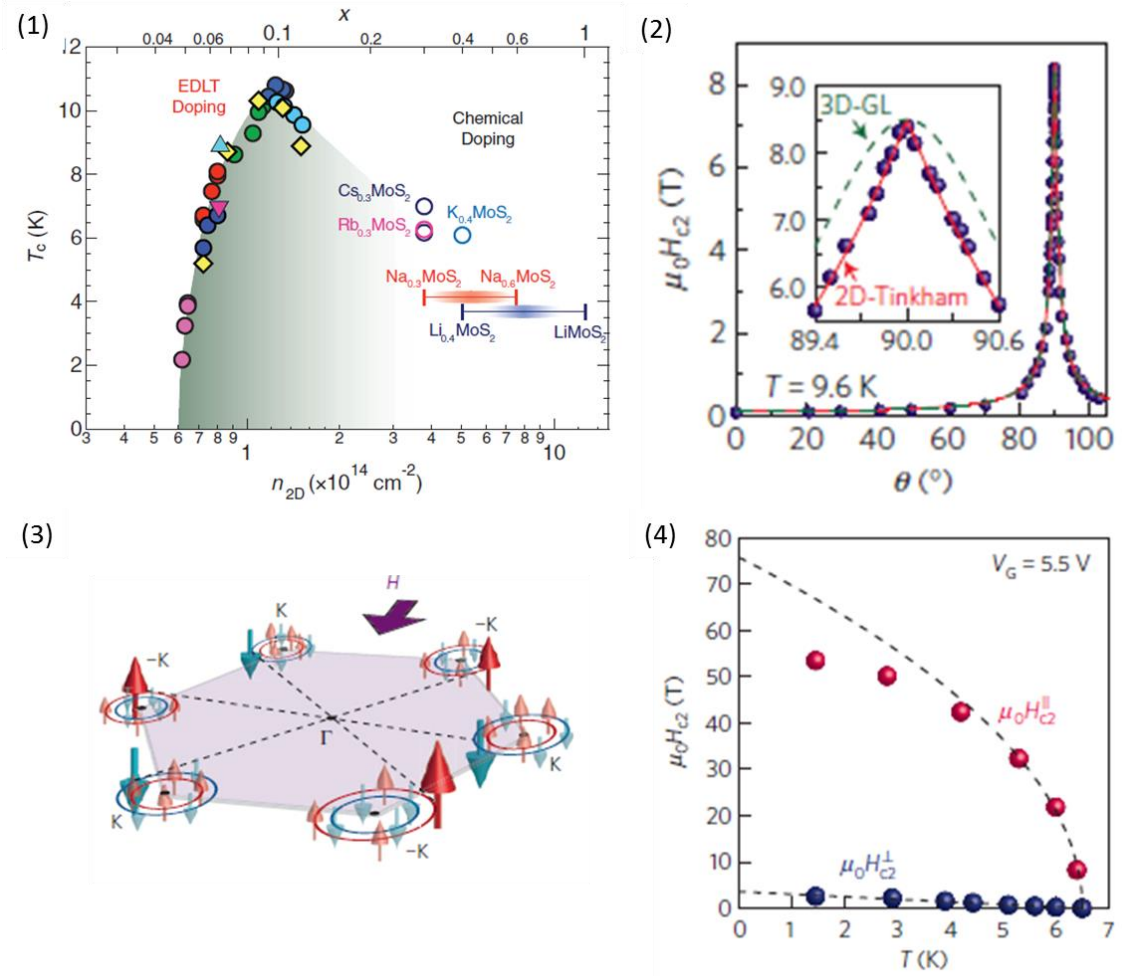


Figure 1-12: Superconducting dome and Ising pairing in ionic liquid gated MoS₂.

(1) The superconducting dome of the critical temperature vs carrier density. (2) The angular dependence of the upper critical field which reflects the two-dimensional nature of induced superconductivity. (3) The schematic field of spin-orbital coupling for effect of pairing. (4) Much enhanced Pauli limits for the upper critical field.

1-2-4 Electrostatic and electrochemical doping

Recently, a new route to the electric field induced superconductivity has been discovered [63] and systematically studied [60]. Beyond electrostatic carrier doping, there is electrochemical doping induced by ionic liquid gating, which is demonstrated that the positive ions pass into the interlayer of the bulk materials and realizing high carrier bulk doping [60][63] instead of surface doping, as shown in Figure 1-13. The source-drain current is firstly saturated with the increase of gate voltage, then the source-drain current keeps increasing reflecting the ions passing into the WS₂ interlayer. Finally, superconductivity is induced after electrochemical doping. Thus, this electrochemical doping technique offers a new method to systematically induce superconductivity in various materials [60].

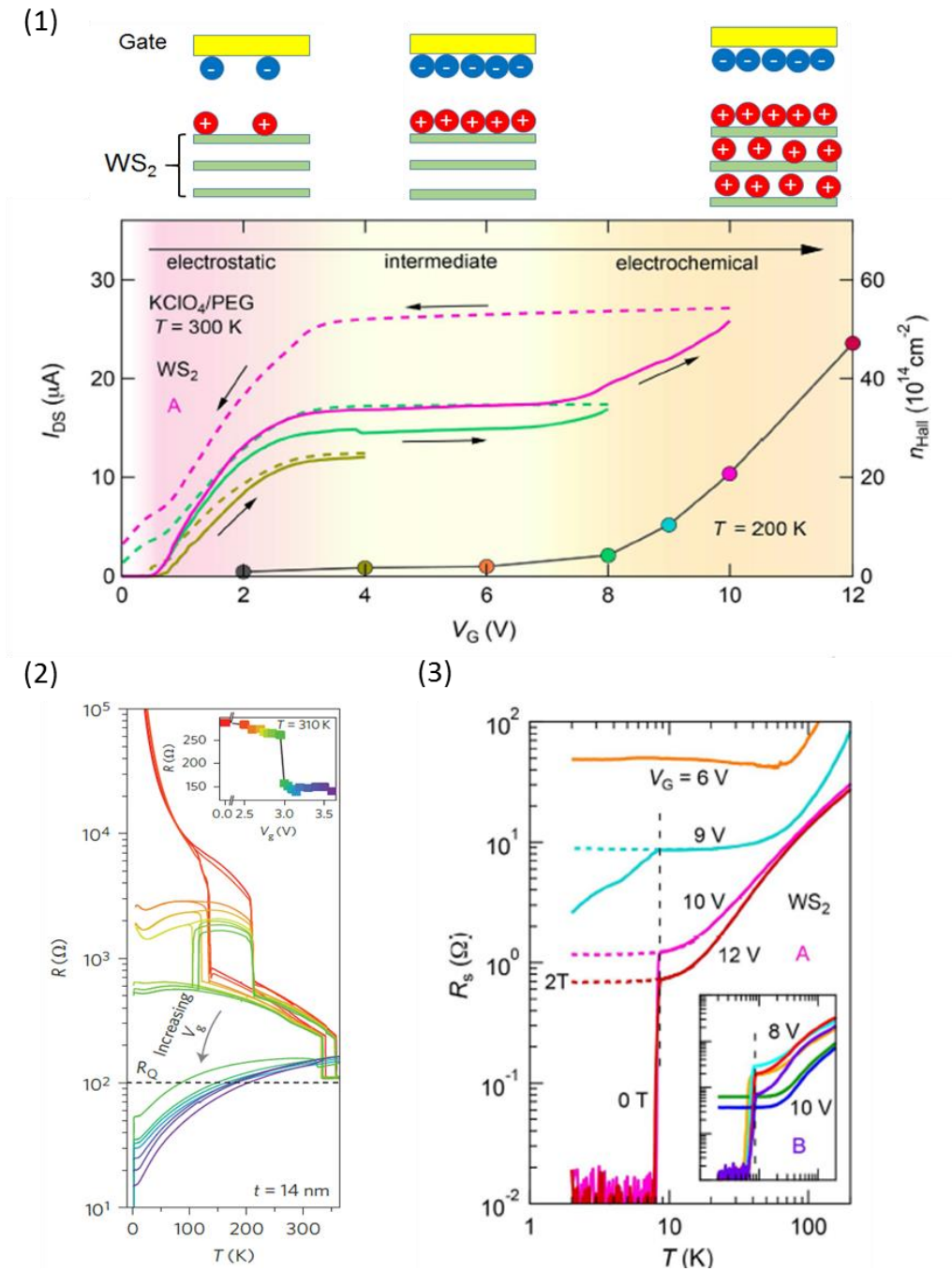


Figure 1-13: Electrochemical doping induced superconductivity.

(1) Figure of electrochemical doping in WS_2 flake. The source drain current is firstly saturated with the increase of gate voltage, then the source drain current keep increasing reflecting the ions passing into the WS_2 interlayer. (2) The electrochemical doping induced in TaS_2 . After electrochemical doping, the resistance obviously decrease and turn into superconductivity at low temperature. (3) The superconductivity induced by electrochemical doping while electrostatic doping cannot induce the superconductivity.

1-3 From the 2D materials to quasi-1D NTs

1-3-1 Carbon NTs

The carbon nanotube (CNT) is a famous organic material, since it was born in 1991 even earlier than graphene [64]. Researchers have been already investigated a lot of properties of CNT [65][66], such as Aharonov-Bohm (AB) oscillations effect in CNT [67], electron-hole symmetry in CNT quantum dot [68], Fabry-Perot interference in CNT [69][70], and even superconductivity [71][72][73][74].

1-3-2 WS₂ NTs

Similar to the TMD materials beyond graphene, people have been thinking about what materials are beyond CNT [75]. Among lots of inorganic nanotubes, WS₂ nanotube (NT) is an interesting candidate, as shown in Figure 1-14, which has been synthesized in 1992 [76][77], just one year after the birth of CNT.

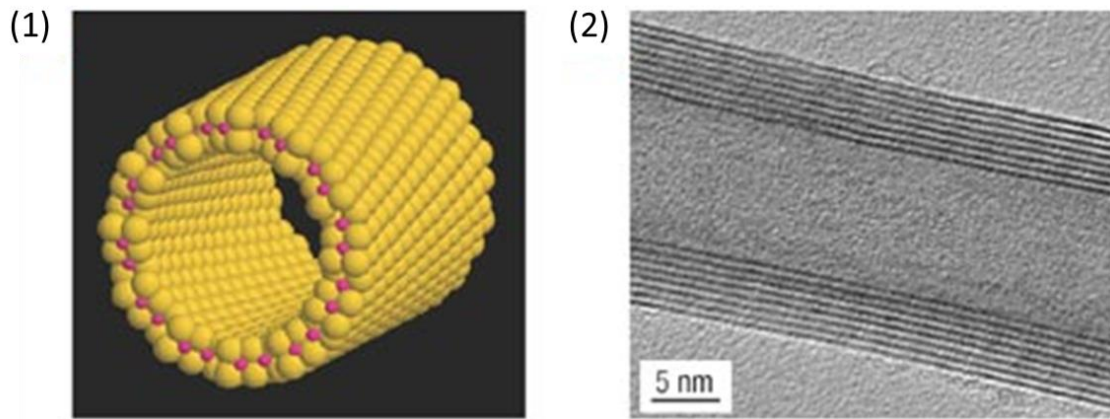


Figure 1-14: Figures of WS₂ NTs.

(1) The schematic figure of WS₂ NT. (2) The Transmission Electron Microscopy (TEM) image of WS₂ NT, and a hollow cylindrical structure is shown.

From the literatures, most of WS₂ NTs synthesized has an outer diameter ranging from tens to hundreds of nanometers. According to figures adapted from reference [78], the tube part has a 2H-polymorph-layered structure of WS₂, where each tungsten atom is surrounded by six sulfur atoms in trigonal bipyramid coordination (space group P6₃/mmc), as shown in Figure 1-15.

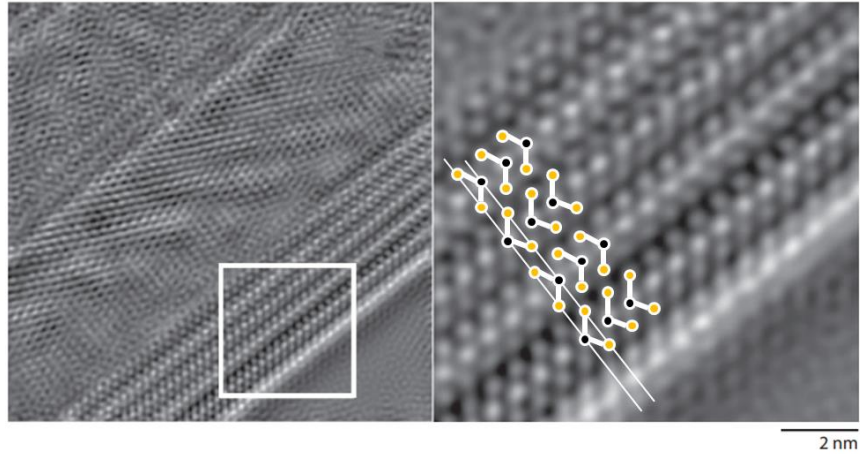


Figure 1-15: High-resolution TEM image of WS₂ NTs.

In these figures, the high-resolution TEM image of WS₂ NTs is shown in left side. In the right side, a magnified part of square area in left side is shown, in which the location of each atoms can be recognized, and a 2H-polymorph-layered structure is shown.

1-3-3 Transport properties of WS₂ NTs

The transport properties of WS₂ NT have been known as insulator. As shown in Figure 1-16, the nonlinear source drain current dependence of the source drain voltage is fitted by using a metal-semiconductor-metal model [78] In addition, at the presence of water or oxygen, the transport properties decrease, while increase under light illuminance [79][80]. On the other hand, the WS₂ NT random network affected by ionic liquid gating has been also clarified by the observed ambipolar transfer curve [81].

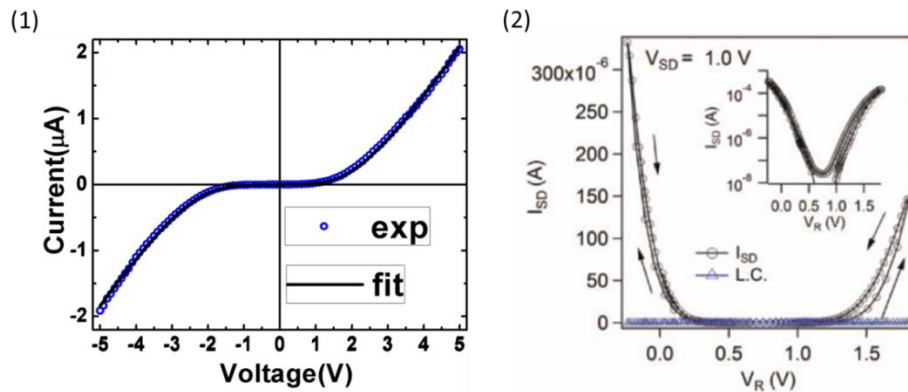


Figure 1-16: The transport properties of WS₂ NTs.

(1) The insulating behavior of individual WS₂ NT. (2) The ambipolar transfer curve of WS₂ NT random networks.

1-4 Purpose of this study

1-4-1 Motivation to this work

Scaling down the dimensionality of a system is always interesting in the research field of condensed matter physics, due to various fascinating phases emerging from competition between condensations and fluctuations. For instance, superconductivity, the most famous condensed phase in materials, shows totally different behaviors when scaling down the system dimensions and finally disappears in one dimension (1D) due to quantum fluctuation. Therefore, recently two dimensional (2D) superconductors in atomically thin metals, mechanically exfoliated 2D materials, and various heterogeneous interfaces are attracting lots of interest. Beyond those, nanotube (NT) should be a new platform for the nanoscaled superconductor because of its unique geometry with an intermediate dimension. Moreover, NT has a distinct topology compared with usual materials, indicating novel properties originating from quantum interference along the NT circumference. The relations between the geometry of materials and superconductivity are highly anticipated to yield unexpected quantum phenomena. Hence, the superconducting NT, once it is realized, due to its uniqueness in geometry, is a potential material for searching exotic phenomena and nontrivial superconductivity.

In the past years, the superconductivity in NTs has not been well-studied so far because of the lack of suitable materials. Although there are intensive studies of superconductivity in carbon NTs in the past years, properties of superconductivity have been investigated only in the assembled form of NTs, and until now such properties reflecting the unique geometry of individual NT have remained elusive.

Above all, we are focusing on another NT made of tungsten disulfide (WS_2) based on three reasons. First, WS_2 NT is famous and well-characterized, because it is the first inorganic NT synthesized in 1992, just one year later than the birth of carbon NT. Second, WS_2 is a member of transition metal dichalcogenides (TMDs) which are now attracting significant attention as 2D materials beyond graphene with novel properties and potential applications for electronics, photonics, spintronics, mechanics, as well as valleytronics. Third, recent systematic studies have been clarified that lots of TMDs including WS_2 , which are semiconductors without doping, exhibit superconductivity under the ionic gating. Hence, WS_2 NT is a promising candidate to realize

superconductivity with novel properties and broad applications in the future.

Aimed at the following points, we have studied the transport properties of WS₂ NT under ionic gating.

- **To realize of superconductivity in WS₂ NTs.**
- **To clarify the relation between superconductivity and the unique geometry of NTs.**

Then, after we have succeeded in the realization of superconductivity in tungsten disulfide (WS₂) nanotubes (NTs) induced by potassium intercalation driven by ionic liquid gating, and clarified exotic superconductivity reflecting its unique geometry of WS₂ NTs. We become interested in the other geometric clues which can be reflected through superconductivity.

For instance, the diameter-dependent superconductivity is extremely interesting. By summarizing data and concluding the relationship between the diameter of NTs and the properties of superconductivity, it will be beneficial for understanding the deeper physics of superconductivity, such as pairing mechanism.

There are possibilities that we can investigate another geometric property of WS₂ NTs much further. In addition to the nanoscaled cylindrical structure of WS₂ NTs, there is an additional degree of freedom, chirality in the rolled structure, which breaks global inversion symmetry. Such a chiral structure might cause unique electronic properties distinct from two dimensional (2D) systems, which will highly contribute to revealing the origin of the superconductivity. This proposal implies that nanomaterials with peculiar lattice structures and broken spatial inversion symmetries offer a new route to manipulate superconductivity.

Hence, finally we turn into the final target of this work.

- **To clarify the effect of chirality on superconducting transport in WS₂ Chiral nanotubes (NTs).**

One of the manifestations of chiral structure in the electronic transport is the

nonreciprocal resistance, in which the forward and backward current flows are not equivalent because of the inversion symmetry breaking, when the magnetic field is applied parallel to the tube, which can be measured as the second harmonic signal in the alternative current (AC) mode by lock-in amplifiers.

The second harmonic signal is expected to be significantly enhanced due to the highly coherent nature of superconductivity. Hence, by scanning the external magnetic field, the second harmonic signal will be measured at each fixed temperature varying from normal state to superconducting state, simultaneously the first harmonic signal which should reflect the Little-Parks oscillation due to the cylindrical structure of NTs will also be measured. On the other hand, because the Little-Parks oscillation, resulting from the quantum interference of the supercurrent along the circumference of NT, reflects magnetic flux quantization inside NT, the second harmonic signal, originated from the chiral structure of NT, should also reflect the same nature of quantization of magnetic flux. The relation between the first and the second harmonic signal will be clarified in both normal and superconducting state of WS₂ NT under magnetic field for both $H \parallel z$ and $H \perp z$, respectively (z represents the tube axis direction).

Physics is a subject associated with experiments closely, and all the development and breakthroughs cannot happen without experiments. Thus, we believe that this work will lead to significant breakthroughs of a deeper understanding of superconductivity. The chirality of NT will be a key characteristic for potential future functionalities.

1-4-2 Organization of this thesis

In this whole study, the basic physical transport properties of the semiconducting inorganic tungsten disulfide (WS₂) nanotubes (NT) have been investigated by using the electric double layer transistor (EDLT) techniques and the phase sensitive measurements on both the first and the second harmonic signal. The study is not confined within the demonstration of high performance of field effect on individual WS₂ NT by EDLT, but we also discovered a new functionality such as the nonreciprocity of superconductivity for the first time.

After this introduction part in Chapter 1, the experimental techniques are shown in Chapter 2, including device fabrication process are introduced, as well as the phase sensitive transport measurements.

Then, the characterization of WS_2 NT is shown in Chapter 3, containing Transmission Electron Microscopy (TEM) and Electron Diffraction (ED) analysis.

Next, the experimental results of ionic liquid gating response are shown in Chapter 4. Not only the ambipolar transfer curve, but also the process of intercalation will be discussed. By intercalation, the WS_2 NTs become superconducting at low temperatures. A possible staging effect is also discussed.

In Chapter 5, anisotropic superconductivity corresponding to the NT geometry is discussed. The intermediate state when magnetic field applied perpendicularly to the NT, and the possible mechanism of upper critical field higher than Pauli limit when magnetic field applied parallel to the NT, are also discussed.

Furthermore, the observation on quantum oscillating behavior reflecting the NT geometry is shown in Chapter 6, and the diameter dependence of superconductivity in NTs is discussed in Chapter 7.

At the last in Chapter 8, we display our phenomenological expectation of the chirality effect on superconducting transports and the related experimental result is presented.

Chapter 2

Experiment

In this chapter, the detailed experimental procedure of this work will be introduced. The tungsten disulfide (WS_2) nanotube (NT) sample was given by Prof. Reshef Tenne and Prof. Alla Zak, and I will briefly introduce how they synthesized WS_2 NT sample following previous studies in the first part, 2-1 Sample preparations. Then, in the second part, 2-2 Device fabrications, I will show you how to fabricate WS_2 NT device with electric double-layer transistor (EDLT) configuration for the transport measurements. Finally, I will explain the experimental techniques of transport measurements in the last part, 2-3 Transport measurements. The performance of WS_2 NT EDLT device during transport measurements will be discussed in the next several chapters.

2-1 Sample preparations

2-1-1 Sample synthesis

In this section, the growth mechanism of WS_2 NT sample will be briefly discussed following previous studies [82][83]. The beginning of the synthesis route for the WS_2 NT sample is spherical tungsten oxide nanoparticles (Figure 2-1 (1)), where the oxide ratio of tungsten oxide nanoparticles ranges from 2.83 to 3, and the diameter of tungsten oxide nanoparticles is mainly smaller than 100 nm. Then tungsten oxide nanoparticles are sulfurized by solid-gas reaction with hydrogen (H_2) and hydrogen sulfide (H_2S) at elevated temperatures ($> 800^\circ\text{C}$) (Figure 2-1 (2) to Figure 2-1 (5)). The tungsten oxide nanoparticles change from non-volatile phase (Figure 2-1 (1)) to volatile phase (Figure 2-1 (2)), then new non-volatile phase forms (Figure 2-1 (3)) and subsequently serves as nucleus for the growth of long tungsten suboxide whiskers (Figure 2-1 (4)). While the

growth of tungsten suboxide whiskers, the sulfurization on whiskers starts from the outside to inside, from the middle toward the ends (Figure 2-1 (4)). Finally, the WS₂ NTs of around 100nm in diameter and up to 20nm in length are synthesized with high quality (Figure 2-1 (5)). These two main steps of the reaction, the oxide whiskers growth and the sulfurization on whiskers, occur under the same H₂S/H₂ gas flow regime, and are not separated in space following each other in a self-controlled mechanism.

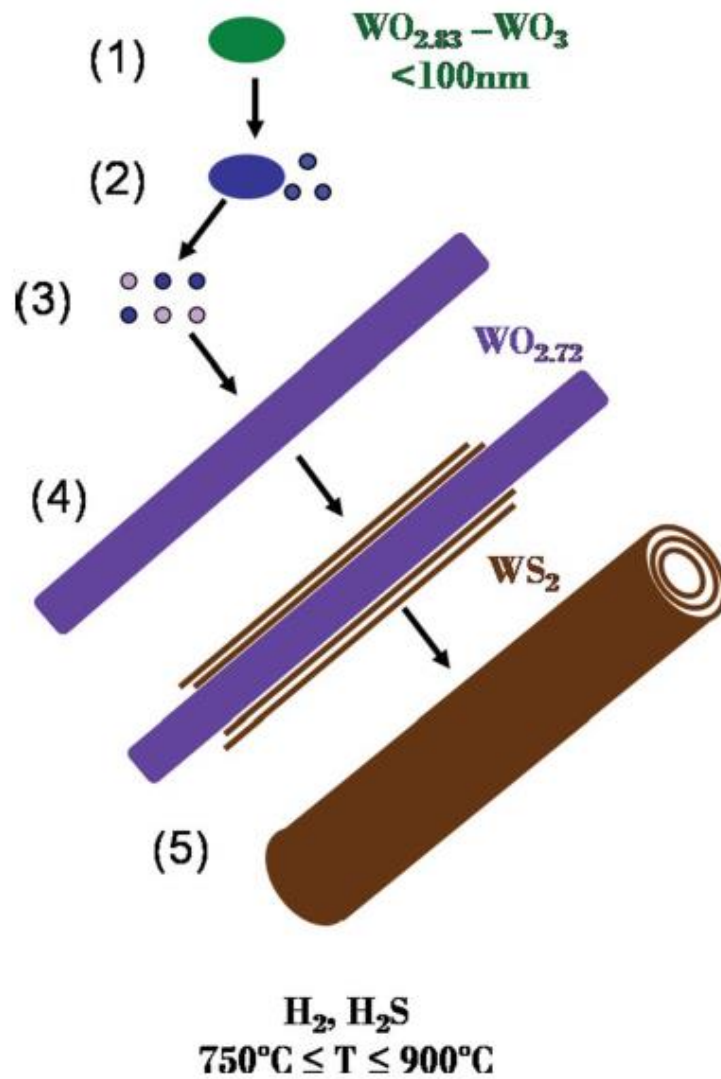


Figure 2-1: The growth mechanism of WS₂ NTs.

(1) A mixture of tungsten oxide nanoparticles. (2) During chemical reactions, tungsten oxide nanoparticles change from non-volatile phase to volatile phase. (3) New non-volatile phase forms as nucleus for tungsten suboxide whisker growth. (4) Two main steps of the reaction - oxide whiskers growth and sulfurization on whiskers. (5) After sulfurization, WS₂ NT sample are prepared with high quality.

2-1-2 Sample preservation

The WS_2 NT sample was firstly powder configuration, which was very inconvenient for us to preserve and to prepare WS_2 NT device for the use of many times. Because we aimed to fabricate isolated individual WS_2 NT device for the clarification of its physical properties, we followed normal procedures [84][85] to disperse WS_2 NT sample into isopropyl alcohol (IPA) solvent by ultrasonication for 20 minutes, in order to (1) uniformly suspended in the liquid, and to (2) separate well-formed individual WS_2 NT from each other and from amorphous WS_2 or other junks, as well as to (3) fabricate isolated individual WS_2 NT device in the future (see 2-2 Device fabrications). It should be noted that the WS_2 NT sample are insulator or semiconductor, which is stable during ultrasonication due to strong covalent bonds. However, conducting NT or thin diameter NT might be fragile under ultrasonic sound, and if you do ultrasonication then you might get nothing but all of the junks.

The procedure of WS_2 NT sample dispersion is shown in Figure 2-2. The WS_2 NT sample powder was firstly dispersed into IPA solvent (①), then after ultrasonication to make uniformly suspension, subsequently dilute into another IPA solvent (②). Repeating the above procedure for several times, finally we got several suspended liquid with different ratio, labeled as ① to ④. Among them, ① had the highest ratio and ④ had lowest ratio. We just roughly did above procedures, because the exact ratio is not so important. At the last step, a droplet of the suspension chosen from each liquid was spin-coated a Si/SiO₂ (3000 Å) substrate (about spin-coat procedure, see Chapter 2-2 Device fabrications), and isolated WS_2 NTs were subsequently chosen under an optical microscope. By judging from optical microscope, the liquid with label ④ had the best ratio of dispersion because there were a lot of isolated and long WS_2 NTs (high quality) and almost no junks to interfere with selecting individual WS_2 NTs. In the following chapters, all of the WS_2 NTs were chosen from the liquid labeled as ④.

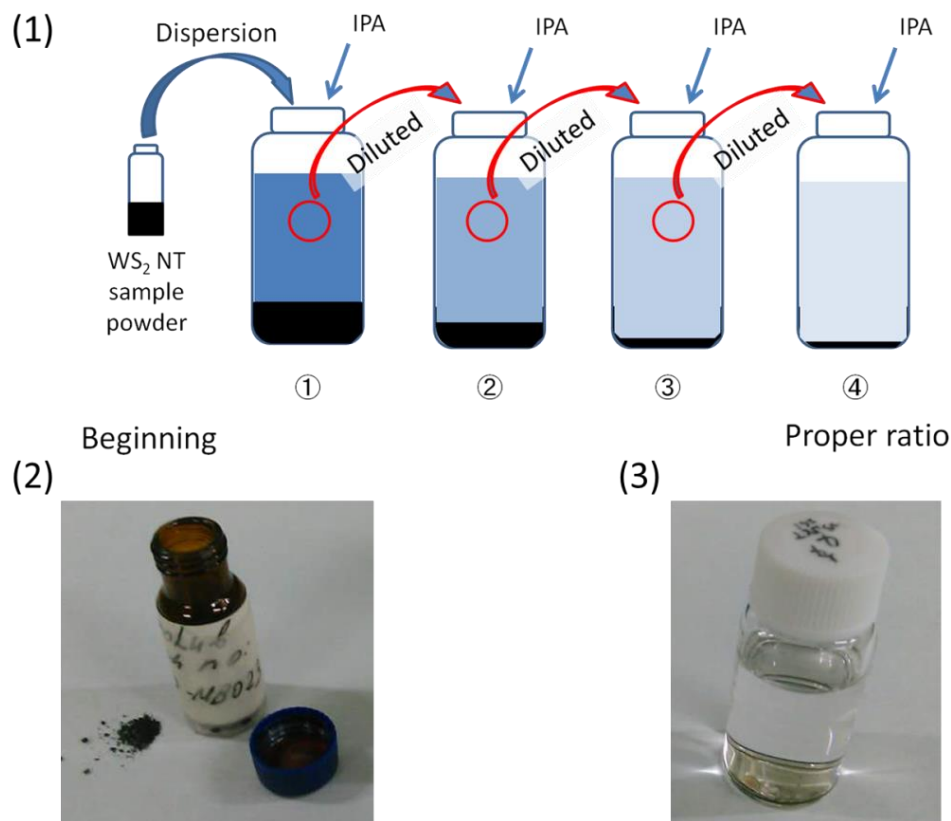


Figure 2-2: The procedure of WS_2 NT dispersion into IPA solvent.

(1) Schematic figure of dispersion. (2) The photo of WS_2 NT sample powder. (3) The photo of the liquid with proper ratio labeled as ④.

2-2 Device fabrications

In this section, the fabrication procedure for WS_2 NT EDLT device will be shown, following mainly four different steps:

- ① WS_2 NT sample dispersion
- ② WS_2 NT device Micro-fabrication
- ③ Wire bonding
- ④ Ionic liquid droplet putting

Among them, the final step ④ is specialized only for EDLT device with ionic liquid droplet. If you want to fabricate device for other special use, you just need follow the procedure ranging from ① to ③, and do your special design for device structure in step ②.

2-2-1 WS₂ NT sample dispersion

As I mentioned before (see Chapter 2-1 Sample preparations), The WS₂ NT sample was firstly powder configuration and dispersed in IPA solvent for the future use. After shaking the bottle (labeled as ④ with proper diluted ratio) by hand and suspending by ultrasonic sound. Followed by Figure 2-3, A droplet of the suspension is spin-coated on a Si/SiO₂(3000Å) substrate by using a programmable spin-coater (shown in Figure 2-4) in order to remove redundant liquid. And then immediately cover polymethyl methacrylate (PMMA) around 400nm in thickness by using the same mode and the same programmable spin-coater.

There are three steps spinning performed as shown in Figure 2-3:

- ① Start with 500 rpm within the first 3 seconds
- ② Continue 4000 rpm for the next 50 seconds
- ③ Stop spinning for the last 3 seconds

First, a droplet of the suspended liquid or a droplet of PMMA is put on the top. Then, during continued 4000 rpm for 50 seconds, the droplet spreads and uniformly covers the top surface. Finally, the droplet becomes dry and forms a thin layer on the top. For the case of PMMA, the spin-coated substrate needs to be heated for 1 minute on a hot-plate at 180°C.

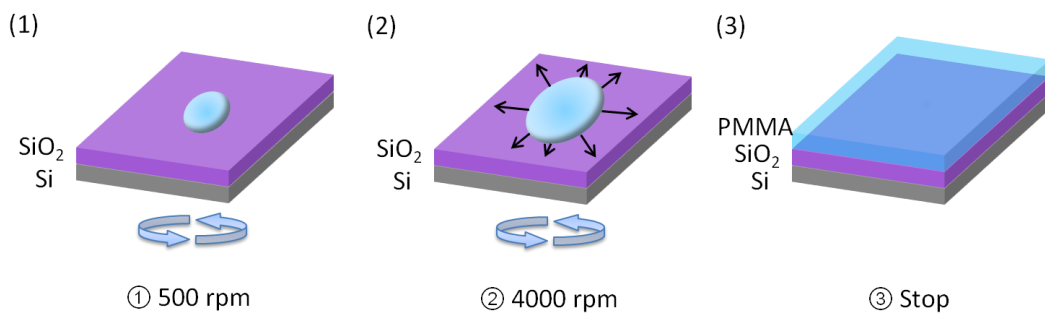


Figure 2-3: Schematic figure of spin-coating PMMA resist layer.

(1) Start with 500 rpm within the first 3 seconds. (2) Continue 4000 rpm for the next 50 seconds. (3) Stop spinning for the last 3 seconds.

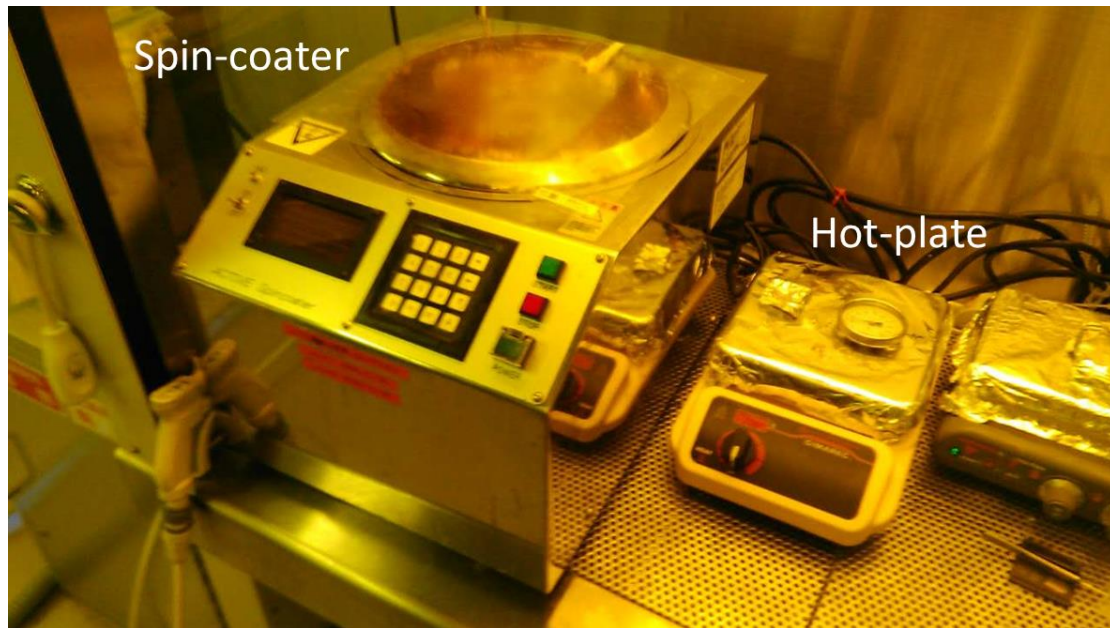


Figure 2-4: Figure of spin-coater (left) and hot-plate (right).

Figure of spin-coater (left) and hot-plate (right) are shown.

There are two reasons to cover PMMA immediately after spin-coating the suspended liquid. First, the PMMA layer can be a protected layer to protect WS₂ NT sample from air and water, which has been reported that the transport performance of WS₂ NT is decreased by exposing on oxygen and water [79]. Second, the PMMA layer can be an e-beam-resist designing device pattern and then making electrodes, which will be introduced in the next section.

2-2-2 WS₂ NT device Micro-fabrication

The procedures of WS₂ NT device micro-fabrication follows below seven steps and key steps are shown in Figure 2-5.

- ① Select isolated NT via microscopy
- ② Device pattern design
- ③ Developing
- ④ Gold electrodes evaporation
- ⑤ SiO₂ protect layer evaporation
- ⑥ Substrate scribing
- ⑦ Device lift-off

After the WS₂ NT sample dispersed follows the procedures shown in the previous section, the procedures of WS₂ NT device micro-fabrication starts. First, the isolated WS₂ NTs are chosen under an optical microscope as shown in Figure 2-5 (1).

Then taking photos of WS₂ NTs and designing device pattern via AutoCAD program of version 2015 student which is download from Website of Autodesk Company (Figure 2-5 (2)). We fabricate both end-contacted (like Figure 2-5 (2)) and bulk-contacted device, and use four-terminal measurement to measure the resistance of WS₂ NT.

After finishing the device pattern design, the AutoCAD file is converted into dxf file and transfer to controlled computer of e-beam machine. There are two steps of e-beam lithography, relevant parameters are 1000 pA of e-beam current, 2 s of dose time, and 1200 μm of drawing size for the first e-beam lithography, and 100 pA of e-beam current, 2 s of dose time, and 300 μm of drawing size for the second e-beam lithography. By using e-beam machine (Figure 2-6), the designed pattern is drawn on the substrate covered by e-beam resist (PMMA), as shown in Figure 2-5 (6). When PMMA is shined in the e-beam, PMMA is resolved (Figure 2-5 (6)).

In develop procedure, we use the liquid mixed by MIKB and IPA with ratio 1:3 in order to remove resolved part (Figure 2-5 (3) and Figure 2-5 (7)).

After finishing the e-beam lithography and developing, the substrate with designed pattern is sent into the vacuum chamber of evaporator machine (Figure 2-7).

We make electrodes with gold (Au 90nm) by evaporating method, and use Cr (5nm) as binder. We also evaporate SiO₂ as insulating layer to protect electrodes from damage by ionic liquid when applying gate.

Then, the substrate is cut into several pieces by scribing machine (Figure 2-8), and there is one single device on each piece. Up to this step, the device can be preserved in vacuum box for a long time and then lift-off just before we are going to measure it. In the final step of fabricating micro-device, the device is dipped in the liquid of acetone for one hour to remove the redundant PMMA and gold, only the fabricated electrodes is remained on the substrate, as shown in Figure 2-5 (9) and (10). Finally, the photo of the well-made device is shown in Figure 2-5 (4)

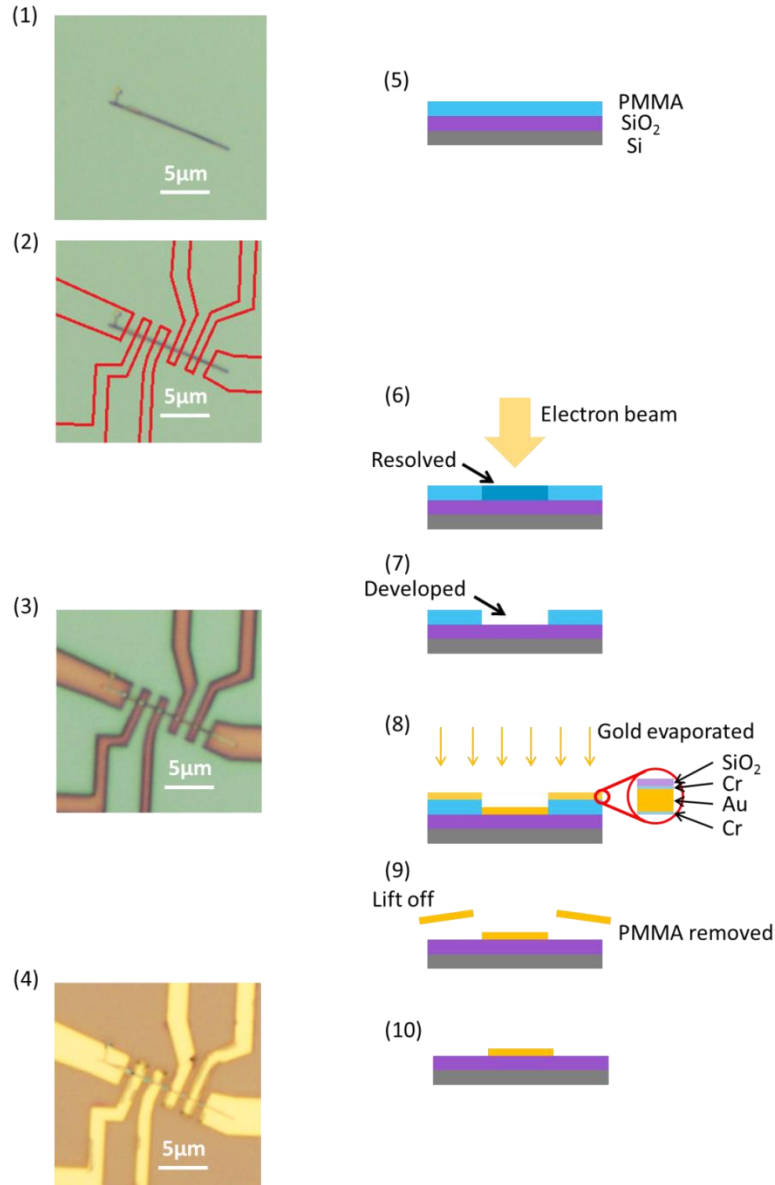


Figure 2-5: The procedure of DELT device micro-fabrication.

Photos from top view (left) and schematic figures from side view (right). (1) The photo of an individual WS_2 NT covered by PMMA. (2) The designed pattern of nano-device. (3) The photo of the pattern after develop. (4) The photo of pattern after gold electrodes evaporation. (5) The schematic figure of the substrate covered by PMMA. (6) The schematic figure of the substrate after e-beam lithography. (7) The schematic figure of the substrate after develop, the resolved part is removed. (8) The schematic figure of evaporation, the electrodes are made of $\text{Cr}(5\text{nm})/\text{Au}(90\text{nm})/\text{Cr}(5\text{nm})/\text{SiO}_2(20\text{nm})$ layer by layer, $\text{Cr}(5\text{nm})/\text{SiO}_2(20\text{nm})$ is aimed to protect electrodes from damage by ionic liquid during gating. (9) The schematic figure of the process of lift-off (10) The schematic figure of the substrate after lift-off, the PMMA is removed and only electrodes are remained.



Figure 2-6: The photo of e-beam machine.

The photo of e-beam machine is shown.



Figure 2-7: The photo of evaporation machine.

The photo of evaporation machine is shwon.

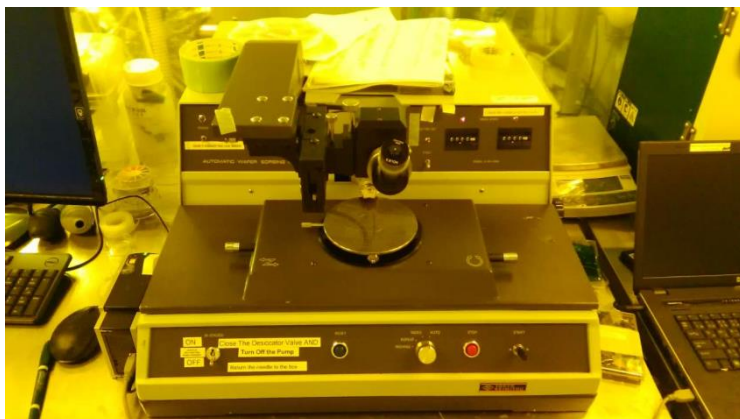


Figure 2-8: The photo of scribing machine

The photo of scribing machine is shwon.

2-2-3 Wire bonding

After micro-fabricating device of WS₂ NT sample, we finally fix the substrate on the chip-carrier by silver paste, and then connect electrode pads on device and electrodes on chip-carrier one by one with gold line by wire bonding machine.

The schematic figure of the WS₂ NT device is shown in Figure 2-9, and the wire bonding machine is shown in Figure 2-10: The photo of wire bonding machine. We use a special chip-carrier or sample holder with the horizontal rotator, which is able to rotate the substrate when measuring inside PPMS. This will be introduced in the next part, chapter 2-3 Transport measurements. Because the sample is tiny, any static electricity may damage the sample and the device cannot work anymore. Hence, we ground our body and also the device to protect the device in the following procedures, wire bonding and ionic liquid droplet putting. The ground line is shown in Figure 2-10: The photo of wire bonding machine. in red box.

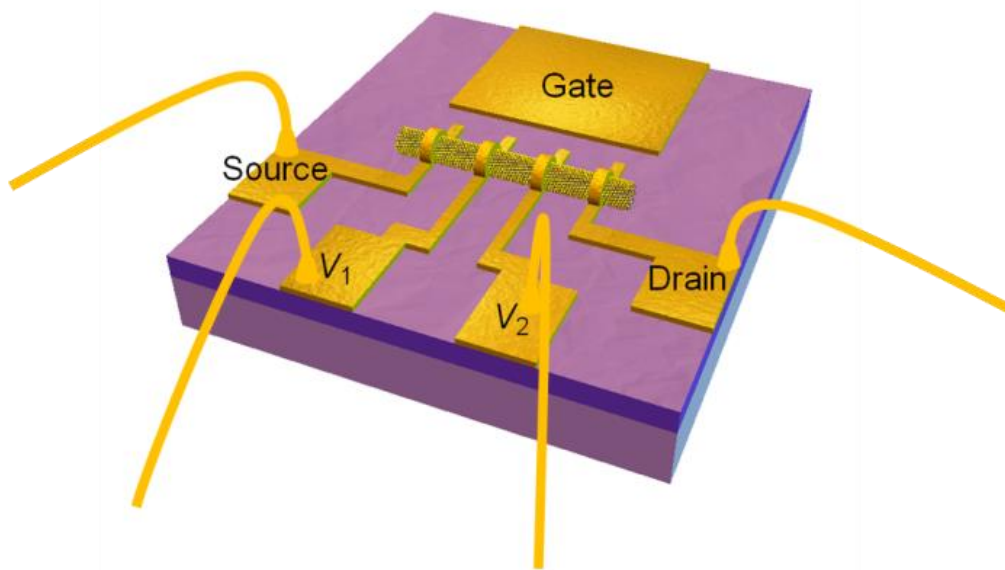


Figure 2-9: The schematic figure of the WS₂ NT device.

The schematic figure of the WS₂ NT device is shown.



Figure 2-10: The photo of wire boding machine.

The photo of wire boding machine is shown. The ground lead is shown in red box.

3-2-4 Ionic liquid droplet putting

A schematic figure of the WS_2 NT device with four-terminal measurement configuration (see chapter 3.3 Transport measurements) is shown in Figure 2-11: **The schematic figure of the WS_2 NT device with ionic liquid.** The Ionic liquid droplet is put on the top of the WS_2 NT sample, covering the whole WS_2 NT sample and also the gate electrode, but not covering the electrode pad.

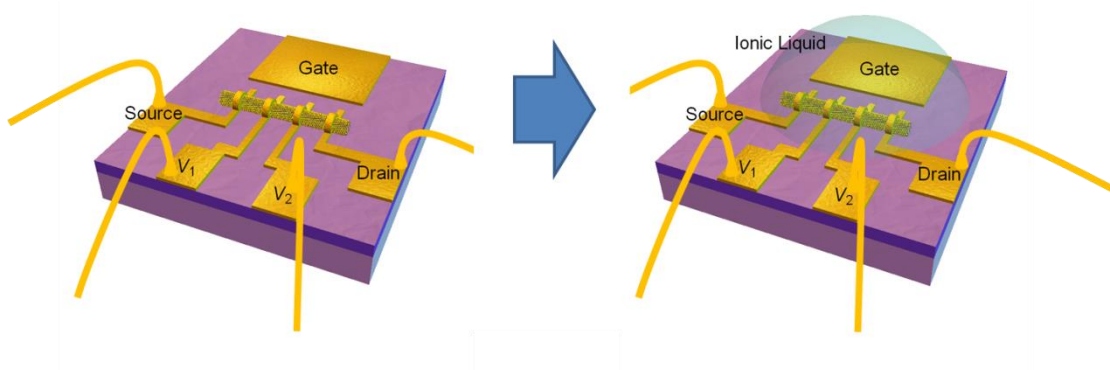


Figure 2-11: The schematic figure of the WS_2 NT device with ionic liquid.

The device after wire bonding procedure is shown (left), the finished EDLT device is shown (right).

2-3 Transport measurements

In this section, the experimental technique of transport measurements will be briefly introduced. The four-terminal measurement is useful for measure tiny device with low resistance, which will be discussed in the first part. The experimental setups will be also shown in the following part, especially for the sensitive measurements by using lock-in amplifiers.

2-3-1 The four-terminal measurement

The intrinsic resistivity of sample is very important for the physical property measurement. However, there always includes errors during measurement, such as thermal fluctuation and systematic error of the experimental setups. The thermal fluctuation error cannot be avoided when measuring physical properties, but the error originating from experimental setups and bad qualities of sample can be partly avoided by carefully designed measurement procedures. Such four-terminal measurement technique is a good example of the well-designed measurement procedures.

Because our target material is insulating or semiconducting sample, while fabricated electrodes are metal, there always exists the contact resistance. On the other hand, since our target sample is very tiny, its resistance is very low compared with contact resistance. Hence, the contact resistance cannot be ignored and highly affect measurement results.

If we naively perform like what students learn in middle school to measure the resistance of the sample, that is, the two-terminal resistance measured by dividing voltage via voltmeter and current via ammeter.

$$R_{2T} = \frac{V}{I} = R_{XX} + R_{CD} + R_{CS} \quad (2.1)$$

This results is totally wrong because we cannot discuss anything about intrinsic properties and everything is hidden behind contact resistance, as shown in Figure 2-12.

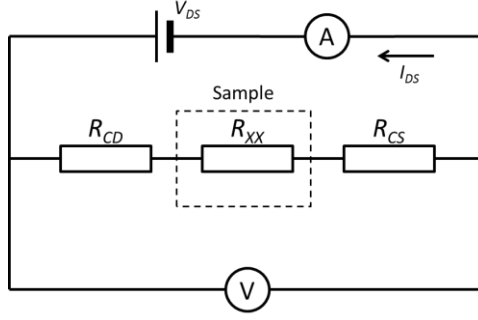


Figure 2-12: Schematic equivalent circuit of usual two-terminal measurement.

In figure, R_{XX} denote the sample resistance, R_{CD} and R_{CS} denote the contact resistance of drain and source side, respectively.

However, if we just measure the resistance of a part of the sample, we have the chance to measure the resistance accurately. This is called four-terminal measurement, and the equivalent circuit is shown in Figure 2-13. In addition to source and drain electrodes, another two electrodes as a pair are connected to the sample between the previous two electrodes. These two additional electrodes are called voltage probes. When the source-drain voltage (V_{DS}) is applied, the source-drain current (I_{DS}) is measured by an ammeter, while the voltmeter detects the real voltage drop of the part of the sample between these two voltage probes. The voltage drop by contact resistance R_{CL} and R_{CR} can be ignored because the voltmeter has much larger inner resistance and the current through voltmeter (I_V) is almost zero. The current through the part of the sample between these two voltage probes is basically equal to I_{DS} . Hence, the resistance of the part of the sample between these two voltage probes can be calculated by

$$R_{4T} = \frac{V}{I} = R_{XX} \quad (2.2)$$

This is the intrinsic property of the resistance of the sample.

If we further know the length of channel L , then the measured resistance can be converted into the one-dimensional resistivity and conductivity of the WS_2 NT sample.

$$\rho_{1D} = \frac{R_{4T}}{L} \quad (2.3)$$

$$\sigma_{1D} = \frac{1}{\rho_{1D}} = \frac{L}{R_{4T}} \quad (2.4)$$

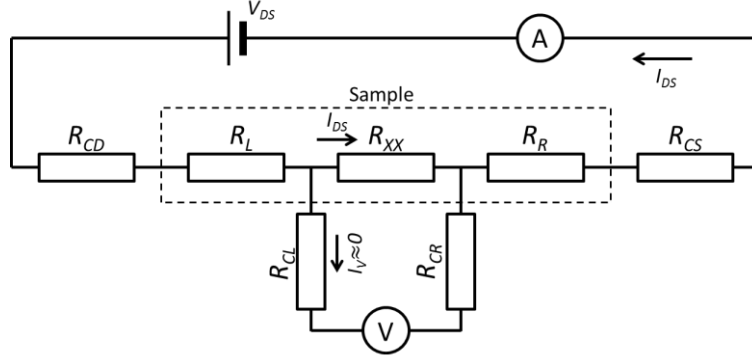


Figure 2-13: Schematic equivalent circuit of usual four-terminal measurement.

In figure, R_{XX} denote the sample resistance, R_{CD} and R_{CS} denote the contact resistance of drain and source side, respectively, and R_L and R_R denote the sample resistance of left side and right side, respectively. In addition, R_{CL} and R_{CR} denote the contact resistance of left side and right side, respectively.

2-3-2 Measurement systems

All of the transport measurements have been done in a physical property measurement system (PPMS) with a Horizontal Rotator. The PPMS system is made by Quantum Design Company, shown in Figure 2-14. With the help of PPMS, we can change the environment surrounding the sample through controller and measure the physical properties of the sample.

We establish the control system as well as the phase-sensitive measurement system in order to perform the transport measurements up to higher accurate level, as shown in Figure 2-15. In Figure 2-14, the direct current (DC) measurements can be performed by source meter and nano-voltmeter, and the alternative current (AC) measurements can be performed by lock-in amplifiers. For the use of EDLT device, we use AC current to carry out the transport properties of the sample and use DC source meter to apply ionic liquid gating on the sample. In addition, we can write codes on the control computer to control these meters and automatically perform phase successive measurements with different aims.

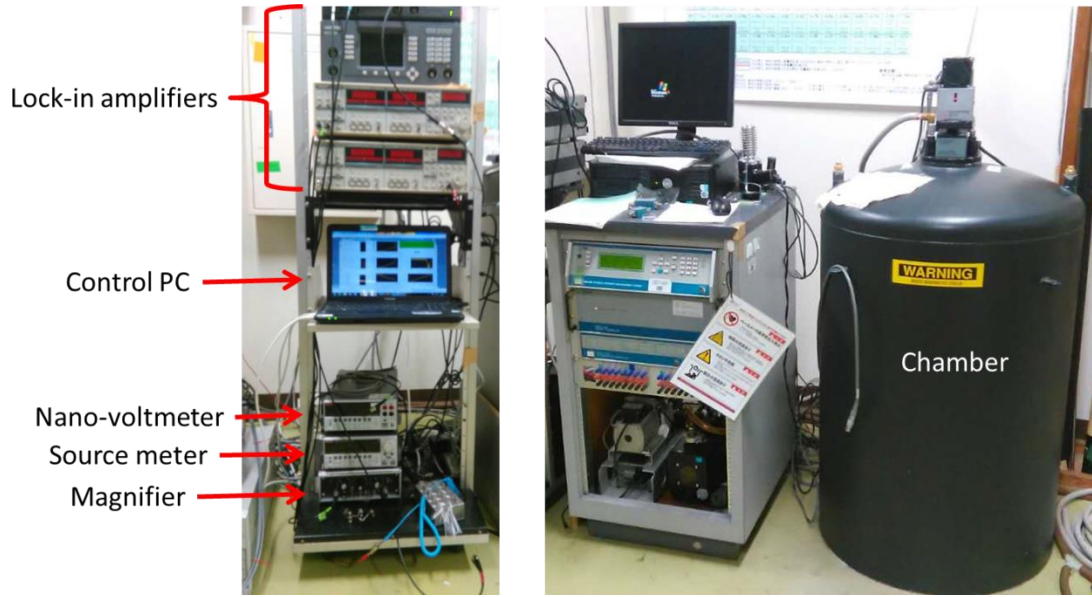


Figure 2-14: The transport measurement system.

The PPMS chamber (right) and the controller systems (left) are shown. In the left figure, lock-in amplifiers, control computer, nano-voltmeter, source meter, and magnifier are pointed out respectively.

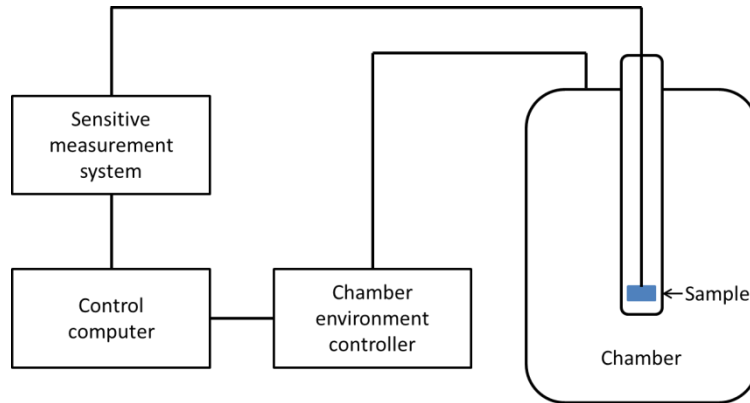


Figure 2-15: The schematic figure of sensitive measurements system.

The schematic figure of sensitive measurements system

The horizontal rotator is an accessory of the PPMS system, which can be used to rotate the sample when the sample is inside the chamber. The rotating angle ranges from -10° to 370° . It is necessary in the measurements of WS_2 NT sample. The horizontal rotator consists of a motor and the rotator body (Figure 2-16). The motor is connected to the PPMS controller and coupled to the rotator body, located at the top of the chamber. The rotator body is the inset inside the chamber. At the end of the rotator body, the

rotator is shown in figure 3.16 (2), which is the place to attach to the sample holder (figure 3.16 (1)). The pin configuration is asymmetric and defines one direction to attach to the sample holder.

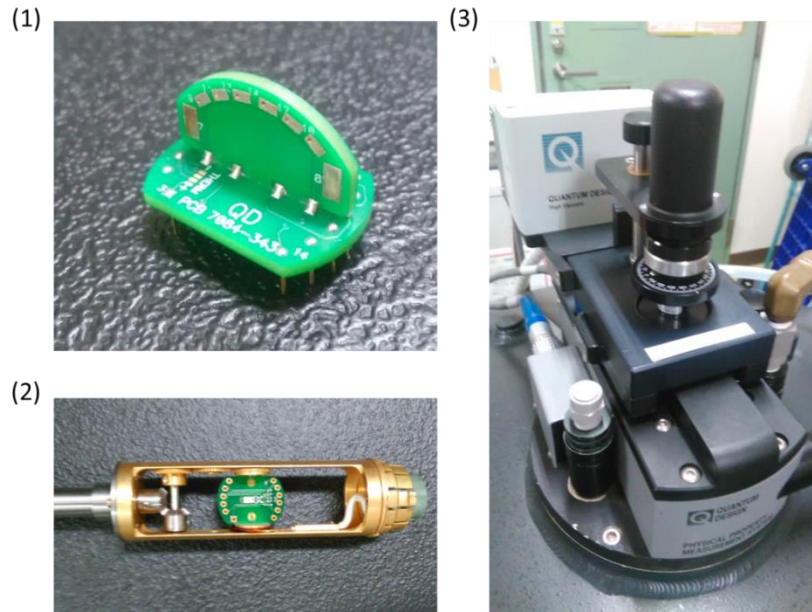


Figure 2-16: The horizontal rotator.

(1) The sample holder of horizontal rotator. (2) The rotator body of horizontal rotator. (3) The motor of horizontal rotator.

2-3-3 Method of transport measurement

All the transport measurements have been done in one Physical Property Measurement System (PPMS) under He-purged and High-vacuum environments.

We perform the phase-sensitive measurement through AC mode, and measure both the first and the second harmonic signal via lock-in amplifiers as shown in Figure 2-17, in order to carry out both the ohmic resistance and nonreciprocal resistance. The harmonic signal inputs from source to drain, and two voltage probes measure the voltage drop, and the first and the second harmonic component is measured via two lock-in amplifiers, respectively.

The ionic liquid gating is applied at 300 K with sweeping rate of 50 mV/s under high-vacuum condition, in order to reduce the influence of the air or other gas on the gate performance.

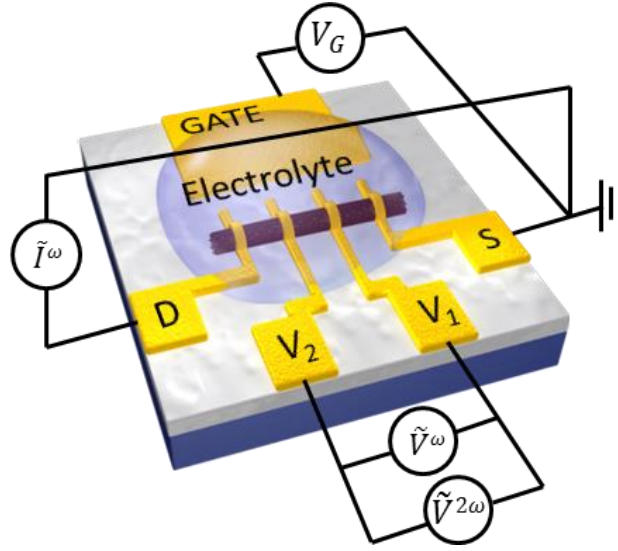


Figure 2-17: The schematic figure of the phase-sensitive measurement.

The schematic figure of the phase-sensitive measurement is shown, in which the first and second harmonic signals are measured simultaneously by individual lock-in amplifiers.

In the temperature dependence measurement, we first cool down to 200K with a scanning ratio 1 K/min after ionic liquid gating and intercalation process under high-vacuum environment and fixed gating voltage, and then we change to He-purged mode and release gate voltage to zero, and keep cooling down to 10 K. Because we use horizontal rotator, the heat contact is not so good, we should use He-purged mode especially in low temperature in order to detailed control of temperature. On the other hand, the ionic liquid freezes about 240 K, so we change the environments inside the chamber at 200 K. Hence, we decide that the He-purged mode is used when the temperature is lower than 200 K and the high-vacuum mode is used when the temperature is higher than 200 K.

When the temperature is lower than 10 K, we cool down or warm up temperature by 0.2 or 0.1 K/min. We also sweep magnetic field at fixed temperature, 100 Oe/s for range up to 9 T or 50 Oe/s for range up to 2 T. The phase-sensitive measurements have been done by applying constant alternative source-drain current with frequency 13 Hz, and both the first harmonic and the second harmonic signals have been measured by lock-in amplifier. During the phase sensitive measurements, the second harmonic signal had about $\pi/2$ phase-shift and agreed with theoretical prediction, and all of the critical data was obtained from y -component which reflected $\pi/2$ phase-shift.

Chapter 3

Sample characterization

In this chapter, the obtained WS₂ NT sample has been characterized through transmission electron microscope (TEM), electron diffraction (ED) analysis and scanning electron microscope (SEM), with the help from Dr. Tomoka Kikitsu, Dr. Daishi Inoue, and Dr. Daisuke Hashizume, those who are researchers in RIKEN. The present results indicate the chiral structure of WS₂ NT [86].

3-1 Transmission electron microscope image

The structure of the WS₂ NTs was determined by transmission electron microscopy (TEM) and related techniques, including electron diffraction (ED) and energy-dispersive X-ray spectroscopy (EDS). Figure 3-1 shows details of two typical NTs with a similar outer diameter but with different core characteristics. TEM images have been taken by JEM-2100F (JEOL Ltd.) with accelerating voltage of 200 kV in RIKEN.

In Figure 3-1, both empty and filled multi-walled WS₂ NT sample are shown. A clear empty WS₂ NT is shown in Figure 3-1 (1) to (3). The inner and outer diameters of the empty WS₂ NTs are estimated as 107 nm and 132 nm, respectively. The number of the layers of the wall is counted about 20 ± 1 , varying from place to place, due to the stacking fault.

More than 90% of the WS₂ NT we have observed had a core-shell structure, and one of the open-ended WS₂ NT is shown in Figure 3-1 (4) to (6). The inner and outer diameters of the open-ended WS₂ NT are estimated as 80 nm and 63 nm, respectively.

The number of layers also changes from place to place. On the surface of the core material (Figure 3-1 (6)), a typical lamellar structure is observed, which is strongly suggestive of the existence of WS₂ also in the core material. In both types of NTs, the shell shows a very nice lamellar structure with the distance between layers estimated as 0.7 nm, which is similar to the interlayer distance of WS₂ crystal with 2H structure. Compared with the shell part, the core part does not show any well-ordered pattern in Figure 3-1 (5).

According to the TEM-EDS (Electron Diffraction x-ray Spectroscopy) analysis, both shell and core part are made from tungsten and sulfur with ratio about W : S = 1 : 2, and without oxygen (Figure 3-2), indicating the complete sulfurization on the tungsten suboxide whiskers during WS₂ NT sample synthesis. The core part may be also made from WS₂ but disordered. Because of the observation of the Little-Parks oscillation, only the outer shell region contributes to the superconductivity realized by ionic liquid gating.

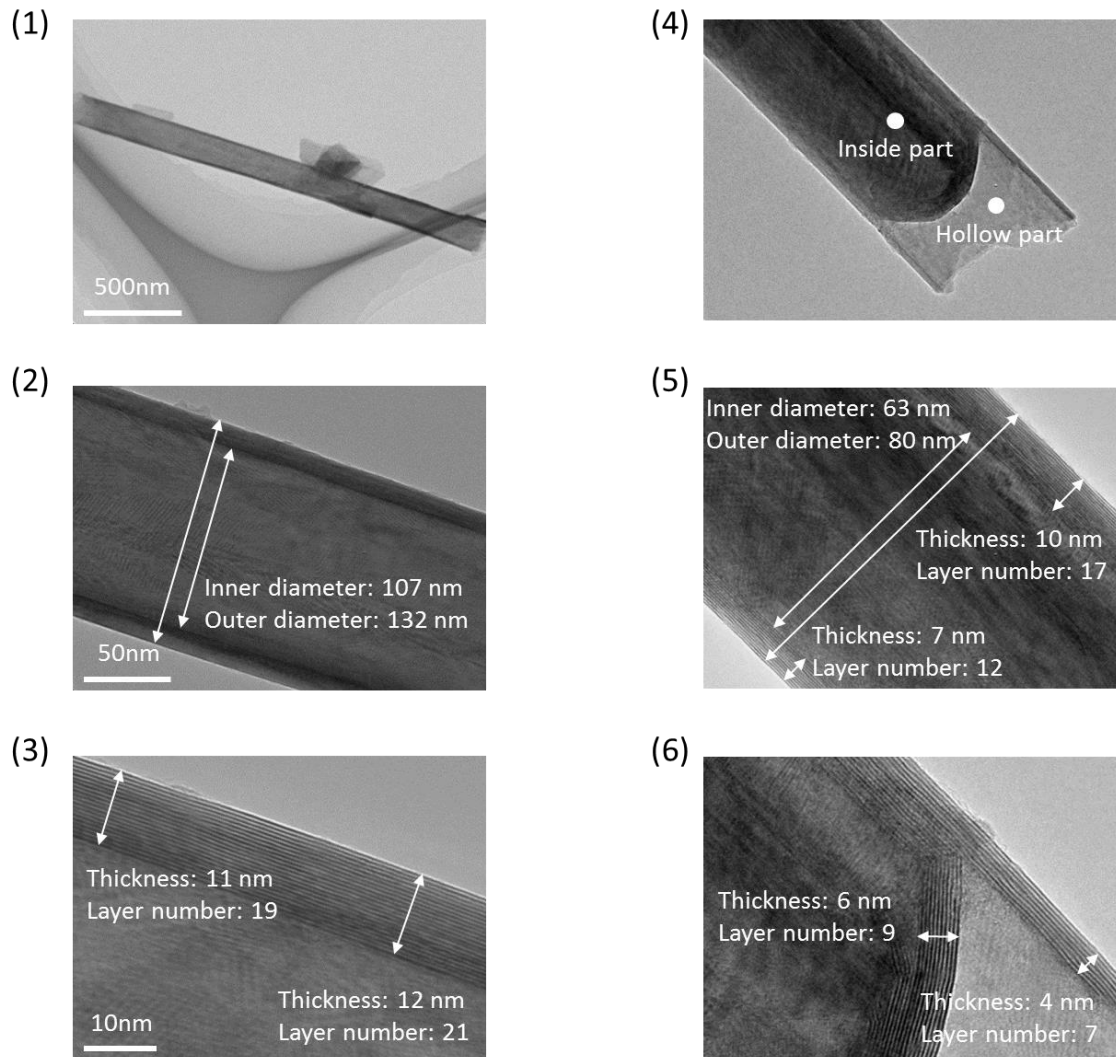


Figure 3-1: The TEM figure of WS₂ NT sample.

(1)(2)(3) The TEM figure of a hollow cylindrical WS₂ NT. (4)(5)(6) The TEM figure of another open-ended WS₂ NT filling with a core material. (1) The TEM image of an empty WS₂ NT. (2) The inner and outer diameter of the empty WS₂ NT are estimated as 107 nm and 132 nm, respectively. (3) The number of the layers of the wall is counted about 20 ± 1 . (4) The TEM image of another open-ended WS₂ NT. (5) The inner and outer diameters of the open-ended WS₂ NT are estimated as 80 nm and 63 nm, respectively. The number of layers of the wall is varying depending on the position. (6) On the surface of the core part, a typical lamellar structure is observed.

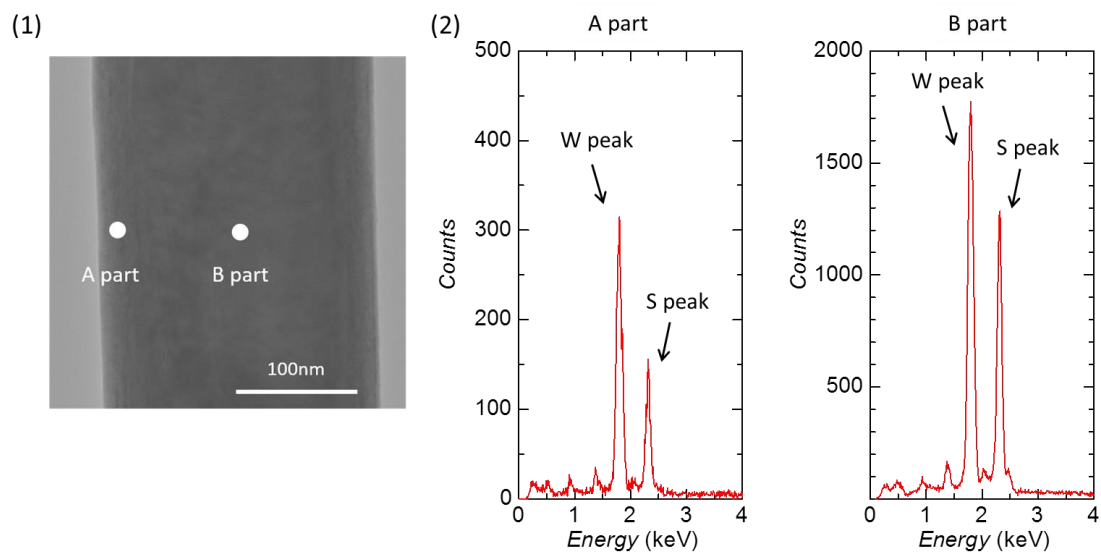


Figure 3-2: TEM-EDS (Energy Dispersive X-ray Spectroscopy) component analysis.

(1) The TEM image of WS₂ NT filled with a core material. (2) The EDS spectra of A part (left) and B part (right). Both A and B parts basically shown only tungsten (W) and sulfur (S) peaks.

Element	Peak position (keV)	A part (%)	B part (%)
W	1.774	35.1	36.3
S	2.307	64.9	63.7

Table 3-1: The quantitative analysis of both A part and B part.

For both A and B parts, the composition ratio is almost the same as W : S = 1 : 2.

3-2 Diameter distribution of the WS₂ NT sample

In Figure 3-3, the distribution of the outer diameter of the WS₂ NT sample is shown. This analysis is based on counting 50 WS₂ NTs sample analyzed by TEM. The histogram indicates a board peak around 100 nm. If we want to use the estimated value of the outer diameter, then 100 nm is the proper value. This diameter is comparable to the values estimated from the Little-Parks oscillation (please see Chapter 6 Little-Parks oscillation).

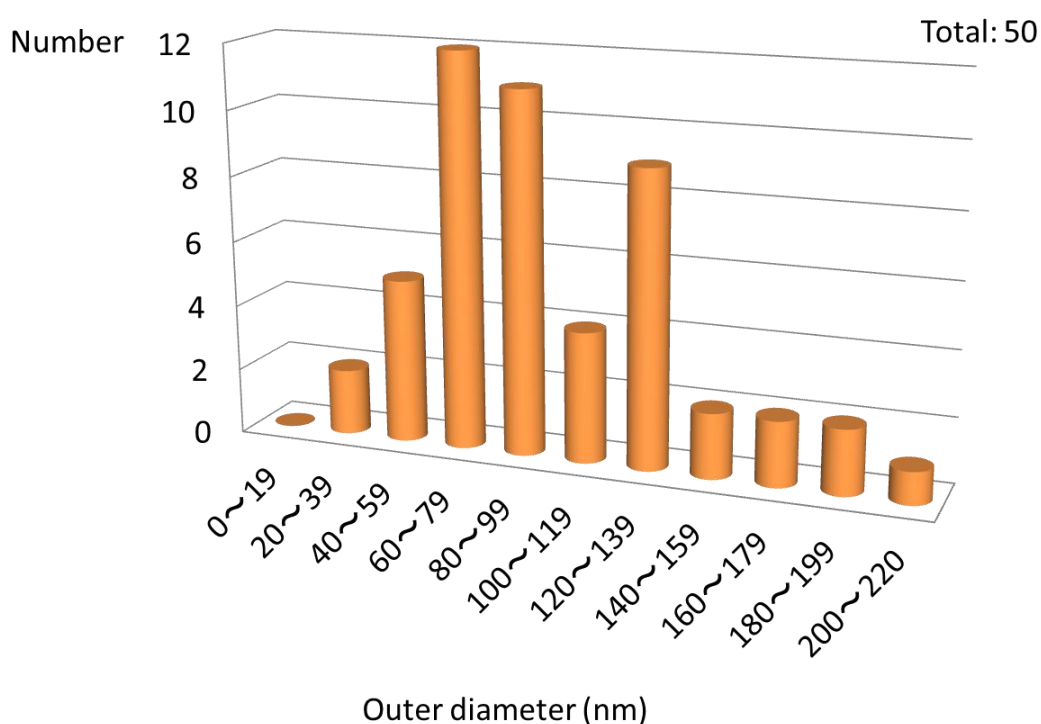


Figure 3-3: The distribution of the outer diameter of the WS₂ NT sample.

Total number of samples is 50 and there is a board peak around 100 nm.

3-3 Electron diffraction analysis

Figure 3-4 displays the schematic figures of the expected electron diffraction pattern for the three typical NTs of $2H\text{WS}_2$.

The zig-zag type of NT (Figure 3-4 (1)) shows a set of six points formed as an upright hexagon (Figure 3-4 (4)), while the arm-chair type of NT (Figure 3-4 (3)) shows a set of six points formed as a hexagon tilted by 30 degrees from the tube axis (Figure 3-4 (6)). Because for the zig-zag type and arm-chair type, the top and bottom layer are accidentally coincident (see from the top view as Figure 3-4 (1) and (3)), although the top and bottom layer both contribute to the electron diffraction pattern, the electron diffraction pattern generated by top and bottom surface layers are also coincident.

On the other hand, for the chiral type NT, the electron diffraction pattern is composed of two sets of six points formed hexagonal pattern and tilted with the chiral angle θ ($0 < \theta < 30^\circ$), and each of which originates from the top and bottom layer of the NT. Because the tilted angles are opposite for the top and bottom surface layer, the electron diffraction pattern tilts with the opposite angle and becomes double hexagons with tilted angles from the tube axis.

Figure 3-5, Figure 3-6, Figure 3-7 and Figure 3-8 are typical real electron diffraction pattern of multi-walled WS_2 NTs.

The electron diffraction pattern of tube A in Figure 3-5 is formed of one hexagon aligned to the tube axis (yellow hexagon in Figure 3-5) and a set of two tilted hexagons (white hexagons in Figure 3-5), indicating that tube A is multi-walled and composed of the zig-zag and chiral NTs.

On the other hand, the tube B in Figure 3-6 is formed of one hexagon with tilting angle of 30° together with a pair of twisted hexagons, indicating that tube B involves the arm-chair and chiral NTs.

Furthermore, Figure 3-7 and Figure 3-8 show more complicated diffraction pattern, proving tube C and D include tubes with a variety of chirality. The observation of the electron diffraction patterns shown in Figure 3-5, Figure 3-6, Figure 3-7 and Figure 3-8 indicate that almost all of the multi-walled WS_2 NTs contain chiral tubes.

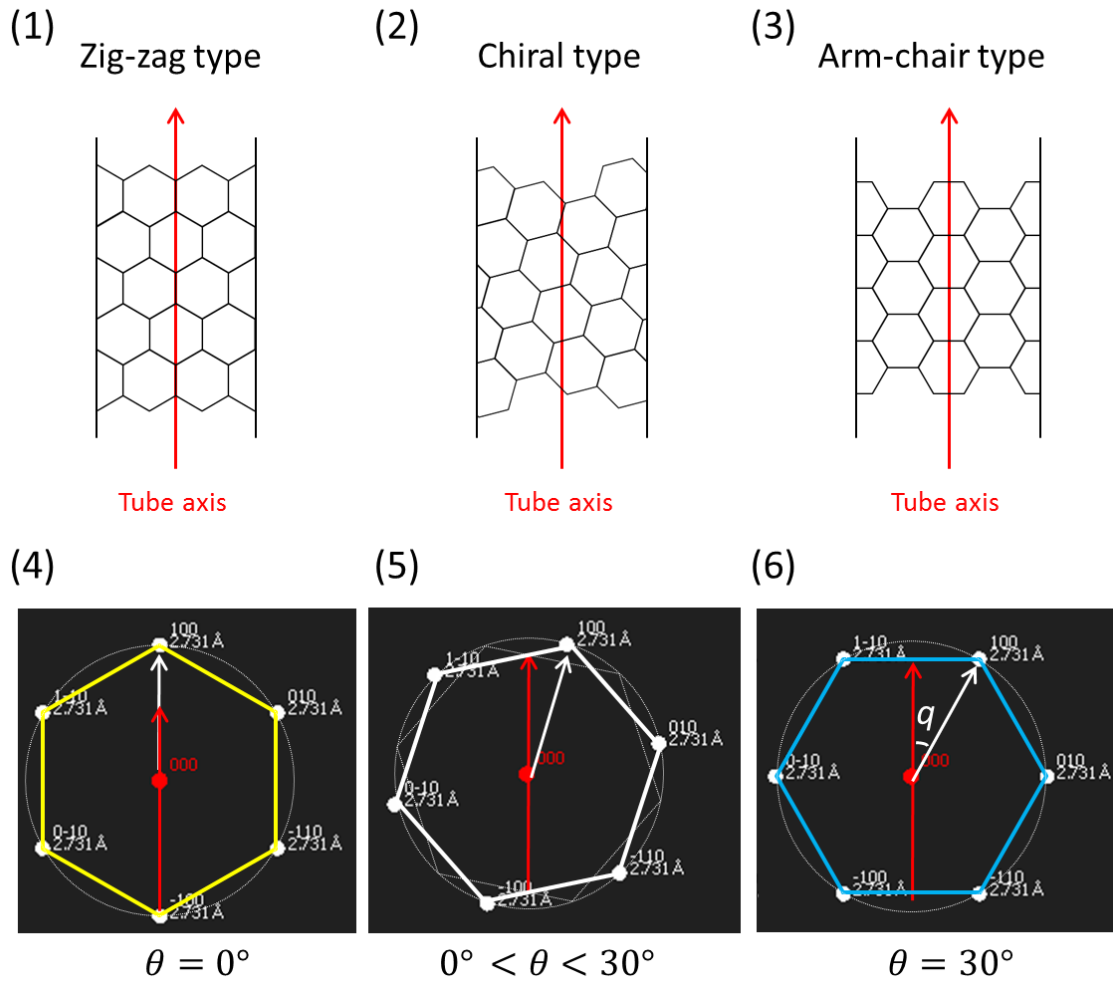


Figure 3-4: The schematic figure of electron diffraction pattern.

(1)(2)(3) The illustration of the three typical NT structure, the red arrow represents the NT axis direction. (1) Zig-zag type. (2) Chiral type. (3) Arm-chair type. (4)(5)(6) The expected electron diffraction pattern for each structure. (4) For the zig-zag type, the electron diffraction pattern is made up of six points formed hexagonal pattern with zero chiral angle. (5) For the chiral type, the electron diffraction pattern is composed of two sets of six points formed hexagonal pattern, each of which originates from the top and bottom layer of the NT. (6) For the arm-chair type, the electron diffraction pattern is made up of six points formed hexagonal pattern with chiral angle equals of 30° .

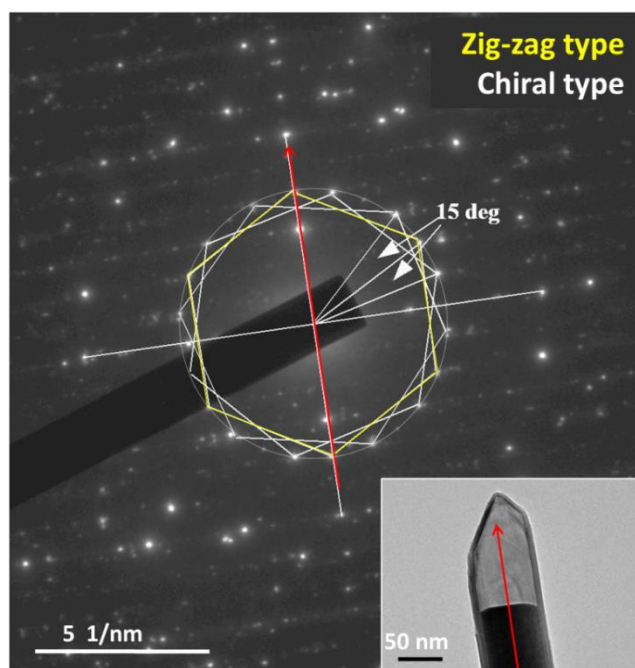


Figure 3-5: The electron diffraction pattern of tube A.

There are zig-zag and chiral tubes in the multi-walled tube A. The inset shows the TEM image of this tube.

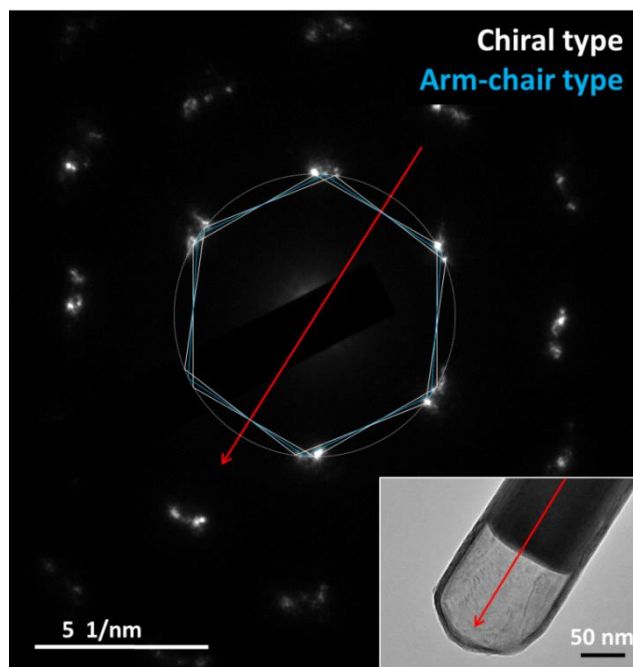


Figure 3-6: The electron diffraction pattern of tube B.

There are arm-chair and chiral tubes in the multi-walled tube B. The inset shows the TEM image of this tube.

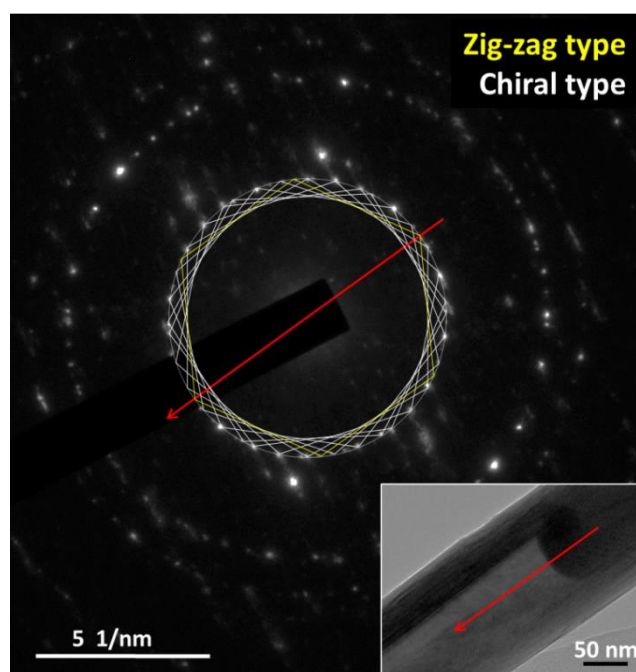


Figure 3-7: The electron diffraction pattern of tube C.

There are zig-zag and multi-chiral tubes in the multi-walled tube C. The inset shows the TEM image of this tube.

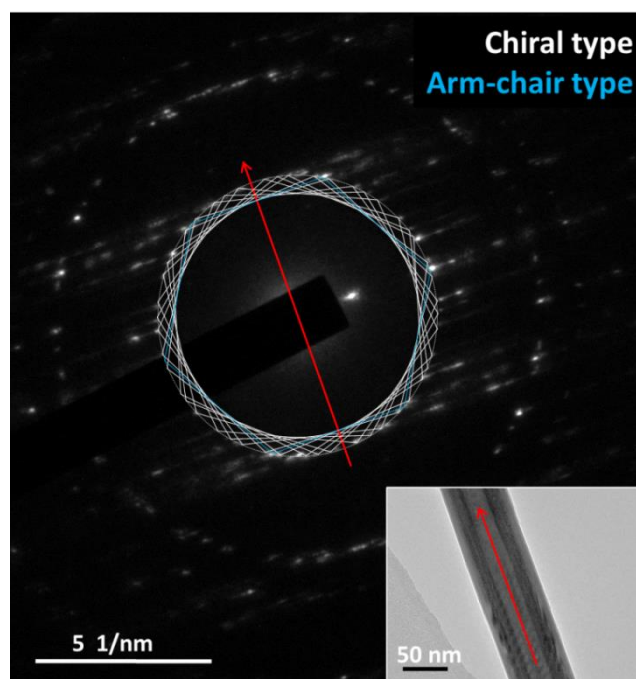


Figure 3-8: The electron diffraction pattern of tube D.

There are arm-chair and multi-chiral tubes in the multi-walled tube D. The inset shows the TEM image of this tube.

3-4 Scanning electron microscope image of WS₂ NT device

The device picture via scanning electron microscope (SEM) is shown in Figure 3-9. The WS₂ NT is well-made.

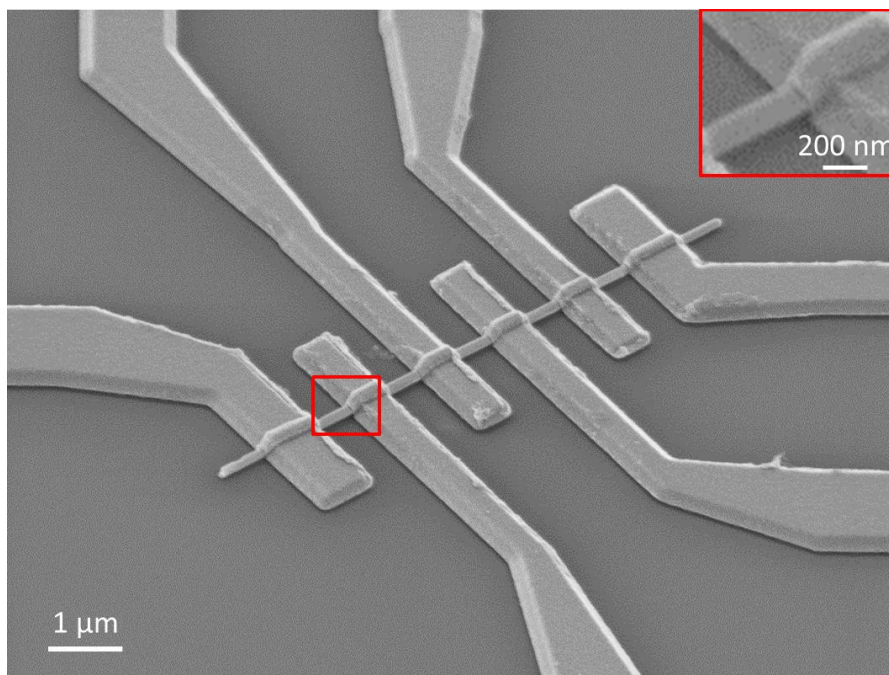


Figure 3-9: SEM image of a WS₂ NT device.

Inset shows the magnified view around the boundary between WS₂ NT and gold electrode.

Chapter 4

Ionic liquid gating on WS₂ NT

In this chapter, the previous research on the field effect on TMD NT will be introduced in chapter 4-1, then the experimental results of ionic liquid gating on WS₂ NT will be discussed in chapter 4-2 and 4-3, for the displaying of electrostatic doping and electrochemist doping, respectively. Finally, the ionic liquid gating induced superconductivity will be shown, further researches on the superconductivity will be discussed in the next chapters.

4-1 From the solid gate to the liquid gate transistor on WS₂ NT

In Chapter 1, the electric double layer transistor (EDLT) technique has been introduced. Here, the effect of field effect transistor (FET) on TMD NT will be introduced, and then a proposal of EDLT on TMD NT will be shown. The experimental results of EDLT on WS₂ NT will be discussed in chapter 4-2, 4-3 and 4-4.

4-1-1 Field effect transistor on WS₂ NT

Here, we summarize the previous research on the FET on TMD NT. People have found a practically insulating WS₂ NT behavior [87] with a band gap of about 2 eV [88], and also negligible field effect mobility [89][90], as well as not so efficient field effect on WS₂ NT [84]. In addition, a complete lack of gate response for MoS₂ NT has been reported [91].

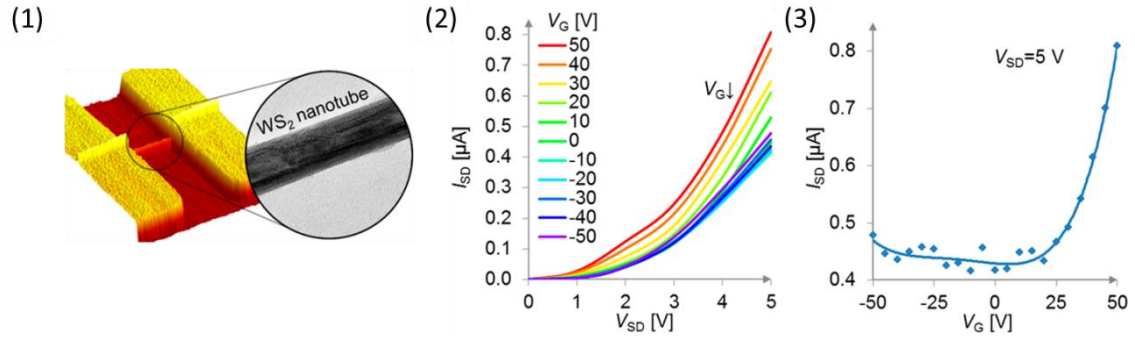


Figure 4-1: The results of the FET on WS₂ NT.

(1) The AFM and TEM images of WS₂ NT FET device and WS₂ NT, respectively. (2) The source-drain current versus the source-drain voltage manipulated by gate voltages. (3) Gate response of the WS₂ NT FET device.

The first experimental report on the FET on WS₂ NT is shown in Figure 4-1. The diagram of source-drain current (I_{DS}) versus the source-drain voltage (V_{DS}) manipulated by gate voltages is shown in Figure 4-1 (2). Most of WS₂ NT FET device performs n-type behavior, as shown in Figure 4-1 (3). The electron mobility estimated from figure is about $\mu \approx 50 \text{ cm}^2 \cdot \text{V}^{-1} \cdot \text{s}^{-1}$. However, there is no previous work on the inorganic FET device. Compared to the Hall mobility of bulk WS₂ sample, where $\mu_H \approx 100 \text{ cm}^2 \cdot \text{V}^{-1} \cdot \text{s}^{-1}$.

4-1-2 A proposal of EDLT on TMD NTs

The usual solid gate is weak for inducing field effect on TMD NTs, and then we propose to use liquid gate for the field effect transistor. There are three advantages of using liquid gate.

First, compared with usual solid gate FET, the liquid gate FET, the EDLT, has been demonstrated to induce ultra-high electric field on the surface ($> 0.5 \text{ V/\AA}$) [92] and have the capability to accumulate more than one order higher carrier density ($> 10^{14} \text{ cm}^{-2}$) even at low bias voltage [44], which is an efficient tool using ultra electric field to control the basic physical parameters of materials.

Second, the liquid gate does not care about the shape of the sample. For the configuration of solid gate, there is charge accumulation on the top and bottom parts of sample. Usually, people work on flake or film, which is basically two-dimensional (2D)

and has a flat, large surface. For this configuration, the solid gate can work well. However, if the sample is not like 2D case but the NT configuration, the solid gate cannot work well, because the top and bottom parts of the sample are narrow. On the other hand, the liquid gate does not care about the shape of the sample, because all of the surface exposed in the liquid can work for the charge accumulation (Figure 4-2).

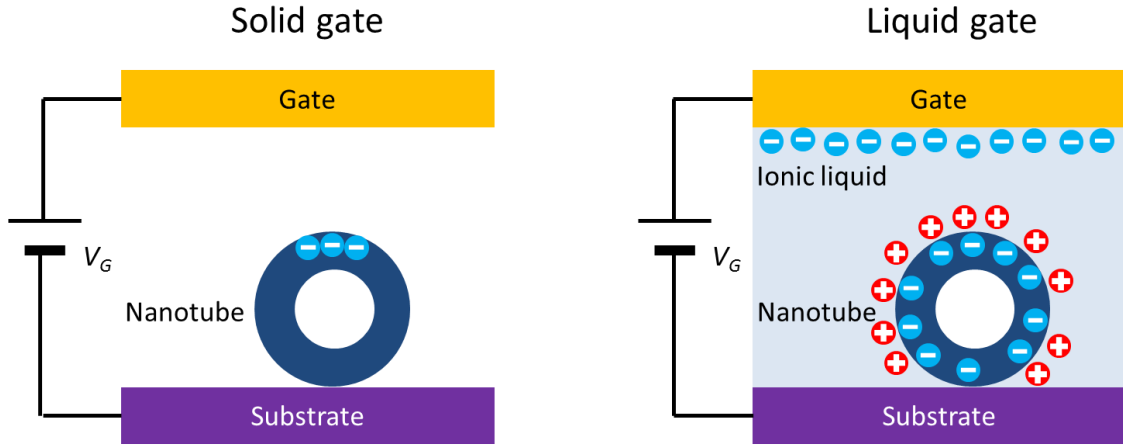


Figure 4-2: The schematic figure of solid gate (left) and the liquid gate (right) on NT configuration.

For the solid gate (left), only the top surface of NT shows field effect, while the entire surface shows field effect for the liquid gate (right) indicating a much better gate response.

Third, according to the previous research of EDLT on TMD materials, there is a possibility to induce superconductivity in WS_2 NT. Recent systematic studies have been clarified that lots of TMD materials including WS_2 , which are semiconductors without doping, exhibit superconductivity under the ionic gating [59][60]. Even if the superconductivity in WS_2 NT cannot be realized within electrostatic doping region, we still have chance to induce superconductivity in electrochemist doping region [60][63].

Hence, in summary, we expect the EDLT will work on WS_2 NT sample, display a significant field effect response, and even induce superconductivity in WS_2 NT. The research of EDLT effect on WS_2 NT is of great interest.

4-2 Electrostatic doping by ionic liquid medium

In this part, the experimental results of the EDLT on WS_2 NT will be discussed. In the experiments, we use KClO_4/PEG as a gate medium, because this ionic liquid

displays a significant field effect on TMD materials, especially for WS₂ flake, according to the literature [60].

4-2-1 Ambipolar transfer curve and electron hole symmetry

The ambipolar transport is shown in Figure 4-3. The source-drain current (I_{DS}) of the individual WS₂ NT device against the gate voltage (V_G) between -2 V to 3 V. The WS₂ NT EDLT device nicely operates in an ambipolar mode, in a similar manner to the 2D devices [48], showing marked contrast with the unipolar gate response of WS₂ NT in the solid gated FET [84]. This indicates the strong gate coupling of the presently used ionic medium [60]. The transistor operation is most likely in the electrostatic mode in this regime, considering the ambipolar behavior is reversible and repeatable as shown in Figure 4-3 (2). Such ambipolar transfer curve indicates the electron hole symmetry in the band structure, and both electrons and holes can be the charge carrier to perform the transport properties.

However, the transfer curve shows large hysteresis in the electron doped side, while a little hysteresis in the hole doped side to be compared. During multiple scanning of the ambipolar transfer curve, the maximum values of the I_{DS} in the electron doped side keep decreasing, while the maximum values of the I_{DS} in the hole doped side basically keep unchanged. These two asymmetries may indicate more complex nature of the electronic state of WS₂ NT, such the effective mass, scattering effect, impurity energy level inside band gap, and other relevant asymmetric quantities of electron and hole. On the other hand, the ionic liquid we used is KClO₄/PEG, in which the positive ions (K⁺) and negative ions (KClO₄⁻) are inequivalent. Above asymmetric properties of ambipolar curve may also originate from the asymmetry of the two opposite ions, which remains further researches.

The ambipolar transfer curve with a high on/off ratio ($> 10^2$) has been observed for both hole and electron sides. The threshold voltages for the electron side and the hole side can be determined by linearly extrapolating the I_{DS} - V_G curves to be zero, and then we further determine the work function of the WS₂ NT. According to Figure 4-3 (1), the work function is estimated about 2.4 eV, consistent with previous research on WS₂ NT with a band gap about 2 eV [87]. In addition, most of measured WS₂ NT samples show electron doped ambipolar transfer curves. The threshold voltages for the electron side (usually about 1 V) and the hole side (usually about 1.4 V) are not symmetric,

indicating the electron doped behavior of WS₂ NT sample, coincides with previous research [84]. Based on careful consideration of the capacitance of the WS₂ NT sample [93], the mobility of electron or hole can be estimated by Figure 4-3 (1), which is about $\mu \approx 1.4 \text{ cm}^2 \cdot \text{V}^{-1} \cdot \text{s}^{-1}$.

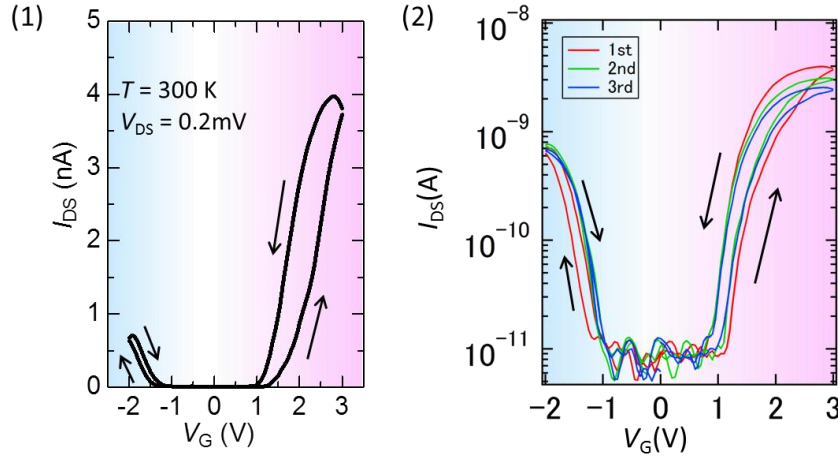


Figure 4-3: The ambipolar transfer curve of WS₂ NT EDLT device.

(1) (2) The source-drain current (I_{DS}) of the individual WS₂ NT device against the gate voltage (V_G) between -2 V to 3 V at 300 K . Red background indicates the electron doped side while blue background indicates the hole doped side. (1) The ambipolar transfer curve in the linear axis. (2) The reversible and repeatable ambipolar transport curves in the logarithm axis. The ambipolar transport curve for the first scan is the same experimental data displayed in (1).

4-2-2 Temperature dependence of ambipolar transfer curve

The ambipolar transfer curve at various temperatures ranging from 200 K to 350 K is shown in Figure 4-4. The starting temperature is 300 K , cooling down to 200 K of the speed of 1 K/min , and then warming to 350 K with the same scan speed. This WS₂ NT sample is electron doped with the band gap to be estimated about 3 V .

With the decreasing of the temperature as shown in Figure 4-4 (1), the gate response changes from the ambipolar transfer curve to the unipolar transfer curve at about 260 K , and then no gate response is observed below 240 K due to the ionic liquid freezing. On the hole doped side, the gate response firstly disappears, while the gate response on the electron doped side still remains obvious signals until 240 K . In

addition, the gate response displays the enhancement of hysteresis on the electron doped side at relative low temperature.

On the other hand, when the increasing of temperature, the gate response displays another hysteresis on temperature, the gate response appears on the electron doped side above 260 K, while on the hole doped side, the gate response appears above 280 K. When the temperature comes back to the 300 K, the ambipolar transfer curve does not come back.

Then, the temperature keeps increasing up to 350 K, as shown in Figure 4-4 (2), the ambipolar transfer curve becomes better, and finally disappears with the broken of the WS₂ NT sample.

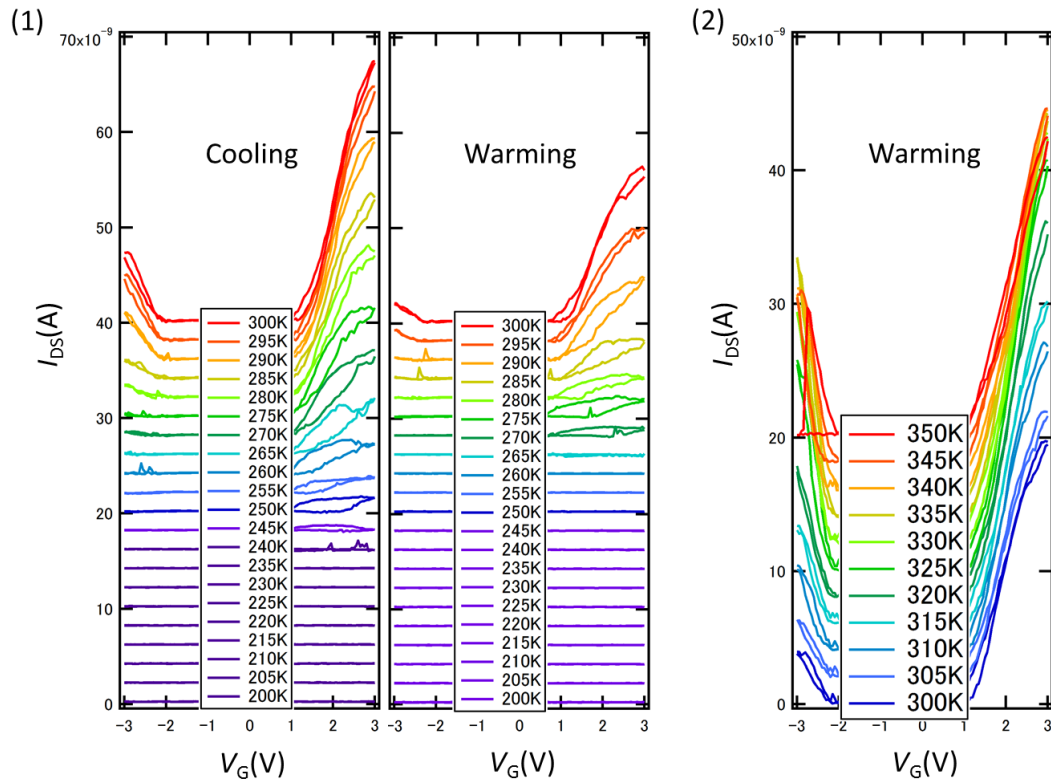


Figure 4-4: The ambipolar transfer curve of WS₂ NT EDLT device at different temperature.

(1) The ambipolar transfer curve at various temperatures ranging from **200 K** to **300 K**. A large hysteresis of the temperature reaction is shown. (2) The ambipolar transfer curve at various temperatures ranging from **300 K** to **350 K**. At **350 K**, the WS₂ NT has broken in hole doped side.

The maximum I_{DS} values of ambipolar transfer curve are determined and displayed in Figure 4-5 both on electron and hole doped side. Figure 4-5 (1) displays the maximum of I_{DS} versus temperature of the cooling process, while the data of the warming process are shown as background. In Figure 4-5 (2), the data of cooling and warming process are shown opposite to Figure 4-5 (1).

The hysteresis on temperature of gate response is clearly seen in Figure 4-5, and is about 20 K. In Figure 4-5 (2), the maximum values of I_{DS} show a domed shape, and reach the peak at about 320 K.

The hysteresis on temperature of gate response implies the slow dynamic process of the glass transition of the ionic liquid. The domed shape of the maximum I_{DS} values points a direction to optimize the effects of EDLT on the WS₂ NT sample.

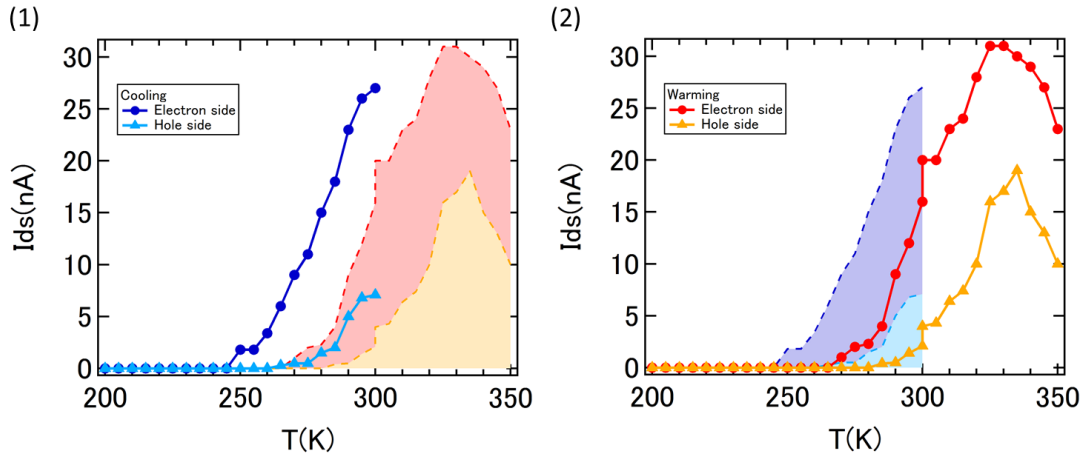


Figure 4-5: The hysteresis of temperature dependence of ambipolar transfer curve.

The hysteresis on temperature of gate response is clearly seen. And the maximum I_{DS} values show a domed shape (in the left), and reach the peak at about 320 K.

4-2-3 Temperature dependence of resistance

The electronic state of the WS₂ NT in ionic liquid electrostatic doping region has been clarified by transport measurement with scanning temperature. As shown in Figure 4-6, the temperature dependence of resistance is modulated by gate voltage. The four-terminal measurements have been performed, and the temperature dependence of resistance shows intrinsic electronic states of WS₂ NT.

In the low gate voltage region, the ambipolar transfer curve is reversible and repeated, indicating the electrostatic doping in the WS₂ NT. The WS₂ NT doped within electrostatic region displays insulating behavior, the resistance keeps increasing when cooling the sample down to 10 K. With the increasing of gate voltage, the resistance of WS₂ NT keeps decreasing, and suddenly jumps down to several hundred ohm and tunes the electronic state become metallic at the gate voltage of 5 V.

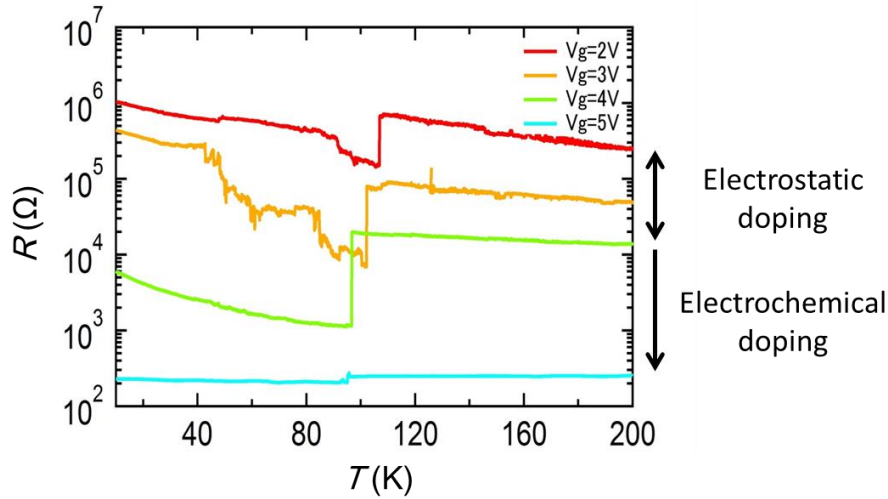


Figure 4-6: Temperature dependence of resistance modulated by gate voltage.

Within electrostatic doping region, the WS₂ NT performs like insulator, while within electrochemical doping region, the WS₂ NT becomes metallic.

4-3 Ionic liquid gating driven intercalation

The intercalation is the electrochemical doping methods in order to realize a much higher electron doping level in the bulk of the sample, instead of on the surface of the sample within electrostatic doping.

A typical intercalation process is shown in Figure 4-7. When the gate voltage was increased up to 8 V at a constant rate of 50 mV/s, the source-drain current displays a saturation indicating the electrostatic doping, similarly to the 2D WS₂ case [60]. When the gate voltage is kept at 8 V for a couple of minutes, another dramatic increase of source drain current by more than two orders of magnitude has been observed as shown in Figure 4-7. This source-drain current increase is presumably attributed to intercalation of K ions into WS₂ NT, which induce a bulk carrier doping with a much higher doping level compared with the doping level of surface doping in electrostatic

region. The intercalation induced by ionic liquid gating provides a powerful technique to realize superconductivity in materials.

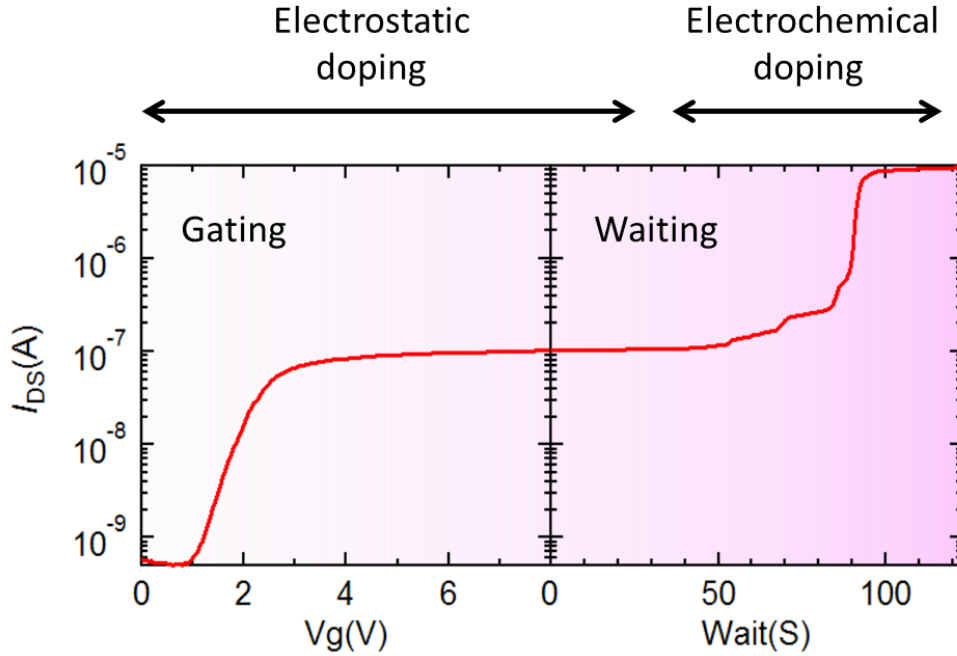


Figure 4-7: A typical intercalation process.

The increase of source drain current during gating displays the electrostatic doping, and the other increase of source drain current during waiting displays the electrochemical doping in which the potassium ions pass into interlayer structure of WS_2 NT and thus the extremely heavy electron doped WS_2 NT is realized by ionic liquid gating.

4-4 Superconductivity induced by the intercalation

The temperature dependence of the resistance of WS_2 NT after intercalation process is shown in Figure 4-8. The resistance firstly shows an anomalous increase above the glass transition of ionic liquid. Then the resistance decreases and behaves like metallic sample. When the temperature is cooled down to 2 K, the superconductivity appears in the K-intercalated WS_2 NT. In contrast to the K-intercalated 2D WS_2 multilayer nanoflake, the superconducting transition is shifted to lower critical temperature and considerably broadened, possibly due to the lower dimensions of NT configuration.

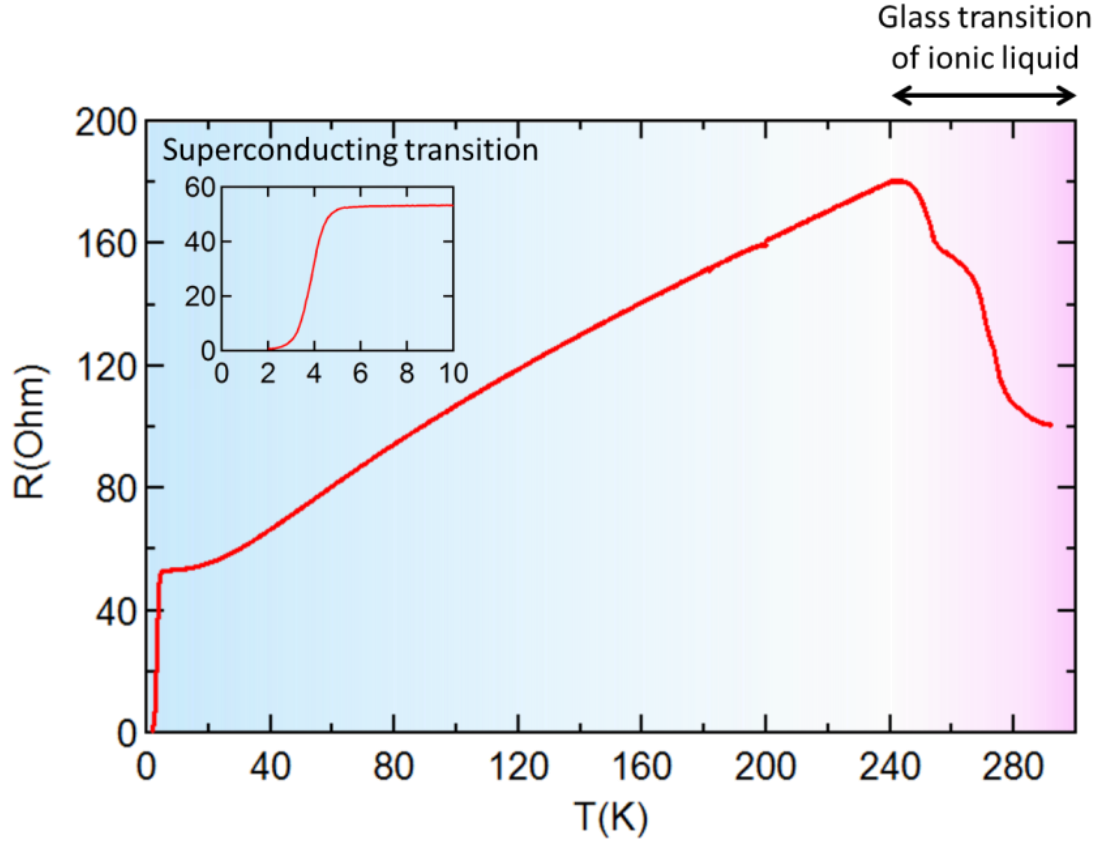


Figure 4-8: Superconductivity induced by the intercalation.

Inset is the magnified figure displaying the superconducting transition with $T_c \approx 4 \text{ K}$.

The gate voltage is kept above 200 K , then released below 200 K .

4-5 Staging effect in gate induced superconductivity

The staging effect is commonly known in layered materials, such as alkali-metal intercalated graphite [94] and TMD materials [60][63]. Especially for the alkali-metal intercalation induced by liquid gating, such staging effect has been clearly displayed. As shown in Figure 4-9 (1), a dramatic reduction of resistance is displayed in lithium intercalated TaS_2 flake, similar to the WS_2 NT case. And in the superconducting phase, in Figure 4-9 (2) and (3), the superconducting dome displays a clear flat roof, indicating a single superconducting phase of staging. Although Figure 4-9 (2) and (3) display two samples with different thickness, the phase diagrams of electronic state are quite similar, in which there exists a robust superconducting phase with fix critical temperature indicating the possible staging phase existing in lithium-intercalated TaS_2 compound [63].

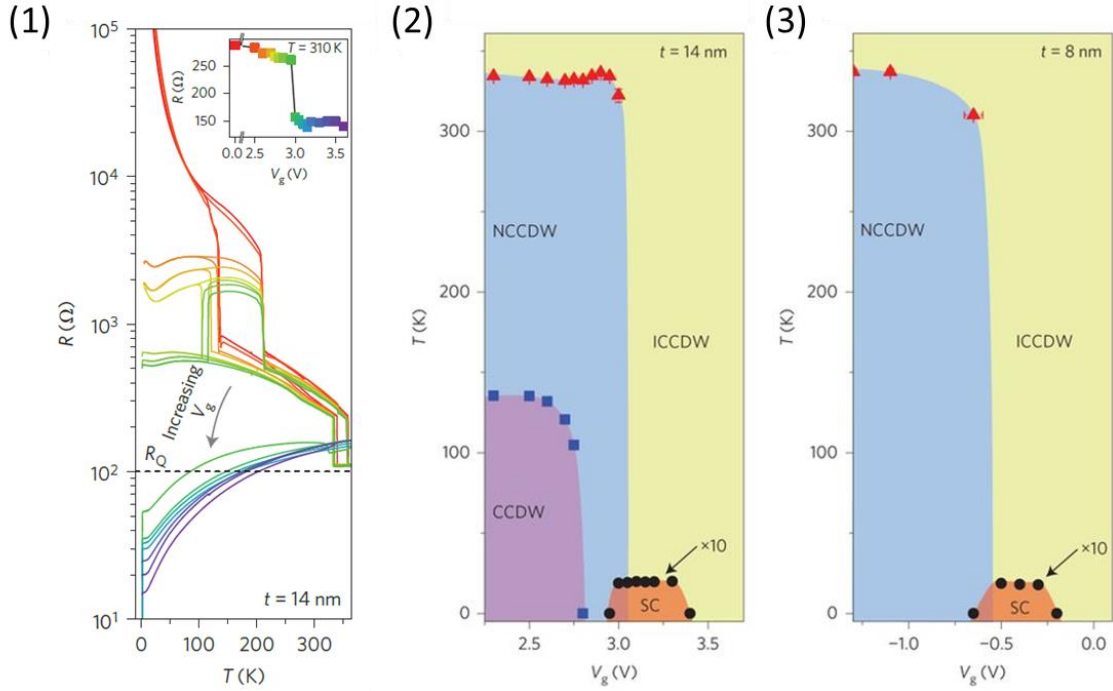


Figure 4-9: The electronic state of lithium-intercalated TaS₂.

(1) The temperature-dependent resistance of lithium-intercalated TaS₂. (2) A phase diagram of electronic state of 14 nm thick lithium-intercalated sample. (3) A phase diagram of electronic state of 8 nm thick lithium-intercalated sample.

For the case of potassium-intercalation in the 2D WS₂ multilayers, the critical temperature $T_c = 8.3$ K is fixed, and does not depend on the carrier density determined by the Hall measurement, as shown in Figure 4-10 adapted from ref. [60]. It is most possible that the superconducting K_xWS₂ is a line phase compound with a fixed value of $x \sim 0.1$, rather than a solid solution, where x and thus T_c are tunable. It should be noted that there is a clear difference between electrostatic and electrochemical doping. In electrostatic region, the doping on the whole surface of the sample is relatively uniform and electronic properties are dependent on carrier density of the surface.

On the other hand, in electrochemical doping, K ions are intercalated between WS₂ layers, and possibly form a stable phase with a distinct value of x , which should be near $x = 0.1$. When the amount of x is off from that of the stable phase, the whole system exhibits the phase separation. Thus, the doping is not uniform. Nevertheless, the superconducting properties such as T_c are determined by this stable superconducting phase, leading to the fixed critical temperature. The carrier density (measured by Hall resistance) is the averaged value over the whole area of the sample, and thus changeable

by gate voltage. Hence, the critical temperature T_c independent on carrier density is observed, as discussed before in ref. [60].

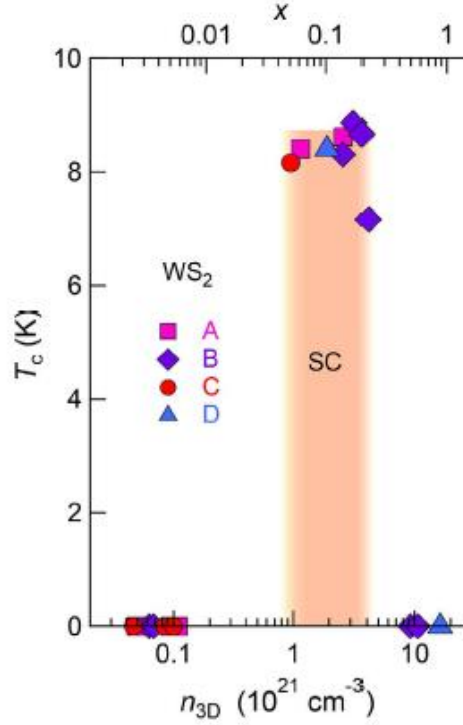


Figure 4-10: The phase diagram of potassium-intercalated WS₂.

The phase diagram of potassium-intercalated WS₂ adapted from ref. [60]. There possibly exists a staging phase and thus a fixed critical temperature of superconductivity.

Importantly, we observed the stable T_c (5.8 K) for WS₂ NT. Figure 4-11 shows the multiple gating processes of the single sample. In Figure 4-11, due to the partially reversible nature of the intercalation, the carrier density is different in every gating process, which is proved by the difference of the resistance in normal state (Figure 4-11). However, observed T_c is still almost the same in every gating process, which also supports the above scenario of staging phase.

Thus, we conclude that the staging phase is essential for the critical temperature of superconductivity and doping uniformity does not affect T_c in electrochemical doping region.

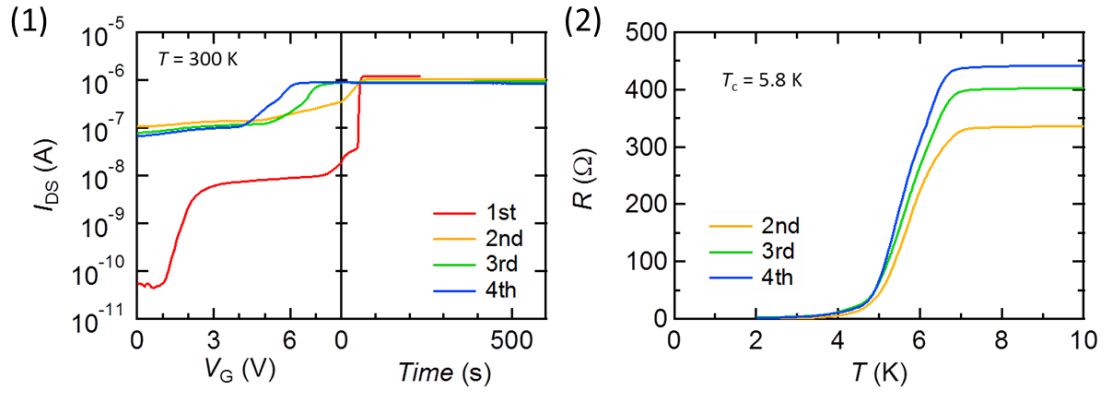


Figure 4-11: Similar T_c in multiple gating processes for both two channels.

(1) Multiple gating processes for intercalation. Once electrochemical doping is realized (1st gate scan, red curve), the gate effect in electrostatic doping region ($V_G < 3$ V) becomes weak and source-drain current I_{DS} never come back to the original value at $V_G = 0$ V. However, it still shows finite gate response from the 2nd time (yellow, green, and blue curves) in large gate voltage region ($V_G > 3$ V), suggesting that the intercalation is partially reversible. (2) Similar T_c for multiple gating processes.

Chapter 5

Superconductivity in individual WS₂ NT

5-1 Introduction to the superconductivity

On the April 8, 1911 [95], H. K. Onnes accidentally observed that the resistivity of mercury abruptly disappeared as the temperature of 4.19K [96]. Initially, H. K. Onnes named such phenomenon as “superconductivity” in order to highlight the extremely conducting nature of the state. The Nobel Prize in Physics in 1913 was awarded to him “for his investigations on the properties of matter at low temperature which led, inter alia, to the production of liquid helium” [97]. Since from that day, with more and more experiments have been done [96], the nature of superconductivity has been becoming more and more clear. The Meissner effect indicates the superconducting state is a thermal equilibrium state, and then phenomenological description on superconductivity has been by F. London and H. London, and V. L. Ginzburg and L. D. Landau. The discovery of isotope effect has proved that the electron phonon interaction is crucial for superconductivity [98][99], and then J. Bardeen, L. N. Cooper and J. R. Schrieffer have proposed that the electron pairing attracted by electron phonon interaction is the key for the superconductivity [100]. Then, the observation of Little-Parks effect has offered evidence of electron pairing in the superconductivity [101][102][103]. Besides those, the prediction of the Abrikosov lattice in type-II superconductors and the realization of the Josephson junction [104] also provide new knowledges on the superconductivity.

Nowadays, because of the zero resistance characteristic, the superconductivity is always the center topic in the research field of condensed matter physics, which is always expected new functionalities for future applications.

5-1-1 The zero resistance and the Meissner effect

The superconductivity is the phenomenon with two distinct properties, the zero resistance and the perfect diamagnetism.

Usually, for a normal metal, the resistance slowly decreases with the decreasing of the temperature, because the scattering effect is pressed in low temperature. On the other hand, there always exist some defect, disordered and impurity in the metal, thus there should be a residual resistance even at zero temperature. However, sometimes people have found that some materials exhibit a dramatic decrease of the resistance even down to zero, out of the measurement limits, when the temperature is below a critical temperature. The superconductor performs like a perfect conductor. This is one of the two key characteristics of the superconducting state. A schematic figure displays the superconducting transition in Figure 5-1 (1).

In addition to the zero resistance below the critical temperature, the expulsion of the external magnetic field, when the superconducting state has been established, is the other key characteristic the superconductivity, named after W. Meissner who has discovered such diamagnetism of the superconducting state. This phenomenon demonstrates that the superconductor is not only the perfect conductor, but also a unique thermal state with totally diamagnetism. A schematic phase diagram is shown in Figure 5-1 (2). When the temperature is below the critical temperature (T_c), with the increase of external magnetic field, the superconductor firstly stays in Meissner state with perfect diamagnetism, then some of the magnetic flux pierce into the superconductor establishing a mixed state, and finally the superconductivity is complete disappeared and the superconductor tuning into normal conductor. If the superconductor displays the phase diagram like Figure 5-1 (2), then it is called the type-II superconductor. On the other hand, some of the superconductor displays the phase diagram without the mixed state, then it is called the type-I superconductor. In general, most of superconductors behave like type-II superconductor. In addition, the piercing magnetic flux quantum is also called the vortex, and the magnetic flux piercing into the type-II superconductor is a quantized value as

$$\phi_0 = \frac{h}{2e} \approx 2.07 \times 10^{-15} T \cdot m^2 \quad (5.1)$$

where h is the Plank constant, and e is the electron charge. The constant 2 appearing in the denominator indicates the electron pairing nature of the superconductivity.

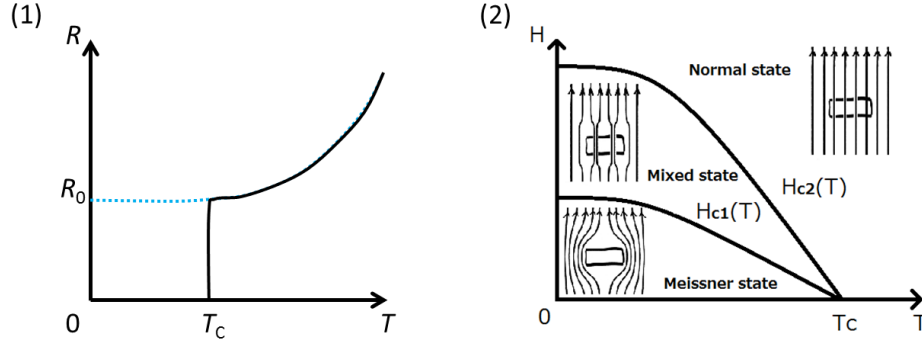


Figure 5-1: The schematic figures of superconducting transition and the phase diagram of type-II superconductor.

(1) The resistance (solid line) abruptly decreases down to almost zero without external magnetic field, indicating the superconducting transition, while the resistance (dashed line) does not show the decrease of resistance in the strong magnetic field. (2) The phase diagram is shown, exhibiting Meissner state, mixed state, and normal state, respectively.

5-1-2 The Bardeen-Cooper-Schrieffer theory of superconductivity

The Bardeen-Cooper-Schrieffer (BCS) theory, named after the authors, is the first microscopic theory of superconductivity in history [100]. Because this theory has been introduced in many textbooks, we will not introduce this theory carefully, but carry out some key information.

Roughly speaking, the BCS theory proposes a gapped ground state of superconductivity, originating the condensation of the Cooper pairs which are the two electrons on the Fermi level forming a pair attracted by electron phonon interaction within spin singlet state. Such superconducting gap at zero temperature $\Delta_{\text{BCS}}(T = 0)$ and the critical temperature T_c obey a universal rule:

$$\Delta_{\text{BCS}}(T = 0) = 1.764 k_B T_c \quad (5.2)$$

where k_B is the Boltzmann constant.

5-1-3 The upper critical field of superconductivity

There exists an upper critical field which is the magnetic field to completely suppress superconductivity in type-II superconductor. The superconducting state breaks due to the depairing effect induced by external magnetic field. There are two different depairing effects. One is the paramagnetic depairing which leads the famous Pauli limit of the upper critical field, and the other one is the orbital depairing effect which only happens in type II superconductors. These two depairing effects lead to upper critical field H_{c2} in the phase diagram of type-II superconductors as shown in Figure 5-1. And the really upper critical field is the smaller one within the orbital limit or the Pauli limit.

The Pauli limit is the upper critical field that breaks the spin-singlet Cooper pairs due to the Pauli paramagnetism in the presence of external magnetic field based on the weak coupling Bardeen–Cooper–Schrieffer (BCS) theory, which is also known as Chandrasechar-Clogston limit [105][106].

The paramagnetic depairing gives the so-called Pauli limit by the competition between the Zeeman energy and the condensation energy. When an external magnetic field is applied in the normal state, electrons are polarized into spin up and spin down parts due to the Zeeman effect, which gives a Pauli paramagnetism as shown in Figure 5-2. In contrast, in the superconducting state, the Cooper pair in spin singlet state is not a spin polarized state. Hence, in order to polarize condensed electrons, the pairs must be broken due to the external magnetic field. This depairing effect occurs when the Pauli paramagnetic energy equals to the superconducting gapped energy (5.2)

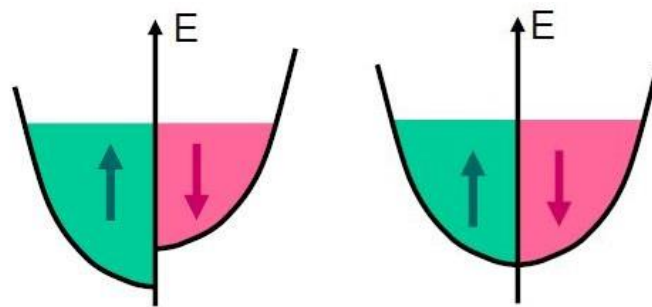


Figure 5-2: Conductors (left) and superconductors (right) in external magnetic field.

The horizontal axis is omitted, which is the density of state. In the superconducting state, the paramagnetic energy is higher than normal state, but it is the favored state because superconducting condensate energy.

Phenomenologically speaking, the upper critical field H_P can be estimated when the Pauli paramagnetic energy $E_P = 1/2 \chi_P H_P^2$ is equal to the superconducting condensation energy $E_C = 1/2 N(E_F) \Delta^2$, where $\chi_P = 1/2 (g \mu_B)^2 N(E_F)$ is the spin susceptibility in normal state, Δ is the superconducting gap at zero temperature, $N(E_F)$ is the density of state at the Fermi level E_F in the normal state, g is the spectroscopic splitting factor of electrons ($g = 2$ for free electrons), μ_B is the Bohr magneton. Thus the Pauli limit H_P is estimated to be $H_P = \sqrt{2} \Delta / g \mu_B$. According to the BCS theory, the superconducting gap Δ and superconducting critical temperature T_c obeys an universal value as $\Delta \approx 1.76 k_B T_c$, where k_B denote the Boltzmann constant. Hence, the Pauli limit at zero temperature is estimated to be

$$H_P^{\text{BCS}} \approx 1.84 T_c \quad (5.3)$$

On the other hand, in type-II superconductors, the mixed state mixes the superconducting Meissner state and the normal state in the macroscopic view, but in fact, these two states are still separated from each other in the microscopic view as shown in Figure 5-3 (1). In the mixed state, there are many vortex cores with a quantized magnetic flux ϕ_0 in the superconductor (Figure 5-3 (1)). The center of the core is in normal state and has a very low density of superconductive electrons (Figure 5-3 (2)), which is the reason why the magnetic field can through into the bulk.

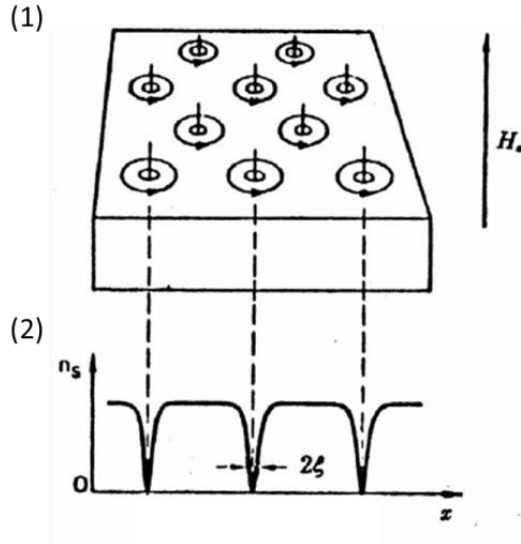


Figure 5-3: The schematic figure of vortex state in type-II superconductor.

(1) The vortex state in type-II superconductor. (2) The superconducting electrons density, the size of the vortex can be roughly estimated by coherence length.

From this point of view, it is easily to give an upper critical field by the overlap of vortex cores, which is nothing but the so-called orbital depairing effect. Hence, the size of the vortex is the most crucial value to be considered. The upper critical field limited by the orbital depairing effect can be roughly estimated by the following formula without losing any generality and neglecting not important constants:

$$H_{C2}(T) \approx \phi_0 / \xi(T)^2 \quad (5.4)$$

where the coherence length $\xi(T)$ with the temperature dependence obeys the relation as the below

$$\xi(T) \approx 1 / \sqrt{1 - T/T_c} \quad (5.5)$$

Combining with the above two equations, the temperature dependence of the upper critical field can be phenomenological described, for the case of the Ginzburg-Landau model and the Tinkham model, respectively.

5-1-4 The Ginzburg-Landau model

The Ginzburg-Landau model is the most well-known phenomenological model to describe the superconductivity in large and thick materials. In Figure 5-4, the schematic vortex is shown with anisotropic material in which the coherence lengths are different for different directions. For a simple discussion, we assume the anisotropy only exist along the c direction for a large and thick superconducting film. If the external magnetic field is applied along the c axis shown in Figure 5-4 (1), the size of the vortex is estimated as the product of two coherence length along a and b axis, respectively, with neglecting not important constant. The similar argument can be done for the external magnetic field applying along the a or b direction. Hence, the upper critical field for both case of the external magnetic field perpendicular (\perp) and parallel (\parallel) to the film plane are driven by

$$H_{C2}^{\perp}(T) \approx \frac{\phi_0}{\xi_{\parallel}(T)\xi_{\parallel}(T)} \propto \left(1 - \frac{T}{T_c}\right) \quad (5.6)$$

$$H_{C2}^{\parallel}(T) \approx \frac{\phi_0}{\xi_{\parallel}(T)\xi_{\perp}(T)} \propto \left(1 - \frac{T}{T_c}\right) \quad (5.7)$$

Thus, the anisotropic Ginzburg-Landau model describes the linear temperature dependence of the upper critical field for both two cases, as shown in Figure 5-4 (2).

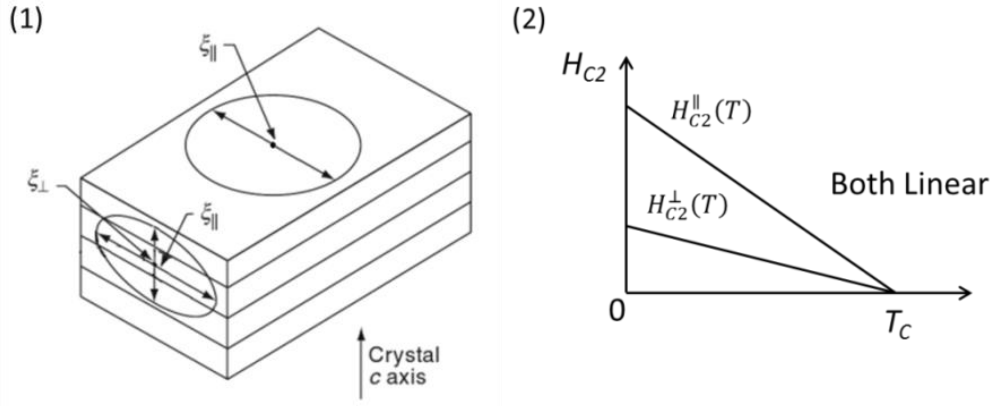


Figure 5-4: The schematic phenomenological description on the Ginzburg-Landau model.

(1) The schematic figure of vortex with anisotropic materials. (2) The schematic figure of the upper critical field obeying the Ginzburg-Landau model. The temperature dependence of upper critical field for both two cases of the external magnetic field perpendicular (\perp) and parallel (\parallel) to the film plane are linear.

Because the vortex is weakly affected by the geometric parameters of the material in the description by the Ginzburg-Landau model, the Ginzburg-Landau model is often considered as a three-dimensional model.

5-1-5 The Tinkham model

The Tinkham model is the phenomenological model well-known for describing the superconductivity in large but thin materials, in which the vortex is confined by the geometric parameter of the thickness of the material. In Figure 5-5, the schematic vortex is shown with thin material in which the coherence lengths are different for different directions. If the external magnetic field is applied along the c axis shown in Figure 5-5 (1), the size of the vortex is estimated as the product of two coherence length along a and b axis, respectively, the same as the size described by Ginzburg-Landau model. However, for the external magnetic field applying along in-plane direction, the size of the vortex should be estimated by the product of one in-planed coherence length and the thickness of the thin material, as shown in Figure 5-5 (1).

Hence, the upper critical field for two cases of the external magnetic field

perpendicular (\perp) and parallel (\parallel) to the film plane are respectively driven by

$$H_{C2}^{\perp}(T) \approx \frac{\phi_0}{\xi_{\parallel}(T)\xi_{\parallel}(T)} \propto \left(1 - \frac{T}{T_c}\right) \quad (5.8)$$

$$H_{C2}^{\parallel}(T) \approx \frac{\phi_0}{\xi_{\parallel}(T)d} \propto \sqrt{1 - \frac{T}{T_c}} \quad (5.9)$$

Thus, the Tinkham model describes the linear temperature dependence of the upper critical field for the perpendicular magnetic field but curved temperature dependence of the upper critical field for the parallel magnetic field, as shown in Figure 5-5 (2).

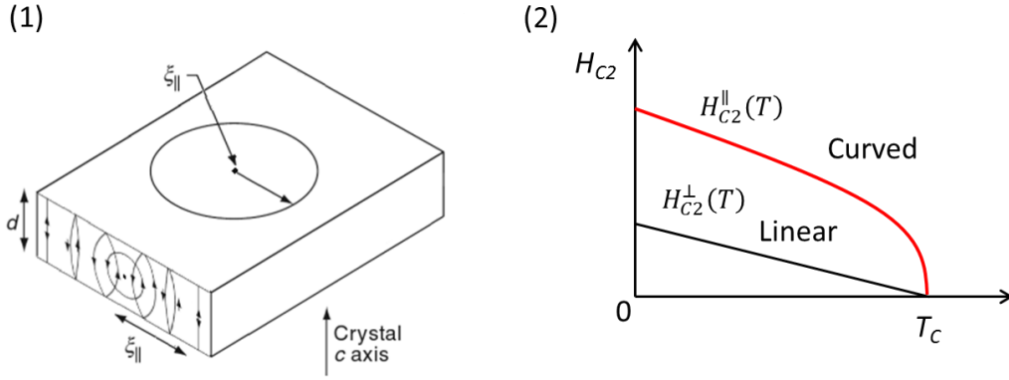


Figure 5-5: The schematic phenomenological description on the Tinkham model.

(1) The schematic figure of vortex with thin materials. (2) The schematic figure of the upper critical field obeying the Tinkham model. The temperature dependence of upper critical field for two cases of the external magnetic field perpendicular (\perp) and parallel (\parallel) to the film plane are linear and curved, respectively. The $H_{C2}^{\parallel}(T)$ described by the Tinkham model is shown in red line to be distinct to the $H_{C2}^{\parallel}(T)$ described by the Ginzburg-Landau model.

Compared with the Ginzburg-Landau model, the vortex is strongly affected by the geometric parameters of the thickness of the material in the description by the Tinkham model, thus the Tinkham model is often considered as a two-dimensional model.

5-1-6 Angular dependence of the upper critical field

In addition to the different descriptions on the upper critical field in the case of parallel magnetic field by Ginzburg-Landau model and Tinkham model, the angular dependences of the upper critical field of two models are also distinct. The direction of the external magnetic field is defined by Figure 5-6.

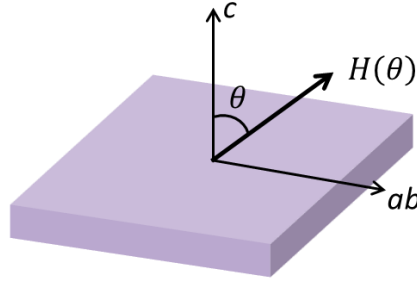


Figure 5-6: A schematic figure to represent the direction of external magnetic field.

For angular dependence of the upper critical field., ab denotes the in-plane direction and c denotes the out-plane direction, the angle θ is shown.

For the Ginzburg-Landau model, the angular dependence of the upper critical field follows the relation:

$$\left(\frac{H_{c2}(\theta, T)}{H_{c2}^{\parallel}(T)} \sin \theta \right)^2 + \left(\frac{H_{c2}(\theta, T)}{H_{c2}^{\perp}(T)} \cos \theta \right)^2 = 1 \quad (5.10)$$

While for the Tinkham model, the angular dependence of the upper critical field is expressed as the following:

$$\left(\frac{H_{c2}(\theta, T)}{H_{c2}^{\parallel}(T)} \sin \theta \right)^2 + \left| \frac{H_{c2}(\theta, T)}{H_{c2}^{\perp}(T)} \cos \theta \right| = 1 \quad (5.11)$$

In Figure 5-7, an experimental result of ionic liquid gating induced superconductivity in MoS₂ is introduced [57]. The Ginzburg-Landau model describes that the angular dependence of the upper critical field displays a relative broad peak at $\theta = \pi/2$. In contrast, the Tinkham model indicates that the angular dependence of the

upper critical field exhibits a kink at $\theta = \pi/2$. Hence, according to the experimental result, the superconductivity in MoS₂ has been clarified to be two dimensional.

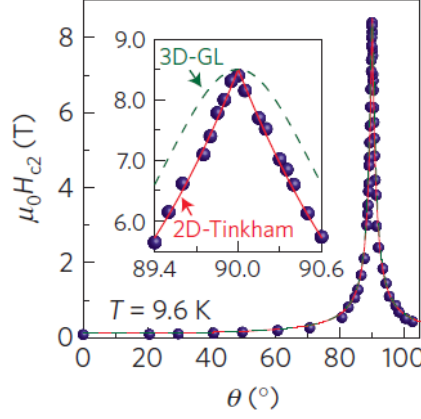


Figure 5-7: Two-dimensional superconductivity in ionic liquid gated MoS₂.

The angular dependence of the upper critical field is shown, and the inset displays a magnified view of the region around $\theta = \pi/2$. For the theoretical representation, the red solid line corresponds to the Tinkham model, and the green dashed line corresponds to the Ginzburg-Landau model.

5-2 Anisotropic superconductivity

Because the WS₂ NT has anisotropic geometry, the superconductivity in individual WS₂ NT itself is expected to display the anisotropy.

5-2-1 The superconducting transition

In Figure 5-8, the temperature variation of the resistance under the external magnetic field is displayed, both for the external magnetic field parallel and perpendicular to the NT axis, respectively. In the case of the external magnetic field parallel to the NT axis, the superconductivity is robust against the magnetic field and remains undefeated even under $H = 9\text{ T}$ at $T = 2\text{ K}$, while the superconducting phase rapidly disappears for the configuration with increase of the external magnetic field perpendicular to the NT axis.

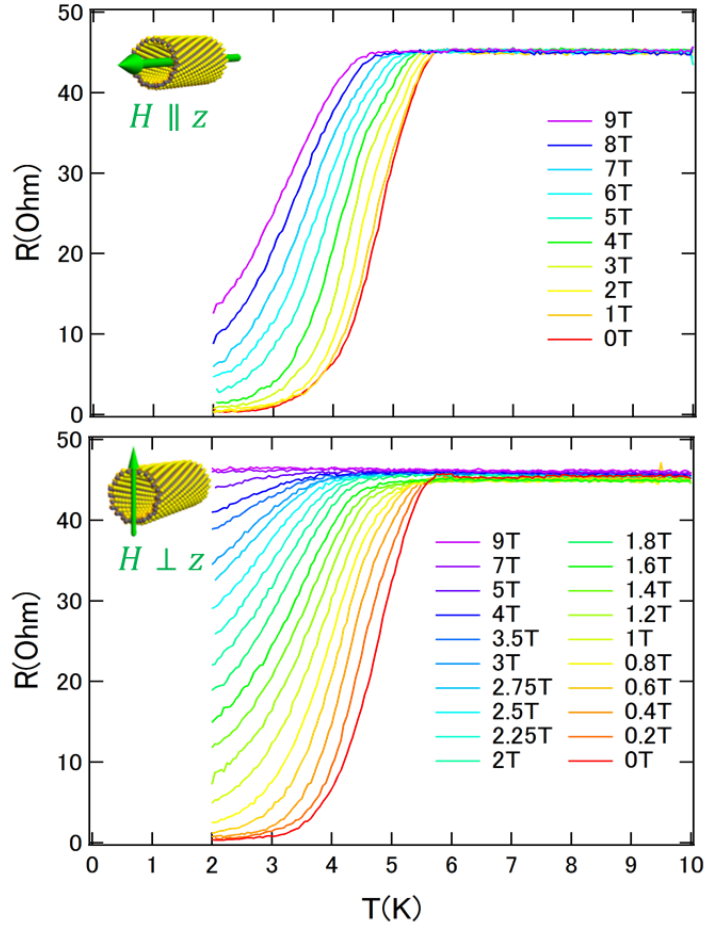


Figure 5-8: The superconducting transition under the external magnetic field.

The temperature variation of the resistance under the external magnetic field is displayed, both for the external magnetic field parallel (top) and perpendicular (bottom) to the NT axis, respectively.

5-2-2 The magnetoresistance during superconducting transition

In Figure 5-9, the magnetoresistance of variation of the temperature is displayed, both for the external magnetic field parallel and perpendicular to the NT axis, respectively. In the case of the external magnetic field parallel to the NT axis, the superconductivity is robust against the magnetic field and remains undefeated even under $H = 9\text{ T}$ at $T = 2\text{ K}$, while the superconducting phase rapidly disappears for the configuration with increase of the external magnetic field perpendicular to the NT axis.

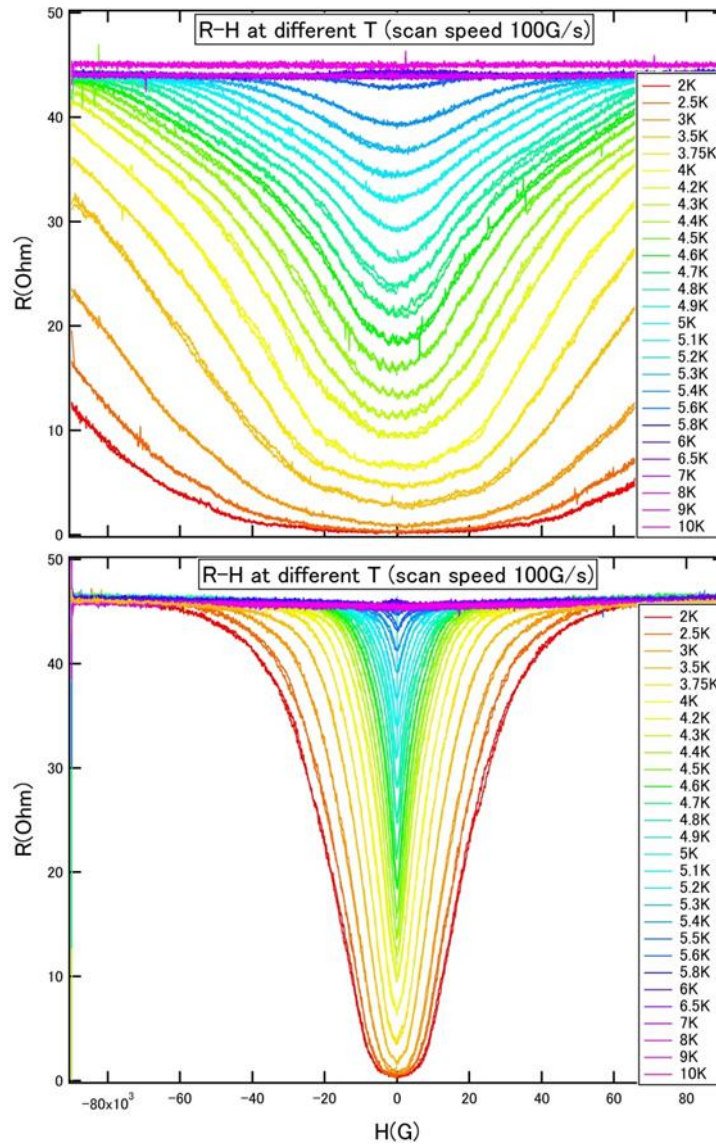


Figure 5-9: The magnetoresistance during superconducting transition.

The magnetoresistance of variation of the temperature is displayed, both for the external magnetic field parallel (top) and perpendicular (bottom) to the NT axis, respectively, in the same sample shown in Figure 5-8.

5-3 Intermediate state

It should be noted that, for the case of for the external magnetic field parallel to the NT axis, within low field region, the magnetoresistance shows periodic oscillations, which will be further discussed in the next Chapter 6.

For the external magnetic field perpendicular to the NT axis, a possible

one-dimensional superconducting transport under magnetic field is demonstrated [107]. As shown in Figure 5-10, the magnetoresistance of another sample of variation of the temperature is displayed for the external magnetic field perpendicular to the NT axis. It is clear to see that the superconducting WS_2 NT tunes into the intermediate state, the part nearly perpendicular to the external magnetic field becomes not superconducting, while the part nearly parallel to the external magnetic field remains superconducting.

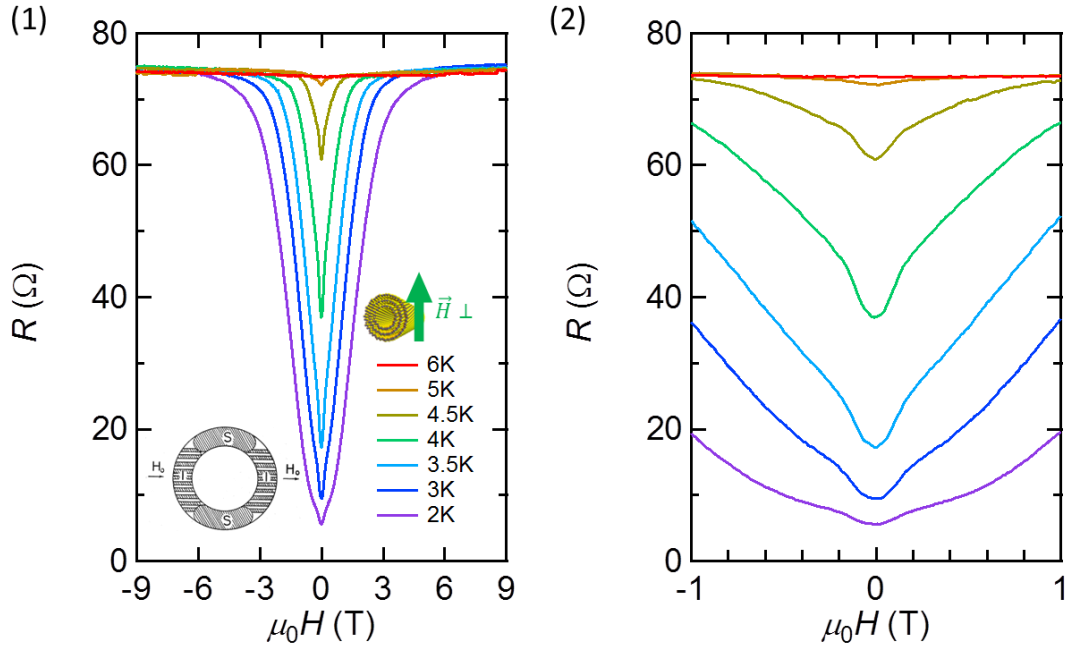


Figure 5-10: The magnetoresistance during superconducting transition.

The magnetoresistance (left) and the magnified magnetoresistance in low field region (right) are displayed, and the inset is a schematic figure of intermediate state in hollow superconducting cylinder [107].

5-4 Upper critical field and Pauli limit

In this section, we argue on the enhancement of the upper critical field over the Pauli limit in superconducting WS_2 NT. As shown in Figure 5-11, the phase diagram of the upper critical field H_{c2} is displayed, for both case of magnetic field applied parallel and perpendicularly to the axis of superconducting WS_2 NT, consistent with previous discussion of anisotropic superconductivity. Especially, the upper critical field is clearly over the Pauli limit.

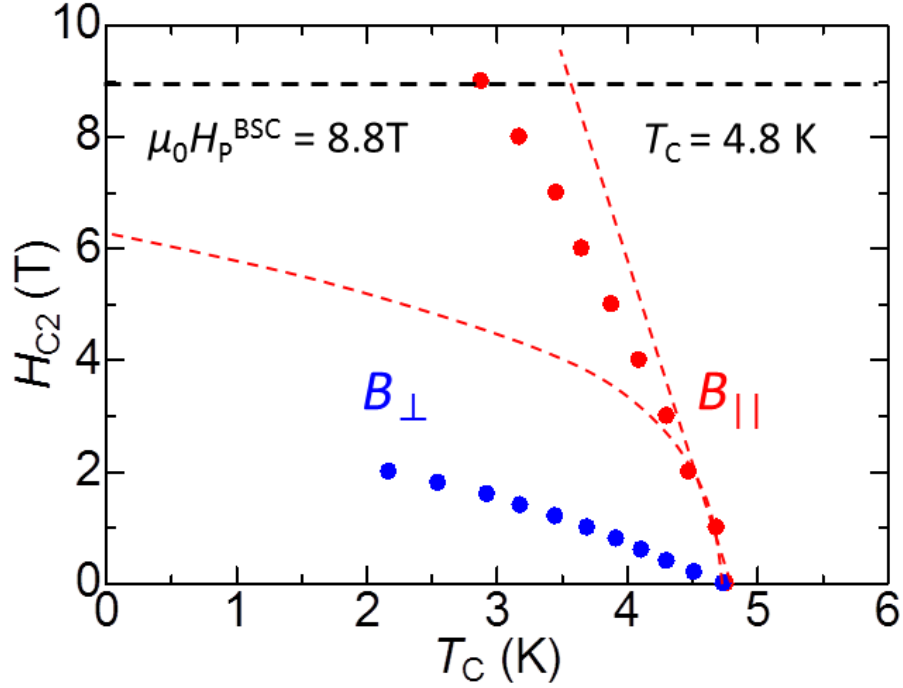


Figure 5-11: Phase diagram of upper critical field in parallel and perpendicular magnetic field.

For the case of magnetic field applied parallel to the axis of WS₂ NT, the upper critical field is expected to be exceeding the Pauli limit. And the curved and linear dashed line are the fitting by 2D Tinkham and 3D anisotropic Landau theory. The observed data in between the 2D and 3D case, displaying an intermediate dimensionality.

For superconducting WS₂ NTs, however, the observed upper critical field in the $H \parallel z$ configuration exceeds the Pauli paramagnetic limit discussed above, indicating the potential mechanism listed below which can explain the enhancement of the upper critical field.

In a superconductor with spin-orbit interaction, the enhancement of Pauli limit has been often discussed by spin-orbit scattering and spin-momentum (or spin-valley) locking.

Enhanced Pauli limit of the two-dimensional (2D) superconductivity in transition metal dichalcogenides (TMDs) has been discussed very recently in terms of the Ising pairing protected by out-of-plane Zeeman-type spin-valley locking[57][58][62]. Since the multi-walled NT can be seen as the stacking of inequivalent curved 2D monolayers, the similar mechanism should be considered for the enhancement of Pauli limit in

superconducting WS_2 NTs. We note that three-dimensional nature induced by the electrochemical doping cannot be also negligible, which can explain the smaller upper critical field in this system than pure 2D cases.

In a dirty-limit superconductor, on the other hand, spin-orbit scattering mechanism is dominated [108], in which the spin paramagnetism is suppressed due to the random spin orientation by scattering, resulting in the decrease of Pauli spin split energy. Since the disorder is potentially caused during the intercalation process, the spin-orbit scattering effect may also contribute to the enhanced Pauli limit in superconducting WS_2 NTs.

In addition, the effect of the nontrivial Cooper pairing has been also discussed in the noncentrosymmetric and low dimensional superconductors.

In a noncentrosymmetric superconductor, the symmetry allows the mixing of the spin singlet pairing and spin triplet pairing. Since the triplet pairing is robust against the external magnetic field, the mixing of spin singlet and spin triplet pairing cause the enhancement of the upper critical field, which should be taken into account in superconductivity of chiral WS_2 NTs.

Another effect of the nontrivial pairing under magnetic field is known as the Fulde-Ferrell-Larkin-Ovchinnikov (FFLO) state [109][110][111]. In FFLO state, Cooper pairs have non-zero momentum, which cause the reduction of the Pauli spin split energy and resultant enhancement of the upper critical field. For one dimensional (1D) case, upper critical field even infinitely diverges at zero temperature [111]. Because of the superconductivity has been observed in low dimensional NT structure, such FFLO state may plays an important role for the enhancement of Pauli limit.

The detailed mechanism of the superconductivity and resultant Cooper pairing in a chiral WS_2 NT should be further pursued in the future.

Chapter 6

Little-Parks oscillation

6-1 Introduction

In history, the Little-Parks effect was experimentally discovered in 1962 by W. A. Little and R. D. Parks when they measured empty and thin-walled superconducting tin cylinders under the magnetic field parallel to the axis [101]. As shown in Figure 6-1, the observed longitude magnetoresistance has displayed periodic oscillation around superconducting transition temperature. Here, the meaning of thin-wall is the thickness of the wall is smaller than the magnetic penetration length.

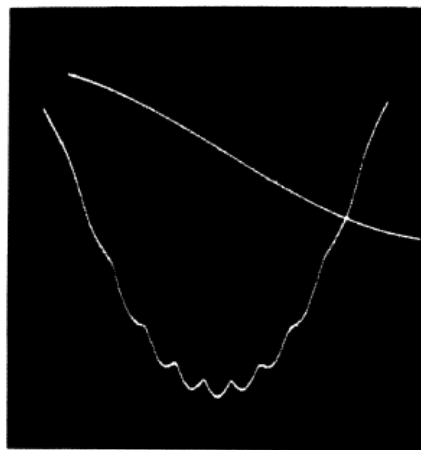


FIG. 2. Lower trace: variation of resistance of tin cylinder at its superconducting transition temperature as a function of magnetic field. Upper trace: magnetic field sweep.

Figure 6-1: The historic figure of the observation of Little-Parks effect.

When scanning the external magnetic field, the longitude resistance oscillates periodically, which reflects more fundamental physics behind Little-Parks effect.

It should be noted that such Little-Parks oscillation is distinct from the well-known Aharonov-Bohm (AB) oscillation [112][113] or the high order AB oscillation as Altshuler-Aronov-Spivak (AAS) oscillation [67]. The period of the oscillation is one half of the period of AB oscillation, obeying the relation (6.1)

$$\phi_0 = \frac{h}{2e} \approx 2.07 \times 10^{-15} T \cdot m^2 \quad (6.1)$$

where h is the Plank constant, and e is the electron charge.

The Little-Parks oscillation reflects more fundamental physics than AB oscillation. The Little-Parks oscillation is the result of collective quantum behavior of superconducting electrons interference by the external magnetic field, and the constant 2 appearing in the denominator of (6.1) indicates the electron pairing nature of the superconductivity [100]. Such resistance oscillation around critical temperature originates from the oscillation of the superconducting critical temperature of the superconducting cylinder [103]. Theoretically, the oscillation of the critical temperature is obtained by (6.2), but experimentally, it can be measured by (6.3).

$$\Delta T_c = 0.14 T_c \left(\frac{\xi}{r} \right)^2 \quad (6.2)$$

$$\Delta T_c = \Delta R \left(\frac{dR}{dT} \right)^{-1} \quad (6.3)$$

Combining with above two relations, the coherence length can be estimated.

6-2 Magnetoresistance oscillation during superconducting transition

In Figure 6-2, the magneto resistance at various temperatures around the critical temperature in parallel external magnetic field is shown. In addition to the robustness of the superconductivity discussed in Chapter 5, the magnetoresistance observed *via* the first harmonic signals in AC resistance (R^ω) shows periodically oscillating behavior in the low magnetic field region. The magnified magnetoresistance shown in Figure 5-9 in the low field region is shown in Figure 6-2 (1), and the magnetoresistance of another sample shows more clear oscillating behavior in Figure 6-2 (2). By subtracting the

polynomial background from Figure 6-2, the oscillation of two samples are shown in Figure 6-3.

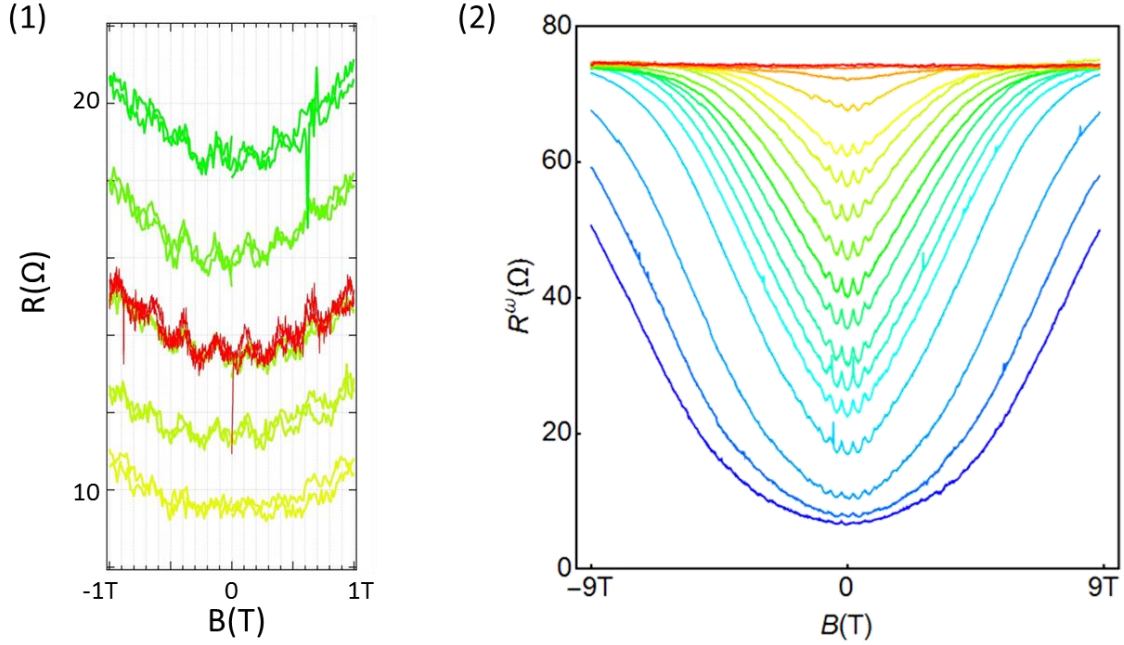


Figure 6-2: Magnetoconductance oscillation during superconducting transition.

(1) The magnified magnetoconductance in low field region shown in Figure 5-9. (2) Magnetoconductance oscillation during superconducting transition in another sample, which displays a much clear oscillating behavior in the low field region.

The period of the oscillation in Figure 6-2 (1) is about 0.25 T, corresponding to the diameter of 100 nm, consisting with the measured value of 120 nm by AFM. The amplitude of the oscillation is estimated as $\Delta R = 0.8 \Omega$, and then resulting in the oscillation of critical temperature about $\Delta T_c = 32$ mK, experimentally. Hence, by combining (6.2) and (6.3) the coherence length can be estimated about $\xi = 10.9$ nm

On the other hand, the period of the oscillation in Figure 6-2 (2) is about 0.4 T, corresponding to the diameter of 80nm. The amplitude of the oscillation is estimated as $\Delta R = 3 \Omega$, and then resulting in the oscillation of critical temperature about $\Delta T_c = 56$ mK, experimentally. Hence, by combining (6.2) and (6.3) the coherence length can be estimated about $\xi = 12.2$ nm

There results of diameters are consistent with the diameter distribution histogram

of the same batch shown in Chapter 3.

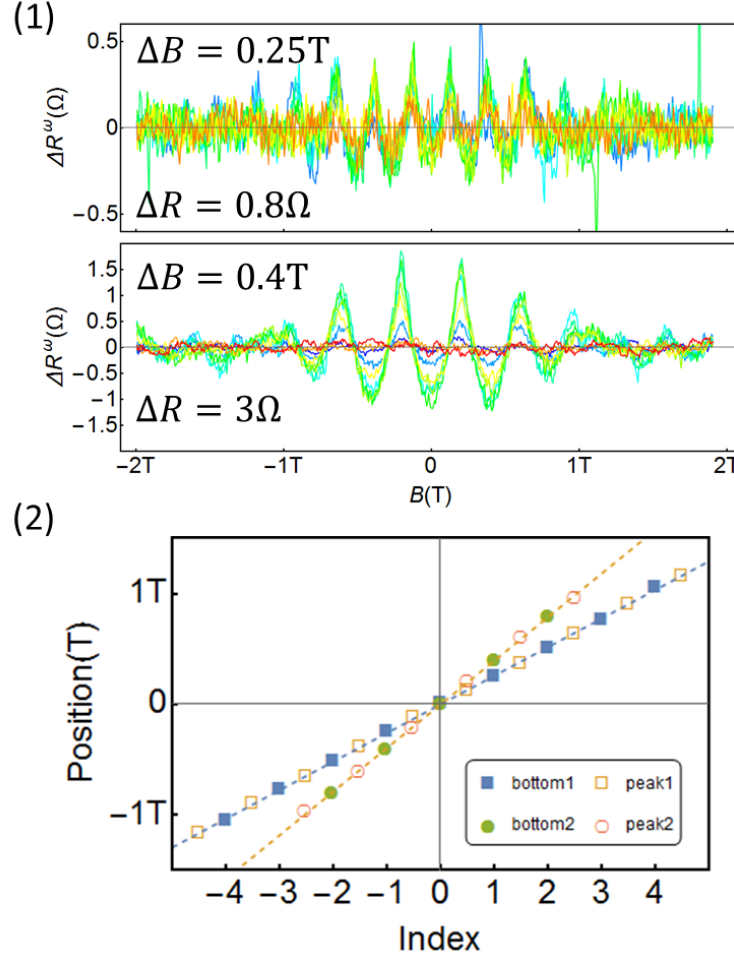


Figure 6-3: The magnetoresistance oscillation of two samples.

(1) The magnetoresistance subtracted by the polynomial background, the period quadric oscillating behavior is clear to be seen. (2) Index plot for the maximum and minimum peak positions of the Little-Parks oscillation. The square marks correspond to the sample in (1) top, and circle marks correspond to the sample in (1) bottom.

6-3 Magnetic flux quantization inside superconducting cylinder

The magnetic flux is quantized as the integer number of magnetic flux quantum, as shown in Figure 6-4. [114]

The reason of the quantization of inside magnetic flux is because the magnetic field inside cylinder is the total field of external magnetic field and the self-field

generated by diamagnetic current. The diamagnetic current is periodically changed with the external magnetic field, which is due to the minimization of free energy of the superconducting cylinder.

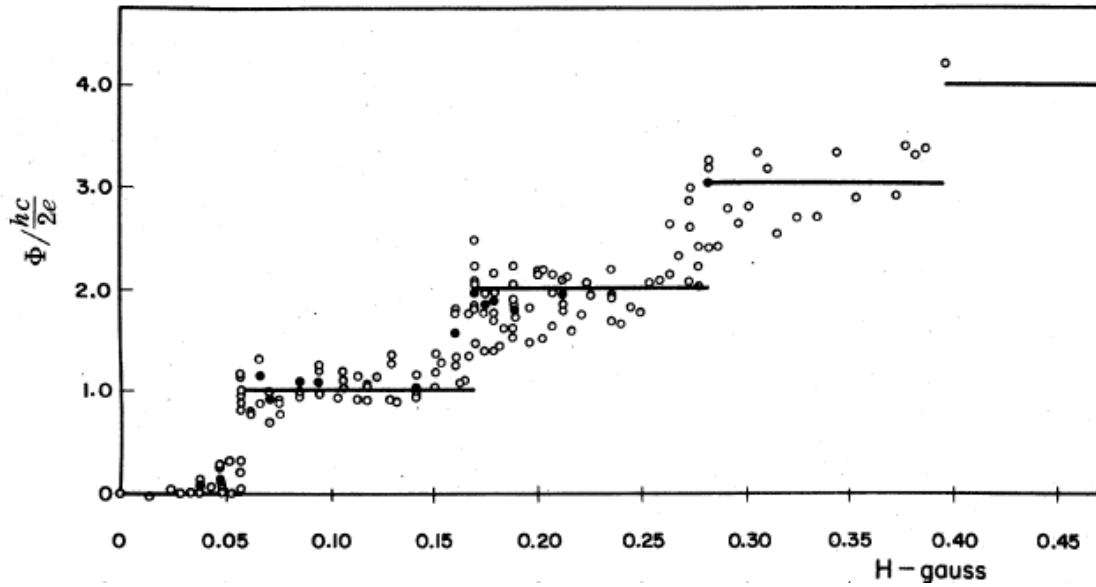


Figure 6-4: Magnetic flux quantization inside superconducting cylinder.

The magnetic flux inside the cylinder corresponding to measured magnetic field is shown against with external magnetic field.

Phenomenologically, the total free energy content two parts, one is the kinetic energy of supercurrent, and the other one is the potential energy in the external magnetic field. Among them, the potential energy is parabolic dependent on the external magnetic field as shown in Figure 6-5 (3). The kinetic part is the kinetic energy of supercurrent, since the supercurrent flows along circumference and thus linearly dependent on the external magnetic field as shown in Figure 6-5 (4), the supercurrent also shows periodic behavior in order to minimize the kinetic energy by magnetic flux quantum piercing inside the cylinder, and thus resulting in the periodic quadric change of kinetic energy.

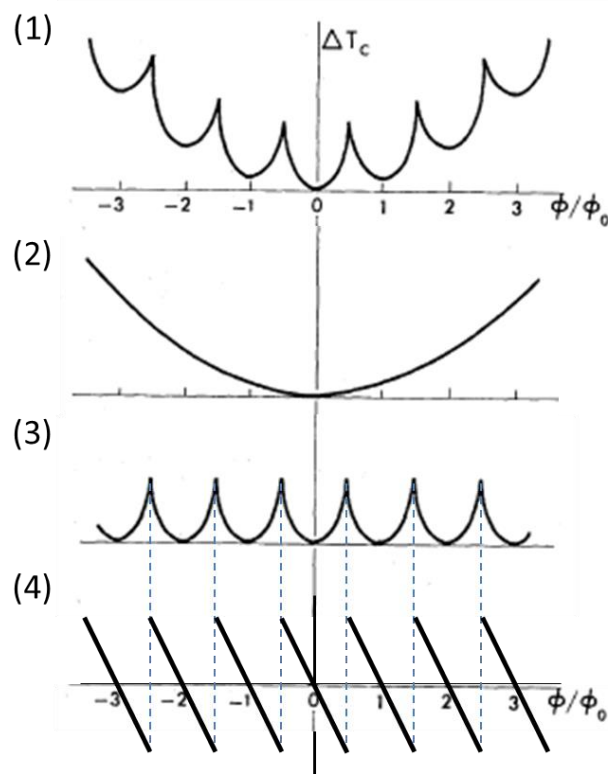


Figure 6-5: The schematic figure of the results of Little-Parks experiments.

(1) The schematic figure of the results of Little-Parks experiments on the variation of T_C with flux through a thin-wall cylinder. (2)(3) The variation of T_C decomposed into periodic part (2) and parabolic part (3). (4) The schematic figure of supercurrent flow, resulting in the periodic part of kinetic energy in (3).

Hence, the observed Little-Parks effect, which is the periodic oscillation of magnetoresistance of the superconducting cylinder under external magnetic field, originates from the collective motion of superconducting electrons, and thus results in the magnetic flux quantization inside the cylinder.

Chapter 7

Diameter-dependent critical temperature T_c

7-1 Diameter of NTs

The properties of superconductivity in the WS₂ NTs with different diameters have been further investigated. Figure 7-1 shows the normalized Little-Parks oscillations of WS₂ NT samples under magnetic field parallel to the axis of the NT. The oscillating component is extracted by subtracting the quadric background from the measured magnetoresistance. The polynomial background is expressed as $R_{BG} = a + b B^2 + c B^4$, in which the parameters are determined by least squares method to fit the data. In Figure 7-1, the positions of the maximum and minimum as a function of index number are plotted. Here, the linear relationship reflects the periodic nature of the Little-Parks oscillation. From the oscillations period, the effective diameter of each the WS₂ NT was estimated by the equation shown below:

$$\mu_0 \Delta H \cdot \frac{\pi}{4} D^2 = \phi_0 \quad (7-1)$$

where D is the diameter of the WS₂ NT and $\mu_0 \Delta H$ is the period of Little-Parks oscillations observed in the magnetoresistance of WS₂ NT when magnetic field applied parallel to the NT axis.

According to the periods of Little-Parks oscillations, the diameter of each WS₂ NT are estimated as 107.8 ± 0.4 nm (sample 1, red), 100.8 ± 0.3 nm (sample 2, orange), 85.2 ± 0.5 nm (sample 3, green), and 70.3 ± 0.3 nm (sample 4, blue), respectively

Figure 7-2 shows the AFM images of the four measured samples after the experiments (intercalation and transport measurement). In Table 7-1: The NT diameters measured by AFM and by Little-Parks oscillations., the NT diameters are measured by AFM, and thus obtained nanotube diameters are compared with those derived from the period of Little-Parks oscillations. Both diameters agree fairly well with each other. However, we should note that the values of the diameter obtained from the AFM measurement varies along nanotube axis, the standard deviations along the single nanotube can be as large as the order of 10 nm. In addition, the AFM only measures the outer diameter of NT. Slight difference between values estimated from Little-Parks oscillations and that from AFM may be attributed to these reasons.

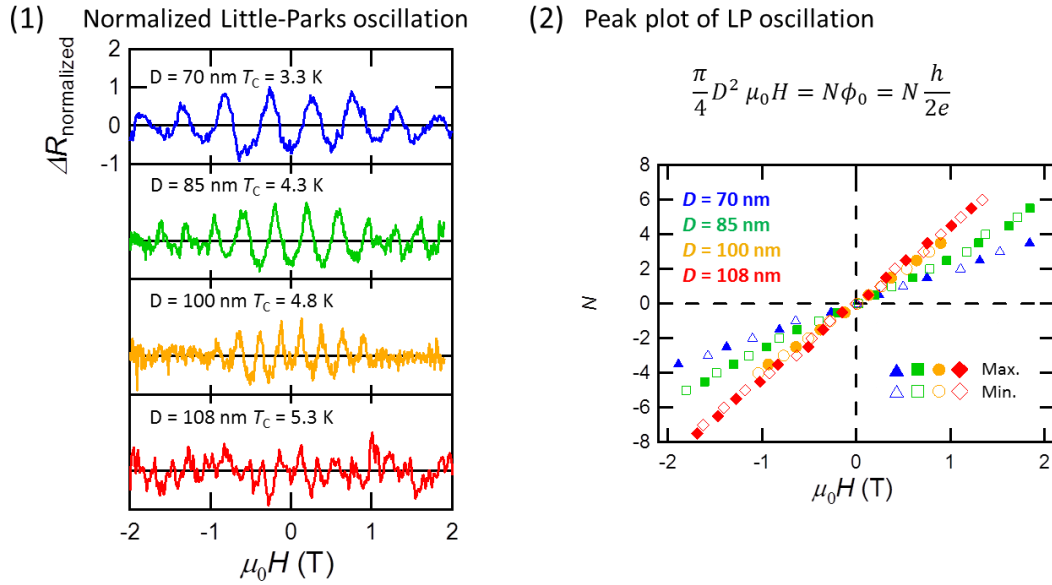


Figure 7-1: Normalized Little-Parks oscillation and peak plot.

(1) The normalized Little-Parks oscillations of four different WS₂ NT samples. (2) The peak plot of the magnetic field at each maximum and minimum versus index N .

	Sample 1	Sample 2	Sample 3	Sample 4
	$T_c = 5.3$ K	$T_c = 4.8$ K	$T_c = 4.3$ K	$T_c = 3.3$ K
D by Little-Parks oscillation	107.8 nm	100.8 nm	85.2 nm	70.3 nm
D by AFM	110.5 nm	101.2 nm	85.5 nm	71.1 nm

Table 7-1: The NT diameters measured by AFM and by Little-Parks oscillations.

The comparison of the values of the diameters obtained from the AFM measurement and from the transport measurement by the period of Little-Parks oscillations.

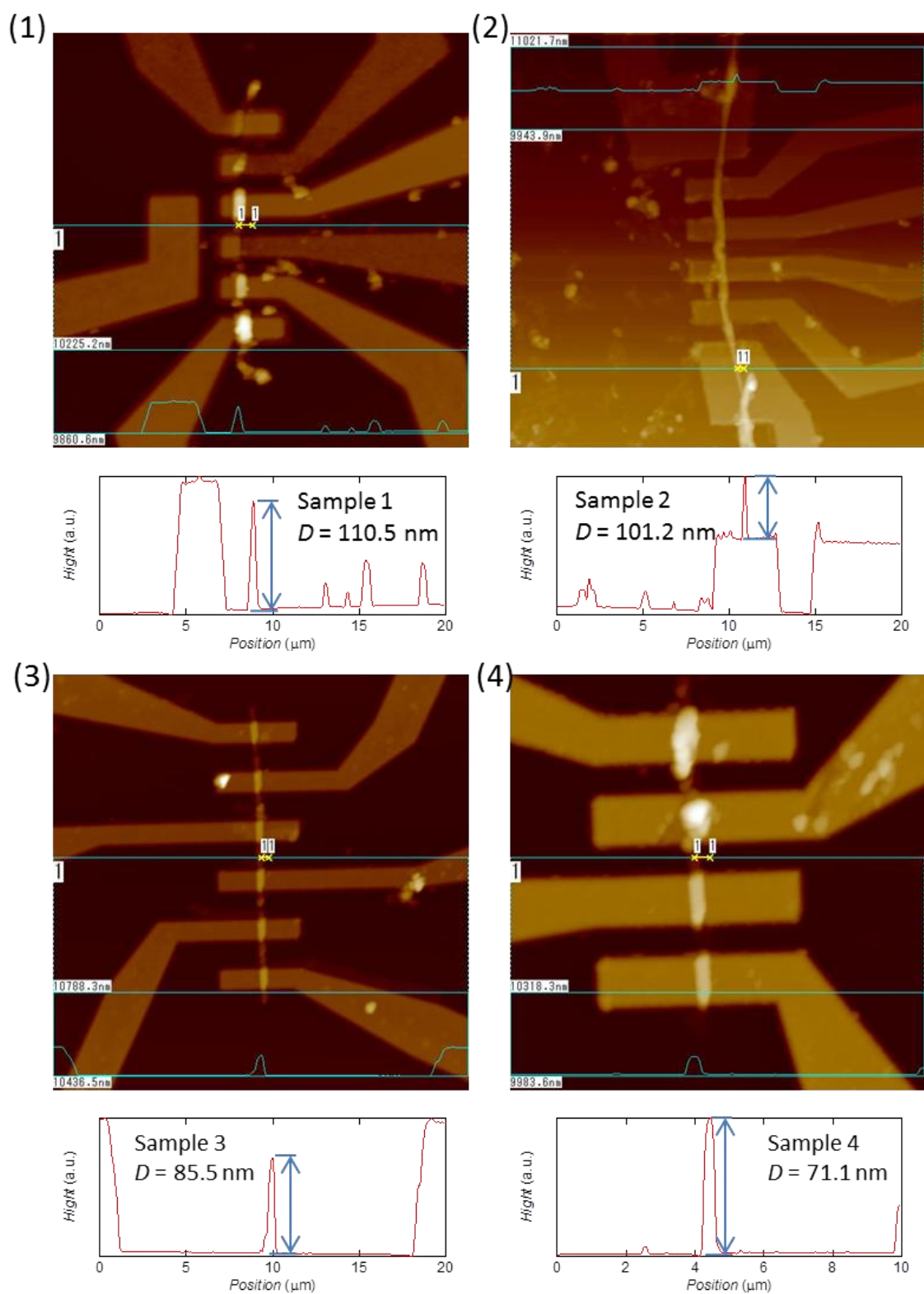


Figure 7-2: AFM images of four NT samples measured after transport experiments.
 (1)(2)(3)(4) The AFM image of sample 1, sample 2, sample 3, and sample 4, respectively.

7-2 Critical temperature

Figure 7-3 shows the temperature dependence of the normalized resistance for different WS₂ samples. Sample 1 to 4 represent WS₂ NTs with different diameter, and sample 0 (black) corresponds to the WS₂ flake as comparison (data adapted from ref. [60]), respectively. The superconducting transition is sharp in the WS₂ flake while it is broadened in the WS₂ NT, which is probably related to the phase slip phenomenon in quasi-1D system due to both thermal and quantum fluctuations [115][116].

Judging from the half resistance the critical temperature, T_c of the different WS₂ samples are estimated as $T_c = 8.3$ K (sample 0), 5.3 K (sample 1), 4.8 K (sample 2), 4.3 K (sample 3), and 3.3 K (sample 4), respectively. Assuming that the diameter of WS₂ flake sample is infinite (i.e., curvature is zero for the case of flake), the relation between the critical temperature T_c and inverse diameter D^{-1} (curvature of the sample) is finally plotted in Figure 7-3.

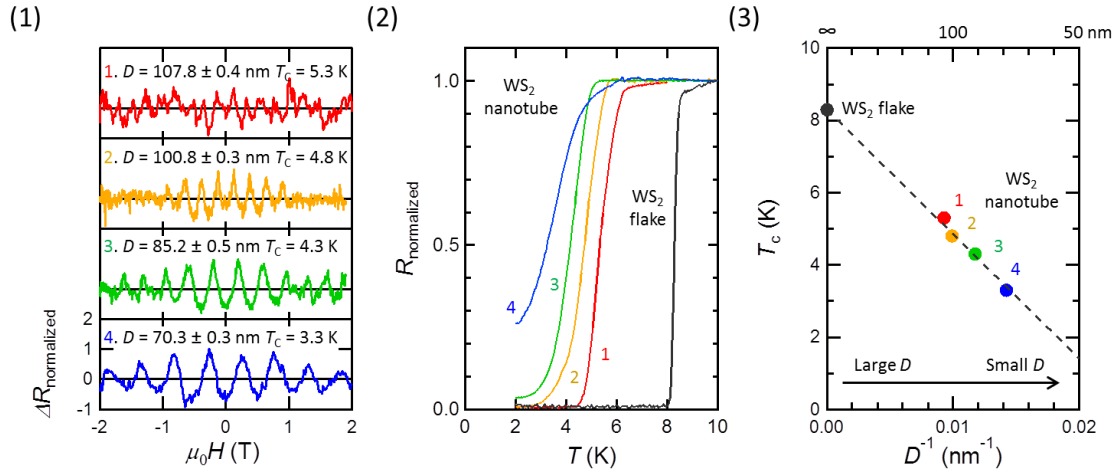


Figure 7-3: Diameter dependence of superconductivity.

In this figure, identical color represents identical sample. (1) Little-Parks oscillations of different WS₂ NT samples. (2) The temperature dependence of the resistance for different WS₂ NT samples with different diameters. The data are normalized by the resistance at 10 K. (3) The critical temperature as a function of inverse effective diameter of the NTs. The critical temperature of each NT is defined by half-resistance from (2) and the diameter of each NT is estimated by the oscillating period from (1) by the relation of $\mu_0 \Delta H \cdot \frac{\pi}{4} D^2 = \phi_0$, where $\mu_0 \Delta H$ is the period of Little-Parks oscillation, D is the diameter of NT, and ϕ_0 is the magnetic flux quantum.

It is clearly shown that T_c systematically decreases with inverse diameter D^{-1} . To a first order approximation, T_c is well fitted by a linear function of the inverse of the diameter. Since the T_c of superconductivity in K intercalated WS_2 flake is constant against the amount of intercalated K [60], it is the case that the superconducting K_xWS_2 is a line phase compound with a fixed value of x , rather than a solid solution, where x and thus T_c are tunable. Such staging behavior is well known in many layered materials including graphite intercalation compounds [94]. Thus, the systematic variation of the critical temperature discussed above is considered to originate purely from the difference in the sample geometry, such as diameter or wall thickness of the NT.

We note that observed systematic T_c variation cannot be explained by the simple size effect of quantum confinement by decreasing the NT diameter [117][118], because the NT diameter (nearly 100 nm) is one order of magnitude larger than the typical length scale of quantum confinement effect (below 10 nm). However, the quantum confinement effect can originate from wall thickness of the NT [119], and it is known that the thickness of sample can affect the superconductivity through various mechanisms [120][121][122]. Therefore, we need to separate the wall thickness dependent effect from the diameter-dependent effect (Figure 7-3). Because the diameter of NT is effectively large, we can treat our sample as curved 2D film, and the dimensionality or the effective thickness of superconducting NT can be estimated by measuring the temperature dependence of the upper critical field in the same manner as in flakes [123] (See the next section 7-3, we clarified through a Ginzburg-Landau calculation that dimensional crossover in the cylindrical superconductor is not affected by radius but essentially driven by the change in thickness of the wall.)

Figure 7-4 shows the upper critical field of all samples in the both parallel and perpendicular magnetic field as a function of the temperature. When the magnetic field is applied perpendicular to the NT axis, the intermediate state is formed and results in the enhancement of the upper critical field arising from the case of WS_2 flake under perpendicular magnetic field, due to the tubular structure and the remaining superconducting edge (locally parallel to magnetic field), as discussed in section 5-3. On the other hand, for the case of magnetic field applied parallel to NT axis, the upper critical field can be well-fitted by the power law relation

$$H_{c2}(T) = H_{c2}(0) \left(1 - \frac{T}{T_c}\right)^\alpha \quad (7.2)$$

where α is the power index reflecting the dimensionality of the superconductivity ($1/2 < \alpha < 1$). According to the Ginzburg-Landau theory, $\alpha = 1$ indicates that the Landau level is not affected by the sample thickness and superconductivity can be treated as 3D-like, while $\alpha = 1/2$ corresponds to the 2D-like superconductivity in which Landau level is strongly modified by the sample thickness.

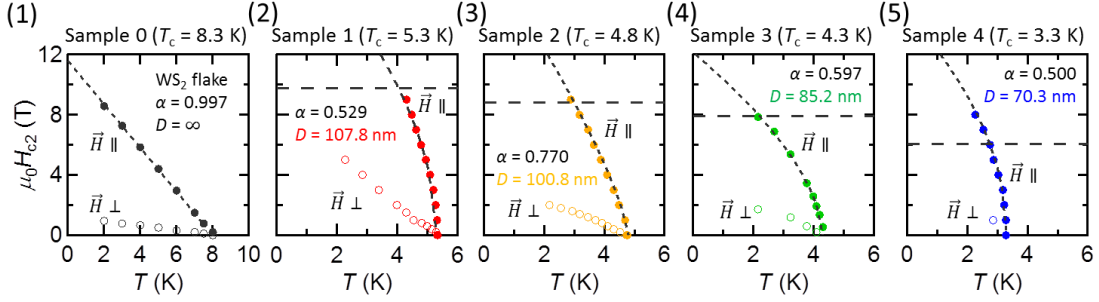


Figure 7-4: Upper critical field and dimensionality of each NT sample.

(1) The temperature dependence of the upper critical field for WS₂ flake sample. (2)(3) The temperature dependence of the upper critical field for two NTs with similar diameter, same figure as Figure 7-5. (4)(5) The temperature dependence of the upper critical field other NTs. In all figures, the horizontal dashed line corresponds to the Pauli limit based on BSC theory.

As seen in Figure 7-5 (1) and (2), although the diameter and T_c of the two samples are similar, the temperature dependence of the upper critical field displays a striking difference. Figure 7-5 summarizes the power index α for all samples, estimated from the fitting curve by (7.2). This figure clearly displays that there is no systematic relation between α and the diameter of the NT. Since α is an indicator of the wall thickness, these results imply that the wall thickness of the NT (dimensionality of the superconductivity) does not affect T_c in our samples and thus the T_c variation mentioned in Figure 7-3 is predominantly determined by the diameter (or curvature, which might lead to some strain effects) due to the tubular structure.

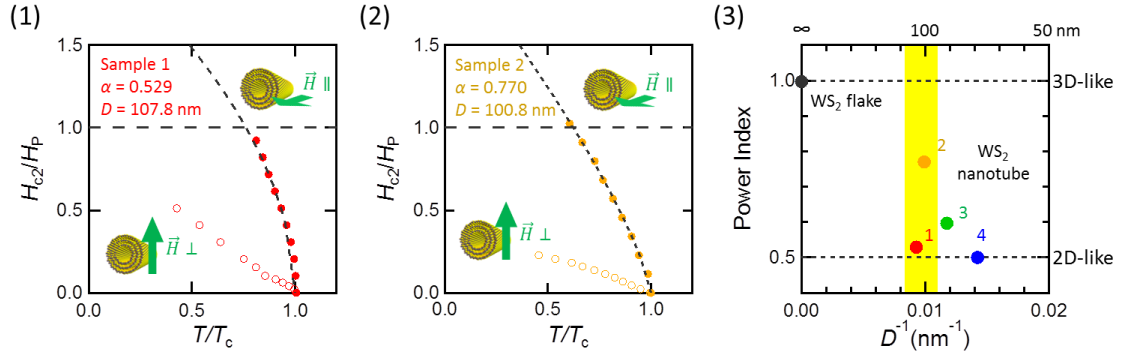


Figure 7-5: Upper critical field and dimensionality of superconductivity.

(1) (2) The temperature dependence of the upper critical field for two NTs with similar diameter of nearly 100 nm. Two samples display the similar superconducting transition temperatures and Little-Parks oscillation periods but distinct power index behavior. (3) The plot of the power index depending on the inverse diameter. The two plots in the yellow-hatched arear correspond to the samples shown in (1) and (1). The power index is very much different between the two samples, despite the similar diameters. It seems that there is no systematic relation between the power index and the diameter of NT, and thus, there is no systematic relation between the thickness of the wall and the diameter of NT. This leads us to conclude that T_c is determined solely by the diameter.

The effect of curvature on the critical temperature of carbon NTs was discussed before [124][125]. It was proposed that the curvature of the lattice will lead to enhancement of the critical temperature due to enhancement of the electron phonon coupling because new electron phonon scattering channels open due to the deformation of the carbon NT lattice. On the other hand, the present result of superconductivity in individual WS₂ NTs infers an opposite conclusion. Microscopically, the complex lattice distortions and the resultant unconventional electron phonon interaction may play an essential role, affecting the paring mechanism i.e. the superconducting properties of TMD NTs.

7-3 Dimensionality of superconductivity

We generalize the anisotropic Ginzburg-Landau equation [126] to satisfy the cylindrical symmetry of the NT by phenomenologically introducing the effective mass tensor in cylindrical coordinate. In order to obtain the relation between temperature and upper critical field (i.e. the dimensionality, as defined in the main text) when magnetic field is applied parallel to the axis of NT, the linearized Ginzburg-Landau equation to be

numerically solved is expressed as below, with Neumann boundary condition $\vec{n} \cdot \vec{p}\varphi = 0$, which ensures that no superconducting current flows out of the superconductor.

$$\frac{1}{2}\vec{p} \cdot \frac{1}{M} \cdot \vec{p}\varphi + \alpha\varphi = 0 \quad (7.3)$$

where $\vec{p} = -i\hbar\vec{\nabla} - 2e\vec{A}$ is the canonical momentum operator, $\vec{A} = 1/2\mu_0 H r \vec{e}_\theta$ is the vector potential of magnetic field \vec{H} satisfying $\vec{\nabla} \times \vec{A} = \mu_0 \vec{H} = \mu_0 H \vec{e}_z$ if the penetration depth is much larger than the sample size (type-II superconductor), and

$$\frac{1}{M} = \frac{\vec{e}_r \vec{e}_r}{m_r} + \frac{\vec{e}_\theta \vec{e}_\theta}{m_\theta} + \frac{\vec{e}_z \vec{e}_z}{m_z} \quad (7.4)$$

is the inverse of effective mass tensor expressed in cylindrical coordinate, and φ is the order parameter which is the pseudo wave function related to the density of superconducting component and only nonzero below the transition temperature T_c .

Equation (7.3) equivalently describes a particle with charge $2e$ in an external magnetic field, so that the eigenvalue α is determined by the lowest Landau level modified by geometric boundary condition, which determines the relation between temperature and upper critical field or the dimensionality. Because along the circumferential direction, the naturally periodic boundary condition is applied, the only confinement to the Landau level originates from the radial direction, namely the wall thickness of NT.

From this view point, the NT is identical to the rolled thin film, and the dimensionality of anisotropic NT is equivalent to the case of anisotropic thin film, while the latter case is commonly known. For the case of thin film, if the thickness does not affect the Landau level, it will lead to 3D anisotropic Ginzburg-Landau model and linear relation between temperature and upper critical field $H_{c2} = H_{c2}(0)(1 - T/T_c)$, while if the film is thin enough to strongly modify the Landau level, it will result in the 2D Tinkham model in which the square root behavior hold for the temperature and upper critical field $H_{c2} = H_{c2}(0)(1 - T/T_c)^{1/2}$. For the intermediate case, the power index (if fitted by power law function as in the main text) is between $1/2$ and 1 , and displays gradual change with the film thickness.

The analytic form of solution of (7.3) can be expressed by Kummer's function [123] [127], we performed the numerical calculation to reveal the relation between dimensionality and geometric parameter such as diameter and thickness of the wall. For a given set of geometric parameters of NT, namely the relative radius R/ξ_θ and the relative wall thickness d/ξ_r , as well as the anisotropic parameter $\Gamma = \xi_\theta/\xi_r$, we calculate the upper critical field as a function of temperature, and fit it by power law function to define the power index or the dimensionality. Figure 7-6 shows the contour plot of power index versus geometric parameters for several Γ values.

According to figure, we conclude that even for the NT case, the dimensionality is mainly determined by the thickness of wall. In other words, by measuring the temperature dependence of the upper critical field of superconducting NT in parallel magnetic field, the dimensionality or the effective thickness of superconducting NT can be estimated.

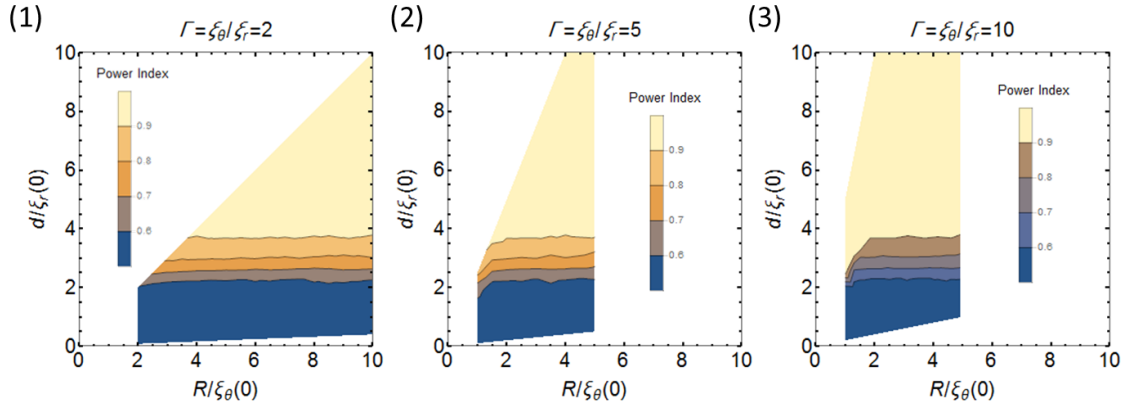


Figure 7-6: Contour plot of power index versus geometric parameters for different anisotropy.

Contour plot for different anisotropic parameters (1) $\Gamma = 2$, (2) $\Gamma = 5$, and (3) $\Gamma = 10$. The contour line is mainly flat, indicating that the power index does not depend on the effective radius, and depends only on the thickness of wall. The anomaly appears around effective radius below 2, because the fitting by power law function is not valid in the small radius region, due to large Little Parks oscillation [128].

Chapter 8

Nonreciprocal superconductivity in chiral WS₂ NTs

In this chapter, the chirality effects of WS₂ NT structure will be discussed. Chirality of materials is known to affect optical, magnetic and electric properties, causing a variety of nontrivial phenomena such as circular dichroism for chiral molecules [129][130], magnetic Skyrmions in chiral magnets [131], and nonreciprocal carrier transport in chiral conductors [132][133][134]. The nonreciprocal carrier transport will be introduced in the first part, chapter 8.1 Introduction to nonreciprocity. Then, a general description of nonreciprocal transport will be discussed in chapter 8-2 Nonlinear voltage response and photovoltaic effect, in which the photovoltaic effect will be also discussed. In the next part, chapter 8-3 Phenomenological description on superconducting nonreciprocal transport, a phenomenological description for superconducting chiral WS₂ NT will be shown. Finally, the experimental results of nonreciprocal superconducting transport will be shown and discussed in chapter 8-4 and 8-5 for the case of parallel and perpendicular magnetic field, respectively.

8-1 Introduction to nonreciprocity

8-1-1 Invariance property breaking due to symmetry breaking

The word, reciprocity, indicates some symmetric properties of a certain system, that is, the invariance property under some operations. For instance, if the object holds mirror symmetry, then the object will be looked the same wherever you see from left side or right side. To specify the reciprocity in this thesis, the meaning of the word is, if

the system holds inversion symmetry, then the electrical resistance of the system will be the same wherever you input the current from left side to right side or from right side to left side, as shown in equation (8.1).

$$R(\vec{I}) = R(-\vec{I}) \quad (8.1)$$

This is the usual case when people do experiments to measure the resistance of something with inversion symmetry.

On the other hand, if the system does not hold inversion symmetry, then the resistance of the system will not be the same for the two direction of input current. This is the non-reciprocity reflecting inversion symmetry breaking shown in equation (8.2).

$$R(\vec{I}) \neq R(-\vec{I}) \quad (8.2)$$

However, if we further consider the time reversal symmetry, for general electric conductivity tensor, L. Onsager have already proved [135][136] that in the quasi thermodynamic equilibrium case

$$\sigma_{ij} = \int_{-\infty}^0 \langle y_i(0) y_j(\tau) \rangle d\tau = \sigma_{ji}^{\dagger} \quad (8.3)$$

where \dagger denotes the time reversal transform. This equality indicates the resistance of one directed current is identical to the resistance of opposite directed current in which the system breaks inversion symmetry. Hence, the time reversal symmetry holds the relation as the equation below, even in the case of the system with broken inversion symmetry:

$$R(\vec{I}) = R(-\vec{I}) \quad (8.4)$$

If we want to see the effect on carrier transports due to inversion symmetry breaking, we must breaks time reversal symmetry at the same time. In addition, applying external magnetic field is the usual methods in laboratory to induce time reversal symmetry breaking. So if we include external magnetic field into the consideration, the time reversal symmetry holds the relation as below:

$$R(\vec{I}, \vec{B}) = R(-\vec{I}, -\vec{B}) \quad (8.5)$$

and the inversion symmetry holds the relation similar to (8.4)

$$R(\vec{I}, \vec{B}) = R(-\vec{I}, \vec{B}) \quad (8.4)^*$$

On the other hand, if the system does not hold inversion symmetry, then resulting in the following relation:

$$R(\vec{I}, \vec{B}) \neq R(-\vec{I}, \vec{B}) \quad (8.6)$$

From the equations labeled as (8.5) and (8.6), the resistance of one directed current is identical to the resistance of opposite directed current when the external magnetic field is not applied, consistent with the equation (8.4)*. The difference between the resistances of two opposite directed current is only observed when the external magnetic field is applied in the case of inversion symmetry breaking as equation (8.6).

Hence, the nonreciprocity of carrier transport is specialized for the electric resistance of two opposite directed electric current in the case of existence of external magnetic field when the system has broken inversion symmetry.

On the basis of symmetry arguments, considering about time reversal symmetry, the electric resistance in the case of existence of external magnetic field can be expressed as Taylor's expansion

$$R(\vec{I}, \vec{B}) = R(-\vec{I}, -\vec{B}) = R_0(1 + \alpha \vec{I}^2 + \beta \vec{B}^2 + \gamma \vec{I} \cdot \vec{B}) \quad (8.7)$$

up to second order terms. Here, R_0 denotes the electric resistance at zero external magnetic fields. The second term indicates the Joule heating effect, and the third term presents the normal quadratic dependent magnetoresistance, respectively. Next we further consider about inversion symmetry, the last term in the equation (8.7) must be zero, which is protected by the relation (8.4)*. However, if the system breaks inversion symmetry, the last term can be nonzero and linearly dependent on the external magnetic field, leading to the nonreciprocal electric resistance.

$$\Delta R(\vec{B}) = R(\vec{I}, \vec{B}) - R(-\vec{I}, \vec{B}) \propto \gamma R_0 \vec{I} \cdot \vec{B} \quad (8.8)$$

In addition, this phenomenon is sometimes called electric magnetochiral anisotropy (eMCHA) [132] which has been firstly reported fifteen years ago (in 2001) by G. L. J. A. Rikken in history. The reason why this phenomenon was named after chirality at that time is, by analogy to the polarization-dependent optical effect in chiral medium [129][137][138], this electric magneto-transport in chiral conductor was then proposed and observed [132]. On the other hand, this phenomenon is sometimes called magnetoelectric anisotropy (MEA) which has been reported eleven years ago (in 2005) by the same person, G. L. J. A. Rikken [139].

There are three possible phenomenological issues of the origin of such nonreciprocal transport, which are chiral scattering [132][134], magnetic self-field [132][133], and relativistic effect [139], respectively. In the next three sections, we will summarize these historical literatures and use a more general name for this phenomenon, the nonreciprocal transport, and also explain each possible issue of the origin of nonreciprocal transport.

8-1-2 Chiral scattering

First of all, the nonreciprocal transport may originate from the chiral scattering [132][134]. In general, the scattering probabilities of un-polarized electrons may be differently dependent on the different handed structures of molecules [140][141], and leading to the asymmetric results for the carrier transport which can be tuned by external magnetic field.

In Figure 8-1 [132], the authors have made two opposite torsion of bismuth wires named *L*-torsion and *D*-torsion, respectively. Here, *L* and *D* are the notation usually used in the optic research field to denote two circular polarization of light, respectively. Then, they have measured resistance difference as shown in equation (8.8), which clearly shows linear dependence on external magnetic field with opposite sign for *L*-torsion and *D*-torsion, respectively. Furthermore, they have concluded that such nonreciprocal transport originates from chiral scattering by lattice defect, because the nonreciprocal signal of *L*-torsion case decreases after annealing process for the bismuth wire in order to reduce lattice defect.

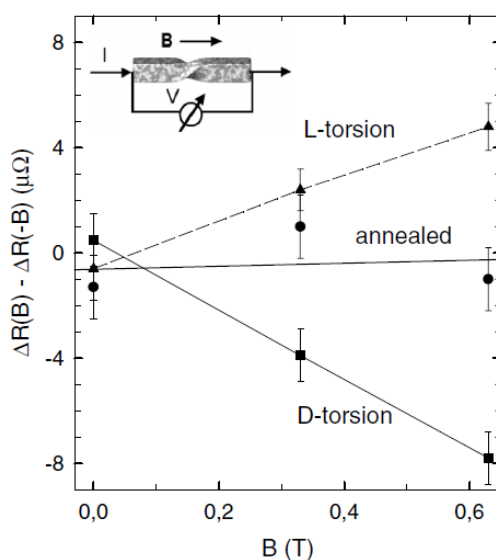


Figure 8-1: Electric magnetochiral anisotropic resistance of distorted bismuth wire.

The inset is the schematic figure of bismuth wire with a length of **10 mm** and a diameter of **0.5 mm**, measured at **77 K** and **0.2 A** of input current. Linearly fitted lines are shown for *L*-torsion (dashed) and *D*-torsion (solid), respectively.

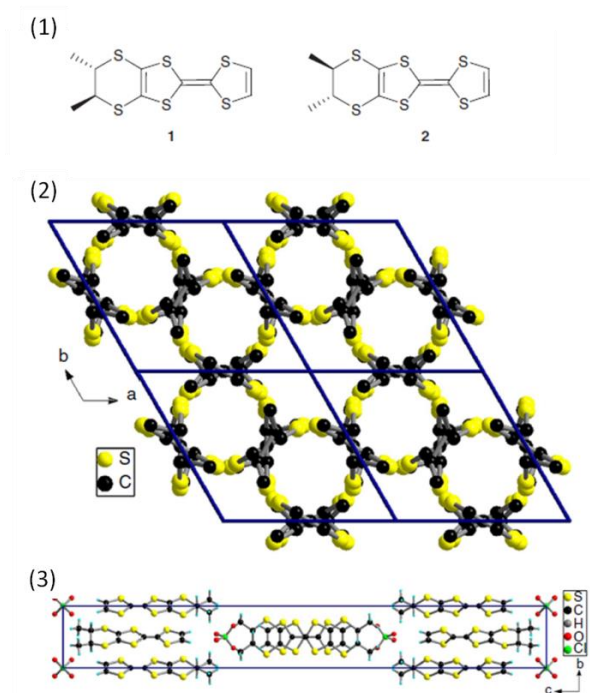


Figure 8-2: The schematic figures of handed molecules and composited crystal.

(1) The chiral molecules of (S,S)-DM-EDT-TTF (left) and (R,R)-DM-EDT-TTF (right). (2) Top view of [(S,S)-DM-EDT-TTF]₂ClO₄ with hexagonal structure. (3) Side view of the crystal.

Another experimental result has been reported on chiral molecules in crystal, as shown in Figure 8-2 and Figure 8-3. Figure 8-2 shows the chiral molecules of (S,S)-DM-EDT-TTF (Figure 8-2 (1) left) or (R,R)-DM-EDT-TTF (Figure 8-2 (1) right), and composited crystal. The experimental results are shown in Figure 8-3. The measured voltage between two probes linearly depends on external magnetic field and quadratically depends on input current, which agrees with equation (8.8). The quadratic dependence of effect on input current is equivalent to the linear dependence of resistance on input current.

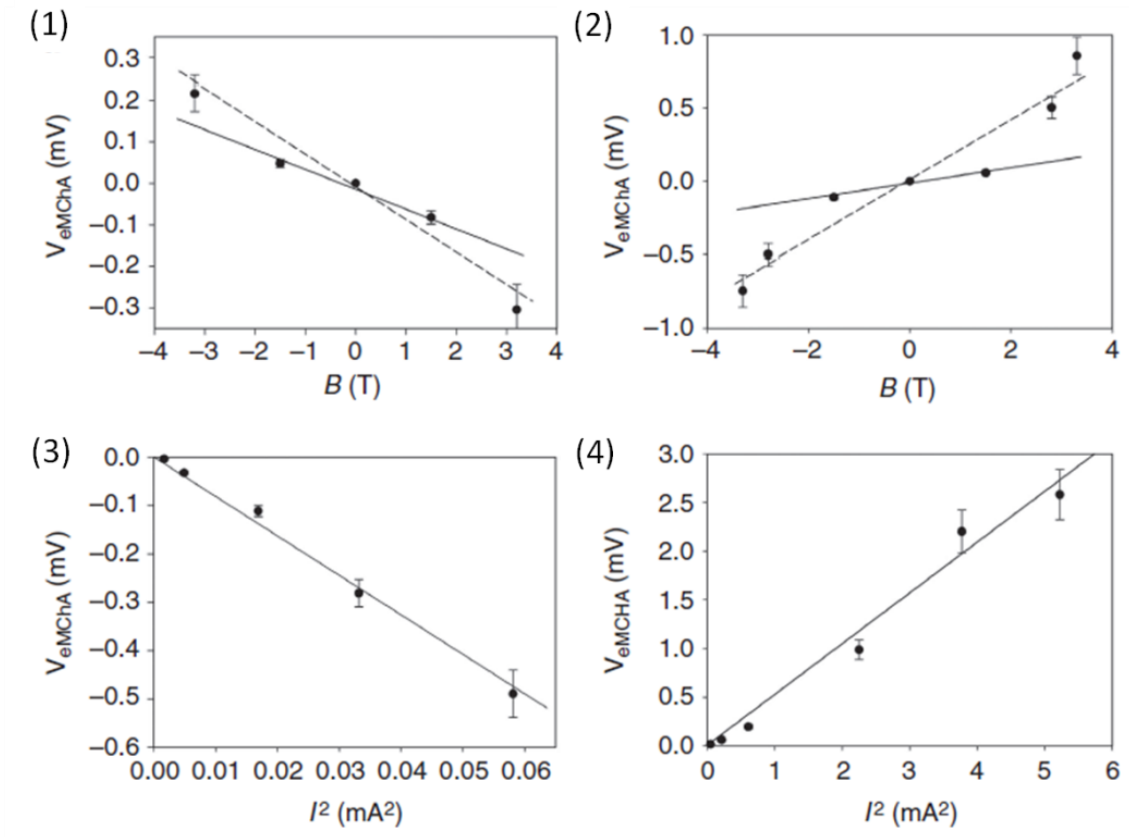


Figure 8-3: Effects of nonreciprocal electric transport.

(1)(2) The odd dependence of the effect on external magnetic field for two different handed molecular crystals. (3)(4) The quadratic dependence of effect on input current, which is equivalent to the linear dependence of resistance on input current.

8-1-3 Magnetic self-field

Secondly, the nonreciprocal transport may result from the magnetic self-field [132][133]. Because of the special geometry of the chiral conductor with broken

inversion symmetry, the current may generate additional magnetic field, which depends on both the direction of current flow and the handedness of the conductor. Considering the following model, in a solenoid, there is a self-field generated from current flow due to the helix geometry of the conductor.

$$B_{self} = \mu_0 n I \quad (8.9)$$

Simply considering nonchiral material, the resistance is given by usual quadratic dependence of magnetoresistance

$$R(B) = R_0(1 + \beta B^2) \quad (8.10)$$

If an external magnetic field B_{ext} is applied, the carrier feels total magnetic field $B_{ext} + B_{self}$ when the carrier transports. Then, it is easy to see that the resistance obeys the similar relation to the equation (8.7)

$$R(I, B_{ext}) = R_0 \left(1 + \beta B_{ext}^2 + 2\mu_0 n \beta I \cdot B_{ext} + O(I^2) \right) \quad (8.11)$$

up to the linear term on current. Hence, even in the case of nonchiral material, the nonreciprocal transport still may be generated from the current induced magnetic self-field due to the special geometry, which is linear for both input current and external magnetic field. The self-field also generates the quadratic relation of input current, which is usually treated as the Joule heating effect. The contributing factors of the quadratic term of input current are remained, waiting for further researches in the future.

Figure 8-4 [132] shows the experimental results of nonreciprocal signal for two distorted bismuth helices measured at 77 K when the external magnetic field is applied parallel to the axis of the helices. A clearly linear dependence of the nonreciprocal resistance on the external magnetic field is observed, with opposite sign for two opposite distorted helices.

In Figure 8-5 [133], people have measured the nonreciprocal transport in carbon nanotube (CNT) when the external magnetic field applied is parallel to the tube axis. The nonreciprocal signal as a function of external magnetic field is shown, clearly indicating a linear dependence of magnetic field as the equation (8.8).

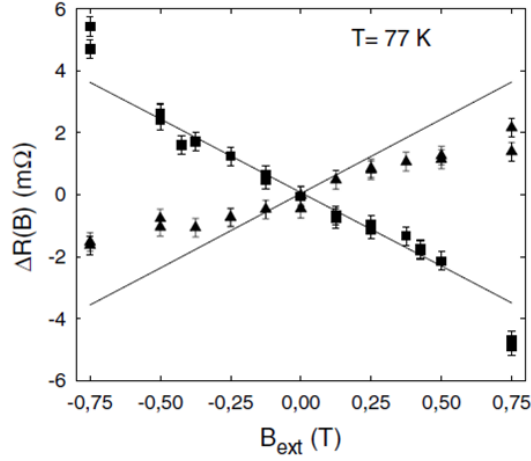


Figure 8-4: The nonreciprocal resistance of bismuth helices.

The D-torsion helix is shown in square, and the L-torsion helix is shown in triangle. These two helices are made with seven turns, **8 mm** diameter, and **0.8 mm** pitch and measured at $I = 0.2 \text{ A}$.

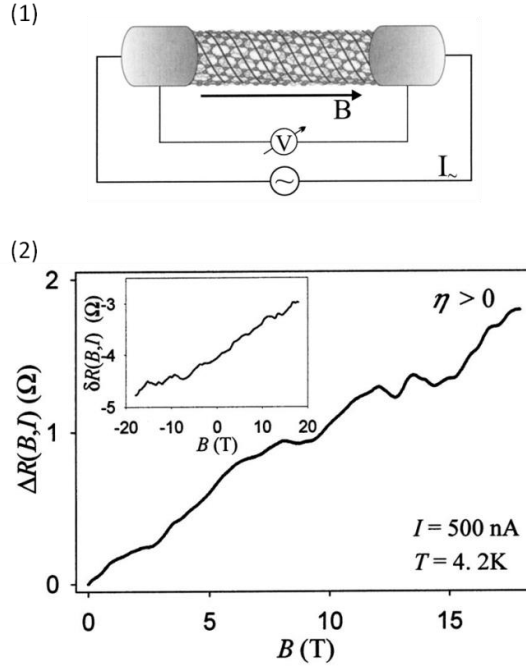


Figure 8-5: The nonreciprocal transport in CNT.

(1) The schematic figure of the experimental setup. (2) The nonreciprocal signal is shown as a function of external magnetic field. In set figure $\delta R(B, I) = R(B, I) - R(B, -I)$ is the resistance difference for opposite current input, and $\Delta R(B, I) = \delta R(B, I) - \delta R(-B, I)$ is the antisymmetrized resistance difference, which helps to reduce the experimental errors.

8.1.4 Relativistic effect

Thirdly, the nonreciprocal transport may be generated from the relativistic effect [139]. According to Onsager's relation by symmetry arguments, if a crossed external electric field is applied to the system, the nonreciprocal resistance exists in the direction perpendicular to both the external electric field and magnetic field (Figure 8-6 (1)).

The time reversal symmetry holds the relation similar to (8.5)

$$R(\vec{I}, \vec{E}, \vec{B}) = R(-\vec{I}, \vec{E}, -\vec{B}) \quad (8.5)^*$$

and the inversion symmetry holds the relation similar to (8.4)*

$$R(\vec{I}, \vec{E}, \vec{B}) = R(-\vec{I}, -\vec{E}, \vec{B}) \quad (8.4)^{**}$$

More specified, we find

$$\begin{aligned} R(\vec{I} \cdot (\vec{E} \times \vec{B})) &= R(-\vec{I} \cdot (\vec{E} \times -\vec{B})) = R(-\vec{I} \cdot (-\vec{E} \times \vec{B})) \\ &= R(\vec{I} \cdot (\vec{E} \times \vec{B})) \end{aligned} \quad (8.12)$$

As shown in (8.12), the term $\vec{I} \cdot (\vec{E} \times \vec{B})$ is invariance under time reversal symmetry and inversion symmetry. Hence, we conclude that the resistance for a system under crossed external electric field and magnetic field can be expressed as

$$R(\vec{I}, \vec{E}, \vec{B}) = R(\vec{I} \cdot (\vec{E} \times \vec{B})) = R_0(1 + \sigma \vec{I} \cdot (\vec{E} \times \vec{B}) + \gamma \vec{B}^2 + \dots) \quad (8.13)$$

In (8.13), the second term generates the nonreciprocal transport, which can be explained by a relativistic effect. If we transform to another moving frame to describe the system, the crossed external magnetic field will change to be zero and lead to normal magnetoresistance. Hence, such nonreciprocal transport phenomenon disappears in a special moving frame. The detailed calculation has been discussed in this paper [139].

The equation (8.13) also indicates that the nonreciprocal resistance is proportional to both the input current and external magnetic field, which has been confirmed by experiments in Figure 8-6 (2) and (3).

In general, the electric field breaks inversion symmetry of the system and then results in the nonreciprocal transport. The electric field in (8.13) may be externally applied by gate or FET structure, or naturally results from material polarization, such as Rashba type bulk material, noncentrosymmetric crystals, or interface of heterostructure.

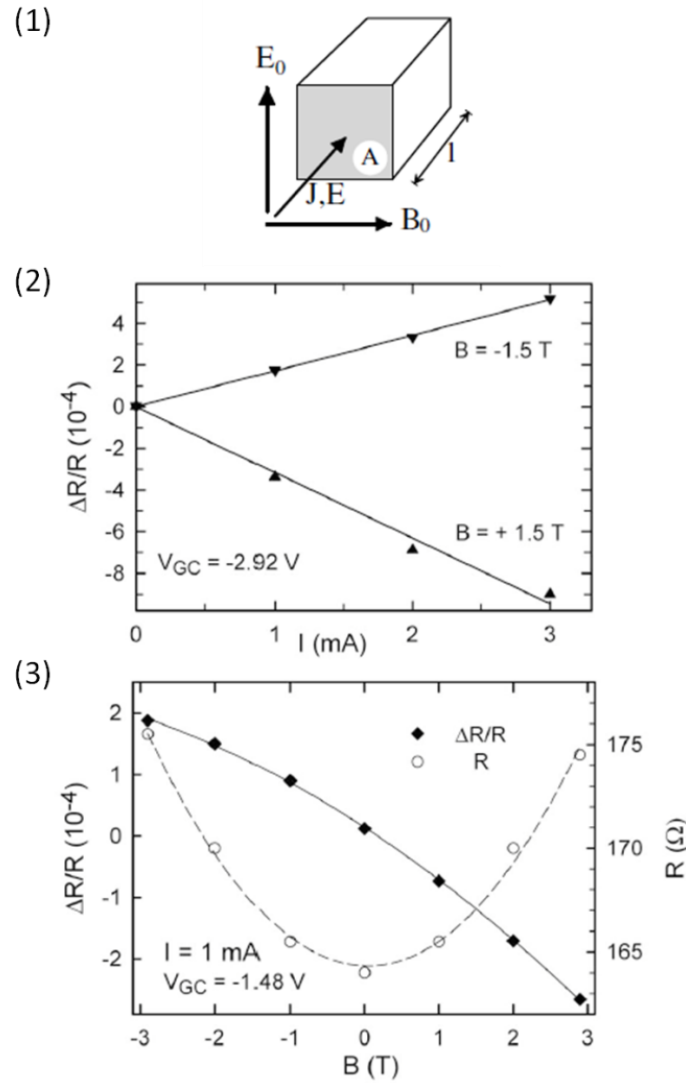


Figure 8-6: The nonreciprocal transport originating from the relativistic effect.

(1) A schematic figure of the model. (2) The nonreciprocal resistance as a function of input current is shown. (3) The nonreciprocal resistance (to left) and the resistance (to right) as a function of external magnetic field are shown.

In the end of this introduction, we summarized typical values of the parameter γ reflecting nonreciprocal transport [132][133][134][139], in Table 8-1, where the parameter is defined by

$$\frac{\Delta R(I, B)}{R_0} = \gamma IB \quad (8.14)$$

Origin	Chiral scattering		Magnetic self-field		Relativistic effect
materials	Bismuth wire	[DM-EDT-TTF] ₂ ClO ₄	Bismuth helix	CNT	FET structure
γ value	10^{-2}	10^{-2}	10^{-3}	10^3	10^{-1}

Table 8-1: Typical orders of the nonreciprocal parameters in different materials.

8-1-5 Measurement technique

In the end of this introduction, we introduce the measurement technique of nonreciprocal transport.

The nonreciprocal transport, of course, can be directly measured by swapping the direction of the direct current flow. However, the nonreciprocal signal is usually be detected through alternative current mode and measured by second harmonic signal via lock-in amplifiers. The current dependent term shown in the equation (8.7) leads to the nonlinear behavior in the voltage response which can be detected as the second harmonic signal in lock-in measurement.

If we apply alternative input current as $I = I_0 \sin \omega t$, then the voltage response is

$$V(t) = IR = IR_0(1 + \alpha I^2 + \beta B^2 + \gamma IB) \quad (8.15)$$

Among them, the second harmonic signal should be only generated by the quadratic current term which is indeed the chiral term. Hence, the second harmonic signal due to the chiral term can be expressed as follows

$$\begin{aligned}
V^{2\omega}(t) &= I\Delta R = IR_0\gamma IB = \gamma R_0 B I_0^2 \sin^2 \omega t \\
&= \frac{1}{2} \gamma R_0 B I_0^2 \left(1 + \sin\left(2\omega t - \frac{\pi}{2}\right)\right)
\end{aligned} \tag{8.16}$$

According to the equation (8.16), there is a $\pi/2$ phase shift between the first and the second harmonic signal. During the measurement, we should pick up the y -component of the second harmonic signal in order to reflect the $\pi/2$ phase shift, and also must confirm that the x -component is almost zero.

8-2 Nonlinear voltage response and photovoltaic effect

In the previous part, the nonreciprocal transport is introduced, and there possible issue of the origin of the nonreciprocity is discussed. More generally, the nonreciprocal transport originates from the nonlinear voltage response when applying electric field and then leading to the observed nonreciprocal resistance follows the equation (8.8). If we consider a nonlinear response of current generated by input electric field

$$j_i(\vec{E}) = \sigma_{ij}E_j + \gamma_{ijk}E_jE_k \tag{8.17}$$

up to the second order term of Taylor's expansion, where the first term expresses conductivity tensor, and the second term leads to the nonreciprocal transport.

$$j_i^{2\omega}(\vec{E}) = \gamma_{ijk}E_jE_k \tag{8.18}$$

It is amazing that in the history the nonreciprocal transport has been discovered analogy to the researches in optical field, now we re-find the relation between nonreciprocal transport and photocurrent generated by light. The equation (8.17) is often used to discuss the photocurrent in optical research field about photogalvanic effect. Because the frequency of the light, even infrared light, is too high to measure, the photocurrent we usually measured is the average current, or the direct component of the current, instead of the second harmonic signal in the nonreciprocal transport measurements.

Then, only the second term remains and results in the linear dependence of photocurrent on the intensity of linearly polarized incident light.

$$\langle j_i(\vec{E}) \rangle = \gamma_{ijk} \langle E_j E_k \rangle \quad (8.19)$$

According to the equation (8.16), the direct component has the exact same factor as the second harmonic component. Hence, we expect the similar intrinsic properties between the photogalvanic effect and the nonreciprocal transport measurements.

For the photogalvanic effect, such symmetry arguments have been already studied for the γ tensor in (8.19) upon spatial symmetry. For example, for the C_{3V} symmetry group which is the symmetry group of transition metal dichalcogenides materials, the non-zero components of the γ tensor are shown in the below.

Group class	γ tensor						
C_{3V} 4 components $m \perp y$		$E_x E_x$	$E_y E_y$	$E_z E_z$	$E_y E_z$	$E_z E_x$	$E_x E_y$
	j_x	γ_{xxx}	$-\gamma_{xxx}$	0	0	γ_{xzx}	0
	j_y	0	0	0	γ_{xzx}	0	$-\gamma_{xxx}$
	j_z	γ_{zxx}	γ_{zxx}	γ_{zzz}	0	0	0

Table 8-2: The γ tensor for the C_{3V} symmetry group.

The mirror plane is perpendicular to the y -axis. There are only 4 independent components, which are γ_{xxx} , γ_{xzx} , γ_{zxx} , and γ_{zzz} , respectively. Other non-zero components are represented by such 4 independent values.

Hence, similar to the photogalvanic effect, for the planar materials with C_{3V} symmetry, people can write down the expected nonreciprocal transport signal obeying (8.18):

$$j_x^{2\omega} = \gamma_{xxx} (E_x E_x - E_y E_y) \quad (8.20)$$

$$j_y^{2\omega} = -\gamma_{xxx} E_x E_y \quad (8.21)$$

where we assume that E_z is zero and we do not measure the out-plane signal.

According to the (8.20) and (8.21), we expect that the nonreciprocal transports occur in the materials with C_{3V} symmetry, and perform both longitude and transverse signals, even display the angular dependent nonreciprocal transports.

8-3 Phenomenological description

In this section, a phenomenological description on the superconducting chiral WS_2 NT will be discussed. Here, we summarize some temporary conclusions and make several assumptions in order to finalize the phenomenological description.

Conclusions:

① WS_2 NTs have chiral structures according to the electron diffraction analysis in Chapter 3.

② The chiral structure breaks inversion symmetry and thus generates the nonreciprocal transport, see Chapter 8.

③ The superconductivity in WS_2 NTs shows Little-Parks oscillation in the low field region, see Chapter 6, originated from the quantum interference of the supercurrent along the circumference of NT, and thus resultant oscillation of critical temperature and the magnetic flux quantization inside the NT.

Assumptions:

① Because the highly coherence nature of superconductivity, the nonreciprocal signal should be significantly enhanced in superconducting region.

② We further assume that the nonreciprocal signal is negligibly small, and for simple description, only focus on the nonreciprocal signal in superconducting region.

③ For a simple description, we assume that the multi-walled WS_2 NT contents unitary chirality.

④ The nonreciprocal signal should also reflect the Little-Parks oscillation with period of magnetic flux quantum.

Here, obeying the above conclusions and assumptions, we demonstrate a phenomenological description of on a general superconducting nonreciprocal transport and then specified it within in WS_2 NT, as shown in Figure 8-7.

A general superconducting nonreciprocal transport signal is expected as shown in Figure 8-7 (1). Following the assumptions ①, ②, and ③, the superconducting nonreciprocal transport signal is expected as linear dependence on the external magnetic field displayed by the dashed line. With the increasing external magnetic field, the measured $R^{2\omega}$ signal linearly increases, and then takes the maximum value at the upper critical field H_{C2} , and finally decreases to be zero or negligibly small when the superconductivity disappears at high field region.

On the other hand, the similar behavior is expected under opposite external magnetic field, and the measured $R^{2\omega}$ signal shows opposite sign. The nonreciprocal signal should be antisymmetric under the whole magnetic field region ranging from opposite direction to positive direction. Because the above discussion is only based on the symmetry arguments and the assumption of highly coherence nature of superconductivity, such a general description shown in Figure 8-7 (1) is expected to be universal for all of the materials with peculiar structure of broken inversion symmetry.

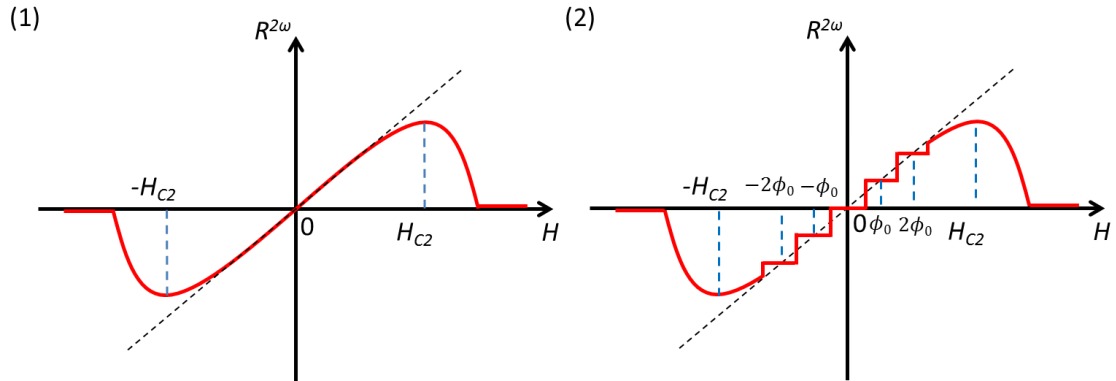


Figure 8-7: The schematic figure of expected nonreciprocal signal.

(1) A general superconducting nonreciprocal transport signal. The measured $R^{2\omega}$ signal is expected linearly increasing up to the H_{C2} , fitted as the dashed line. And then the measured $R^{2\omega}$ signal is expected decreasing to be zero or negligibly small in the normal state. The nonreciprocal signal should be antisymmetric under the whole magnetic field region ranging from opposite direction to positive direction. (2) A specified superconducting nonreciprocal transport signal in superconducting chiral NT configuration, exhibiting quantum plateaus in the low field region, originating from the magnetic flux quantization inside the NT associated with Little-Parks oscillation.

In addition to such superconducting nonreciprocal transport in the general

description, the superconducting nonreciprocal transport in the superconducting chiral NT is more special, due to the exhibiting of Little-Parks oscillation in the first harmonic signal. Because Little-Parks effect originates from the quantum interference of the supercurrent along the circumference of NT, and thus resultant the magnetic flux quantization inside the NT, the effective magnetic field affecting on the nonreciprocal transports also performs quantized behavior.

Hence, according to the equation (8.16), if the effective magnetic field displays a stepwise behavior, thus the second harmonic signal should display a stepwise behavior, too. As shown in Figure 8-7 (2), the nonreciprocal transport of the superconducting chiral NT is expected displaying the plateaus in the low field region, being associated with Little-Parks oscillation in the first harmonic signal.

8-4 The nonreciprocity in parallel magnetic field

In this section, the experimental results of nonreciprocal superconducting transport in parallel magnetic field will be discussed.

8-4-1 General discussion

The main results of the nonreciprocal superconducting transport in parallel magnetic field are shown in Figure 8-8.

Figure 8-8 (1) shows the magnetic field dependence of the second harmonic signal $R^{2\omega}$ at different temperatures. Finite antisymmetric $R^{2\omega}$ signal has been observed in the superconducting region, which unambiguously indicates the nonreciprocal transport due to the chiral structure of WS₂ NT. With the decreasing of temperature, the physical state of WS₂ NT tunes from the normal state into the superconducting state. In sharp contrast, the observed $R^{2\omega}$ signal is negligibly small in the normal state, indicating that the nonreciprocal transport signals are significantly enhance in the superconducting phase due to the coherence nature of superconductivity.

In addition, the maximum positions of the absolute minimum values of the observed $R^{2\omega}$ signal marked by solid and hollow triangles are shown in Figure 8-8 (1), consisting with the expected enhancement at upper critical field even at various temperatures (Figure 8-8 (2)), which reflect the intrinsic properties of inversion

symmetry breaking in the chiral WS₂ NT.

Besides for the broad the nonreciprocal superconducting transport signals (the word “broad” means comparable with upper critical field), in the low magnetic field region, the the nonreciprocal superconducting transport signals display the oscillating behavior with the period of the magnetic flux quantum, similar with Little-Parks oscillation in the R^{ω} signals (Figure 8-8 (3) to (5)). Such oscillating behavior in the $R^{2\omega}$ signals totally disappear in normal state (Figure 8-8 (3)), and enhance around critical temperature conjugated with Little-Parks oscillation (Figure 8-8 (6)), and finally display the stepwise behavior at low temperature. On the other hand, the oscillating amplitude is enhanced at the position of the disappearance of Little-Parks oscillation.

The observed quantum oscillation in $R^{2\omega}$ signals indicates that the nonreciprocal superconducting transport also has been tuned by the magnetic flux passing through the NT due to the interference nature of superconductivity.

Finally, according to Figure 8-8 (5), the nonreciprocal parameter γ is roughly estimated similar to the value of CNT.

$$\gamma = \frac{\Delta R(I, B)}{R_0 I B} \approx 10^3 \quad (8.22)$$

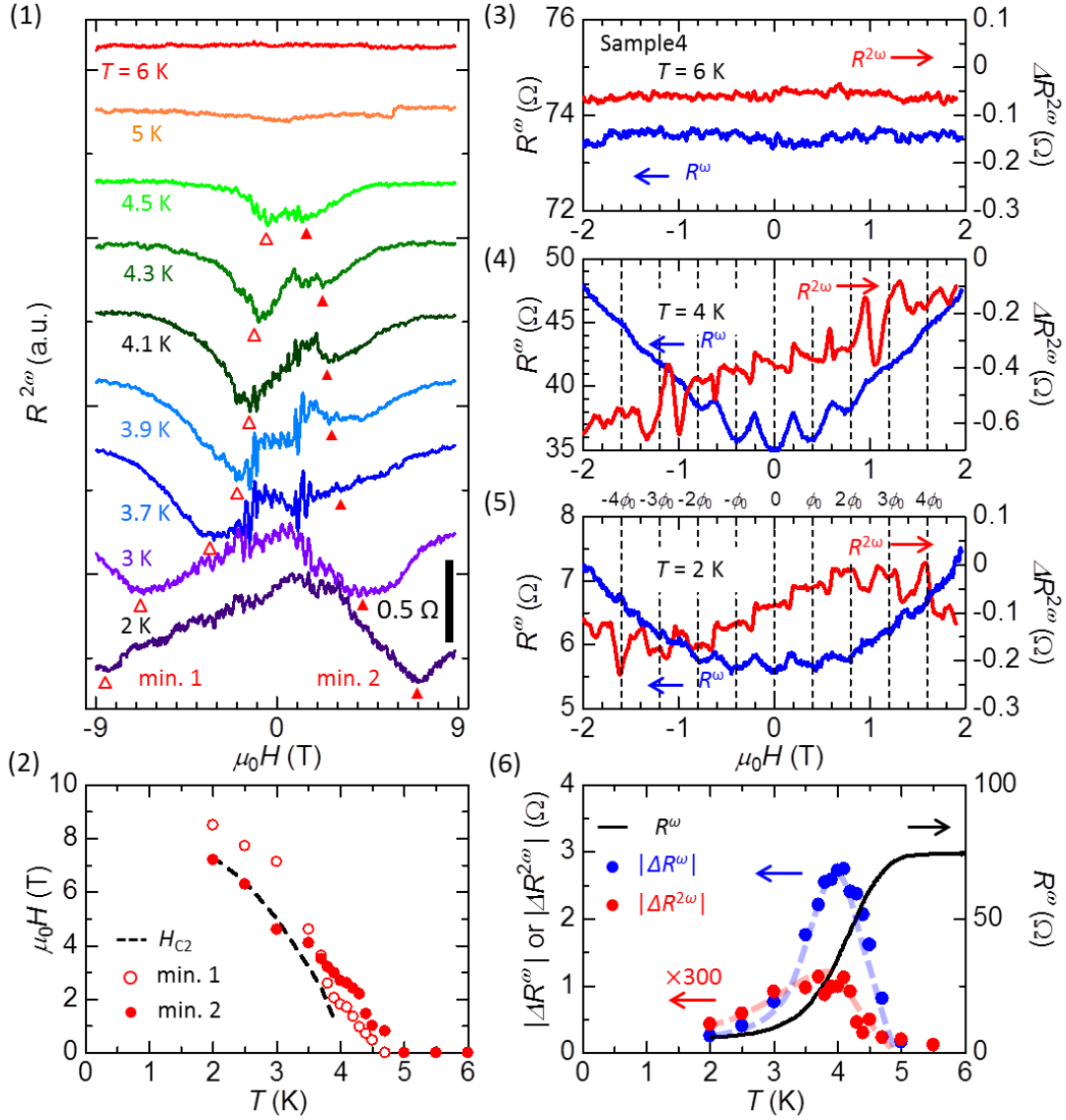


Figure 8-8: Nonreciprocal superconducting transport measured by the second harmonic signal in AC magnetoresistance.

(1) The magnetic field dependence of the second harmonic signal at various temperatures. In figure, only parts of the results are shown, but all of the results have been included in the consideration. The triangular marks denote the minima positions of the observed $R^{2\omega}$ signal. Each set of minimum positions gradually changes with temperature. (2) The diagram of the minima positions of the observed $R^{2\omega}$ signal vs temperature, and the upper critical field is shown in dashed line. The minima positions are consisting with the upper critical field. (3)(4)(5) Comparative plots of R^ω and $R^{2\omega}$ signals in low magnetic field region at characteristic temperature. (3) $T = 6$ K in normal state. (4) $T = 4$ K within

superconducting transition. (5) $T = 2$ K in deeply superconducting state. The $R^{2\omega}$ signals show same periodic oscillations associating with Little-Parks oscillation in R^ω signals in superconducting state, and the oscillating behavior disappeared in normal state for both R^ω and $R^{2\omega}$ signals. The $R^{2\omega}$ signals display the stepwise behavior at low temperature. (6) The temperature dependence of oscillating amplitudes for both R^ω and $R^{2\omega}$ signals. Both oscillating behaviors in R^ω and $R^{2\omega}$ signals are enhanced around T_c .

8-4-2 The symmetric nonreciprocal signal

The observed $R^{2\omega}$ signals have been symmetrized and shown in Figure 8-9. To be distinct with a general discussion, the minima positions totally consist with the upper critical fields denoted by triangular marks. Usually, the symmetrized nonreciprocal superconducting transport signals originates from the impurity, disordered, or defects of the sample, basically reflecting the inhomogeneity of the sample and being treated useless for the analysis.

However, such symmetrized nonreciprocal superconducting transport signals have provided two piece of important information.

First, the minima positions coincides with the upper critical fields, indicates that the intrinsic enhancement of nonreciprocal superconducting transport occurs in the superconducting region.

Second, compared with observed $R^{2\omega}$ signals, such symmetrized signals display significantly small oscillation, implying that all of the oscillations come from the antisymmetrized signals reflecting the intrinsic properties of superconducting chiral WS_2 NT.

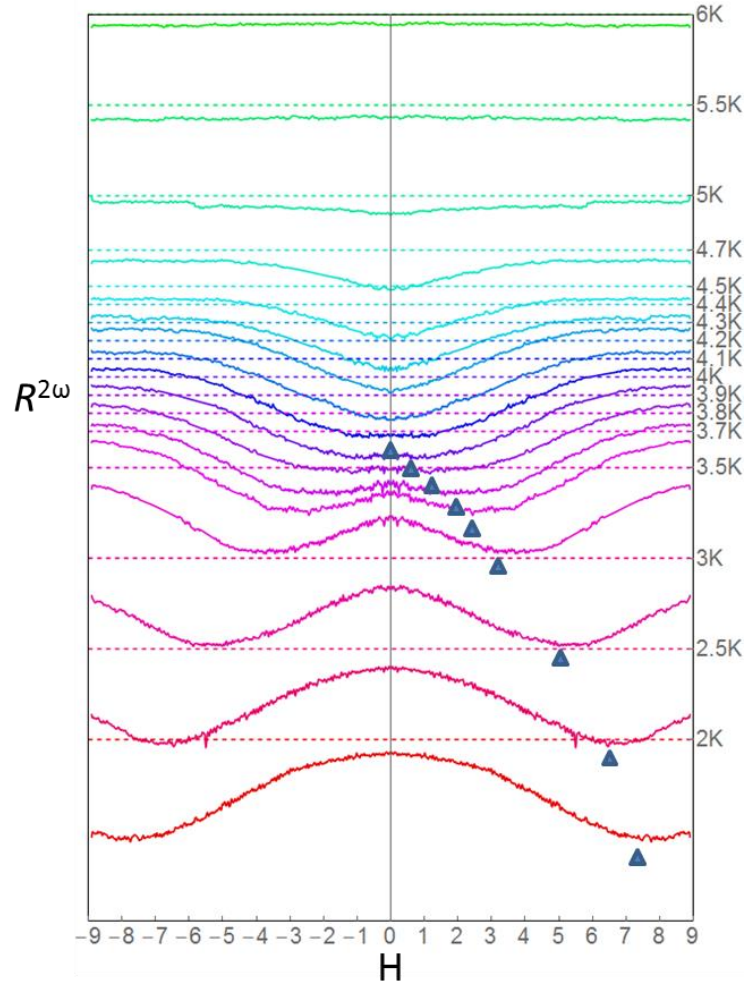


Figure 8-9: The symmetrized nonreciprocal superconducting transport signals.

The triangular marks denote the upper critical field for each temperature. The dashed line indicates the zero point for each temperature.

8-4-3 The antisymmetric nonreciprocal signal

The observed $R^{2\omega}$ signals have been antisymmetrized and shown in Figure 8-10. There is a clear oscillating behavior in the low field region as discussed in previous section. In the broad part of the antisymmetrized signal, on the other hand, there are several characteristic maxima and minima positions, changing with temperatures. The temperature dependence of each maxima and minima positions have been roughly estimated and shown in Figure 8-10 (2).

Obeying the phenomenological description of expected nonreciprocal transport

signal, the nonreciprocal signal shows a single peak around upper critical field with unitary chirality. It seems that the observed multi-peak behavior possibly reflects the multi-type of chirality in the multi-walled WS₂ NT. Thus, the observed WS₂ NT sample possibly contains several superconducting layers with different chirality, critical temperature, and upper critical field.

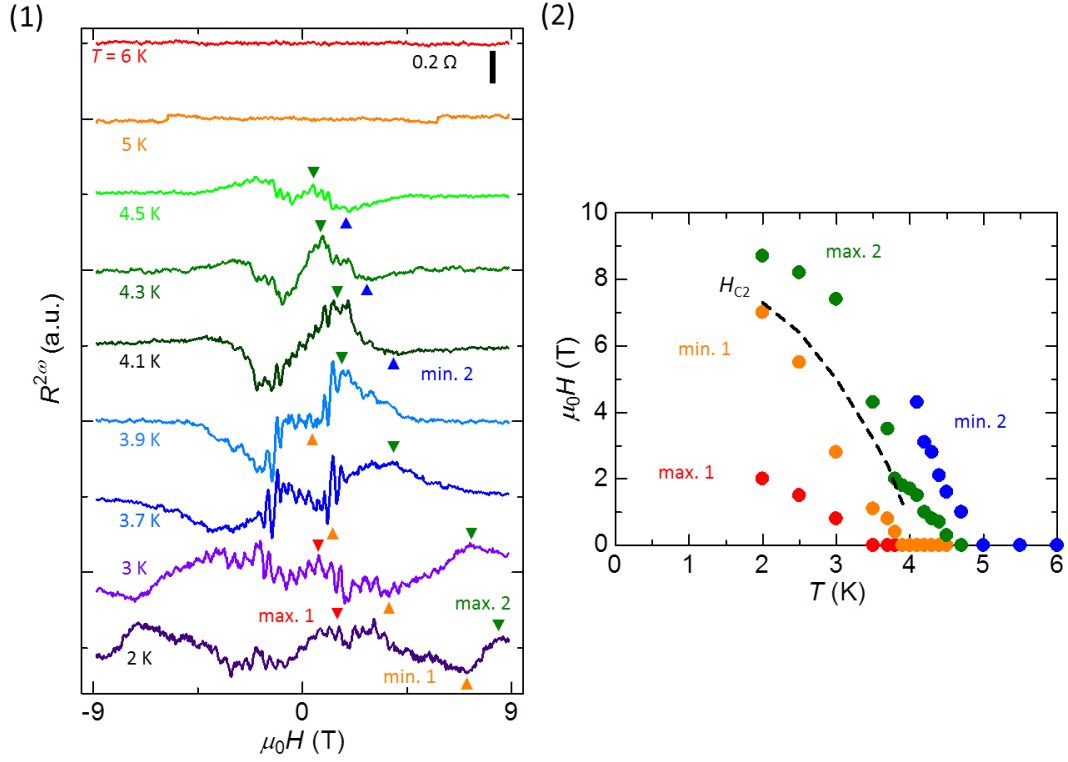


Figure 8-10: The antisymmetrized nonreciprocal superconducting transport signals.

(1) The antisymmetrized nonreciprocal superconducting transport signals displayed at different temperatures. The triangular marks roughly denote the minima or maxima positions. (2) The diagram of the minima or maxima positions vs temperature. The upper critical field is shown in dashed line. There are four different minima or maxima positions changing with temperature but showing similar tendency to the upper critical field, possibly indicating at least four component of the superconductivity in multi-walled WS₂ NT with different type of chirality, critical temperature and upper critical field.

8-5 The nonreciprocity in perpendicular magnetic field

8-5-1 Nonreciprocal signal in perpendicular magnetic field

Similar to the case of the parallel magnetic field, we have measured the nonreciprocal signal in the case of perpendicular magnetic field, as shown in Figure 8.11. Finite antisymmetric $R^{2\omega}$ signal has been observed in the superconducting region, which needs further discussion and researches.

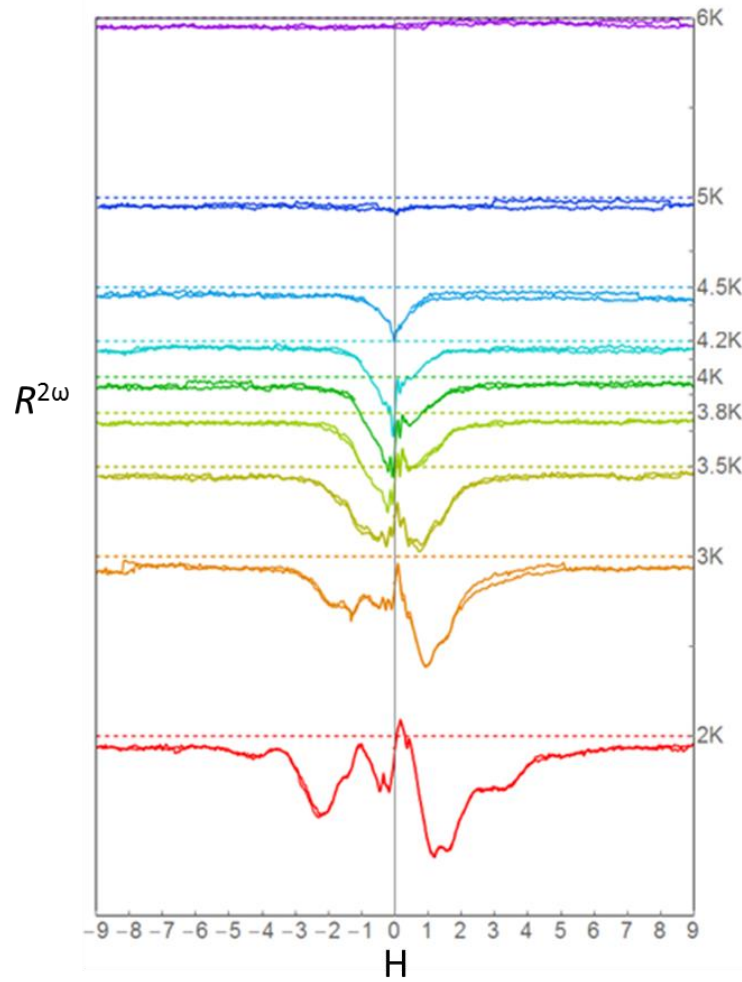


Figure 8-11: The observed nonreciprocal signal in perpendicular magnetic field.

Finite antisymmetric $R^{2\omega}$ signal has been observed in the superconducting region.

The observed $R^{2\omega}$ signals have been symmetrized and shown in Figure 8.11. The minima positions totally consist with the upper critical fields denoted by triangular marks, the same as the parallel magnetic field case, indicating the new physics behinds the symmetrized signal.

Usually, the symmetrized nonreciprocal superconducting transport signals originates from the impurity, disordered, or defects of the sample, basically reflecting the inhomogeneity of the sample and being treated useless for the analysis. However, in the totally different configurations, the similar enhancement has been observed, possibly indicating that the intrinsic enhancement of nonreciprocal superconducting transport occurs in the superconducting region.

Second, compared with observed $R^{2\omega}$ signals, such symmetrized signals display significantly small oscillation, implying that all of the oscillations come from the antisymmetrized signals reflecting the extrinsic properties of superconducting WS₂ NT.

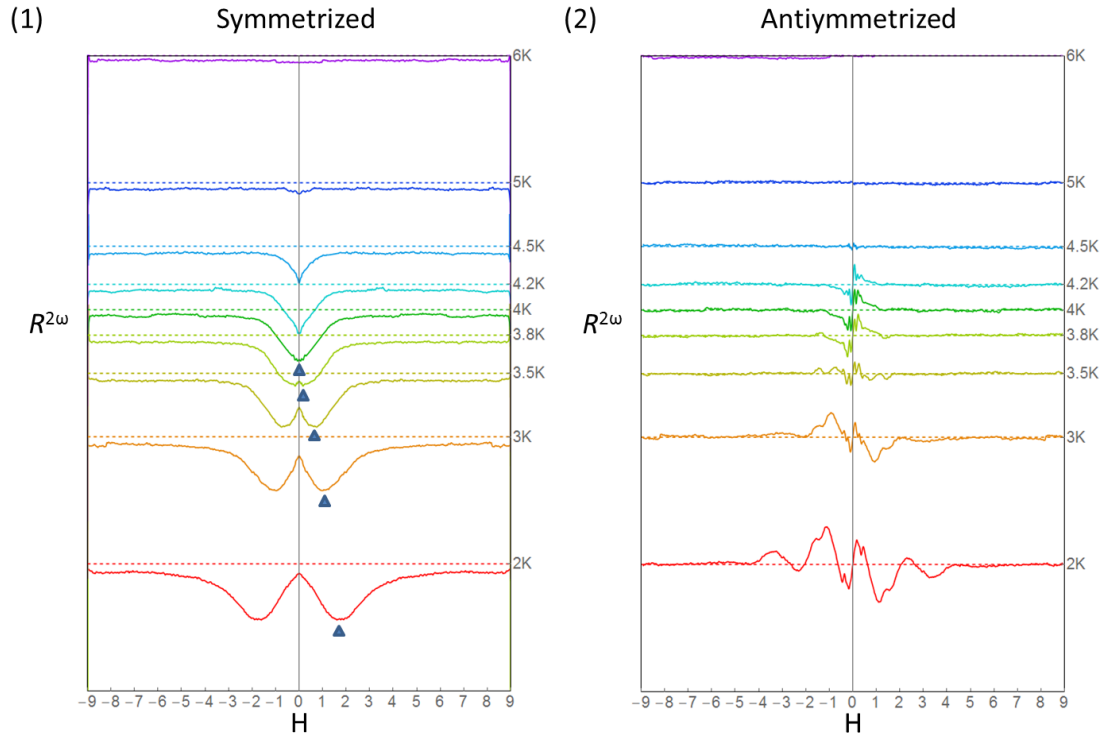


Figure 8-12: Symmetrized and antisymmetrized nonreciprocal signal.

(1) In symmetrized nonreciprocal signal, the triangle markers denote the upper critical field, consisting with the minima position of the symmetrized nonreciprocal signal. (2) In antisymmetrized nonreciprocal signal, there are also oscillating behaviors.

8-5-2 Possible Weber blockade phenomenon

So far, we have no knowledge about the oscillation nonreciprocal signal. Here, we assume that the oscillating behavior is come from the magnetic flux pass in or out the superconducting sample.

Even in the perpendicular magnetic field, the magnetic flux quantum still exists inside the superconducting NT but perpendicular to the wall. This is consisting with the possible intermediate state observed in the first harmonic signal.

This is nothing but the Weber blockade phenomenon [142][143][144], as shown in Figure 8-13, which is the same as we have demonstrated a quasi-one-dimensional superconducting transport exist in the perpendicular magnetic field. Because in the lower dimensions the interaction of vortices will be much enhanced compared with two dimensional (2D) systems, the vortices are repulsive to each other and stabilized at integer number of vortices piercing in finite size of device, possibly leading to the observed oscillating the antisymmetric second harmonic signal.

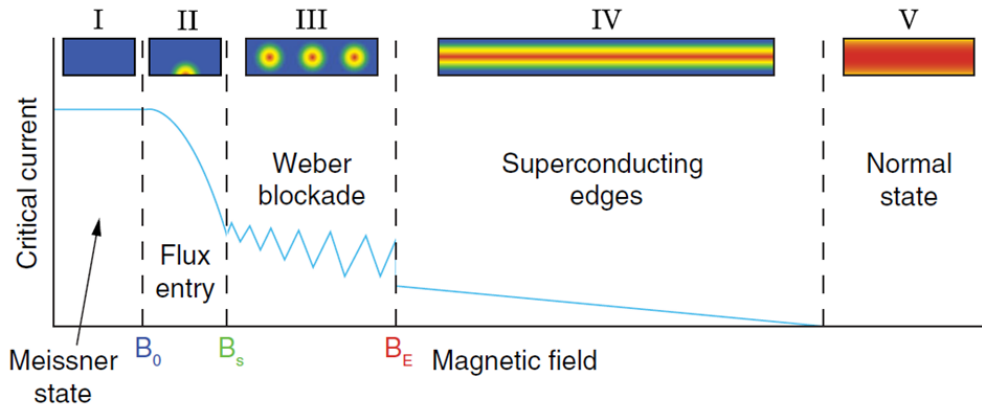


Figure 8-13: The schematic figure of Weber blockade.

With increasing the magnetic field, the magnetic flux quantum goes inside the cross of the NT, and stabilized at integer number of magnetic flux quantum. Then, the center part is filled by magnetic flux quantum and become non-superconducting, only the two sides remain superconducting. Finally, the total NT become normal and there is not antisymmetric signal have been observed.

With increasing the magnetic field, the magnetic flux quantum goes inside the cross of the NT, and stabilized at integer number of magnetic flux quantum. This

stabilizing process may result in the oscillating the nonreciprocal signal. Then, the center part is filled by magnetic flux quantum and become non-superconducting, only the two sides remain superconducting. This leads to the broad component of the observed nonreciprocal signal. Finally, the total NT become normal and there is not antisymmetric signal have been observed.

Chapter 9

Summary

In this whole study, basic physical transport properties of the semiconducting inorganic tungsten disulfide (WS_2) nanotubes (NT) have been investigated by using the electric double layer transistor (EDLT) techniques and the phase sensitive measurements on both the first and the second harmonic signal. The study is not confined within the demonstration of high performance of field effect on individual WS_2 NT by EDLT, but also the discovery of a new functionality such as the nonreciprocity of superconductivity for the first time.

First of all, this is the first experimental study that has been reported on the ionic liquid gating response of an individual multi-walled WS_2 NT. The carrier density of WS_2 NT has been successfully tuned by EDLT, and the ambipolar transfer curve with a high on/off ratio ($> 10^2$) has been observed for both hole and electron sides. In addition to the electrostatic doping in electric double layer region, the electrochemical doping has been realized, and thus the superconductivity was realized for the first time in individual NTs.

Second, this is the first experimental research that has been investigated on the superconductivity in an individual NT. Besides the anisotropic of the superconductivity in the external magnetic field, the magnetoresistance have shown the periodic oscillation during the superconducting transition, known as Little-Parks effect, originating from the quantum interference of the supercurrent along the circumference of NT and thus resultant oscillation of critical temperature. These results are the solid evidence that the superconductivity occurs in the cylindrical structure, and provide clear information of the effective diameter of NTs. By summarizing the relation between

effective diameter and the critical temperature, a nontrivial relation was found that the critical temperature decreases linearly as a function of inverse diameter. This result gives an insight to the pairing mechanisms of superconductivity.

Third, this is the first experimental discovery that has been demonstrated on the nonreciprocity of superconductivity. This is the first unambiguous evidence of the superconductivity reflecting chiral structure of NT in which the forward and backward supercurrent flows are not equivalent because of inversion symmetry breaking. The observed nonreciprocal signal has been significantly enhanced within the superconducting state due to the highly coherence nature of superconductivity, and became negligibly small in the normal state. In the low field region, the nonreciprocal signal has been measured in detail, being associated with unprecedented quantum Little-Parks oscillation in the configuration of external magnetic field parallel to the NT axis. The present results inspire researchers to further pursue the research on the microscopic mechanism of nonreciprocity of superconductivity and pairing symmetry in chiral or noncentrosymmetric structure.

On the other hand, this whole study has remained several topics to be further investigated in the future.

For example, clarification of the nonreciprocal superconductivity in WS₂ NT via direct current injection, and investigation on other superconducting properties performed by direct current, such as Weber blockade, superconducting gap, and critical current. And, research on other physical properties and new functionalities should be further explored for the application of WS₂ NT, such as thermoelectric and optical properties.

For the knowledge of basic physics, this study indicates the nonreciprocity should be a new approach toward the superconductors with chiral or noncentrosymmetric structure. In the view of wealthy family of materials, this study implies the inorganic NT should be a new platform for the researches on nanoscaled devices beyond carbon NT.

Reference

- [1] K. S. Novoselov, A. K. Geim, S. V. Morozov, D. Jiang, Y. Zhang, S. V. Dubonos, I. V. Grigorieva, and A. A. Firsov, *Science* **306**, 666 (2004)
- [2] A. H. C. Neto, F. Guinea, N. M. R. Peres, K. S. Novoselov, and A. K. Geim, *Rev. Mod. Phys.* **81**, 109 (2009)
- [3] A. K. Geim, *Science* **324**, 1530 (2009)
- [4] "The Nobel Prize in Physics 2010". Nobelprize.org. Nobel Media AB 2014. http://www.nobelprize.org/nobel_prizes/physics/laureates/2010/
- [5] A. C. Neto, F. Guinea, and M. N. Peres, *Phys. World* **19**, 33 (2006)
- [6] M. I. Katsnelson, K. S. Novoselov, and A. K. Geim, *Nature Phys.* **2**, 620 (2006)
- [7] M. I. Katsnelson, and K.S. Novoselov, *Solid State Comum.* **143**, 3 (2007)
- [8] A. A. Balandin, S. Ghosh, W. Bao, I. Calizo, D. Teweldebrhan, F. Miao and C. N. Lau, *Nano Lett.* **8**, 902 (2008)
- [9] F. Ebrahimi, *Graphene – New trends and developments*, (InTheh, 2015)
- [10] B. Aïssa, N. K. Memon, A. Ali, and M. K. Khraisheh, *Front. Mater.* **2**:58 (2015)
- [11] P. Avouris, and C. Dimitrakopoulos, *Materials Today* **15**, 86 (2012)
- [12] V. P. Gusynin, and S. G. Sharapov, *Phys. Rev. Lett.* **95**, 146801 (2005)
- [13] K. S. Novoselov, A. K. Geim, S. V. Morozov, D. Jiang, M. I. Katsnelson, I. V. Grigorieva, S. V. Dubonos, and A. A. Firsov, *Nature* **438**, 197 (2005)
- [14] Y. Zhang, Y. Tan, H. L. Stormer, and P. Kim, *Nature* **438**, 201 (2005)
- [15] K. S. Novoselov, Z. Jiang, Y. Zhang, S. V. Morozov, H. L. Stormer, U. Zeitler, J. C. Maan, G. S. Boebinger, P. Kim, and A. K. Geim, *Science* **315**, 1379 (2007)
- [16] K. v. Klitzing, G. Dorda, and M. Pepper, *Phys. Rev. Lett.* **45**, 494 (1980)
- [17] X. Lu, M. Yu, H. Huang, and R. S. Ruoff, *Nanotech* **10**, 269 (1999)
- [18] A. Gupta, T. Sakthivel, and S. Seal, *Progress in Materials Science* **73**, 44 (2015)
- [19] G. R. Bhimanapati, Z. Lin, V. Meunier, Y. Jung, J. Cha, S. Das, D. Xiao, Y. Son, M. S. Strano, V. R. Cooper, L. Liang, S. G. Louie, E. Ringe, W. Zhou, S. S. Kim, R. R. Naik, B. G. Sumpter, H. Terrones, F. Xia, Y. Wang, J. Zhu, D. Akinwande, N. Alem, J. A. Schuller, R. E. Schaak, M. Terrones, and J. A. Robinson, *ACS*

- Nano* **9**, 11509 (2015)
- [20] A. K. Geim, and I. V. Grigorieva, *Nature* **499**, 419 (2013)
 - [21] S. Das, J. A. Robinson, M. Dubey, H. Terrones, and M. Terrones, *Annu. Rev. Mater. Res.* **45**, 1 (2015)
 - [22] B. Aufray, A. Kara, S. Vizzini, H. Oughaddou, C. Léandri, B. Ealet, and G. L. Lay, *Appl. Phys. Lett.* **96**, 183102 (2010)
 - [23] B. Lalmi, H. Oughaddou, H. Enriquez, A. Kara, S. Vizzini, B. Ealet, and B. Aufray, *Appl. Phys. Lett.* **97**, 223109 (2010)
 - [24] L. Tao, E. Cinquanta, D. Chiappe, C. Grazianetti, M. Fanciulli, Madan Dubey, A. Molle, and D. Akinwande, *Nature Nanotech.* **10**, 227 (2015)
 - [25] E. Bianco, S. Butler, S. Jiang, O. D. Restrepo, W. Windl, and J. E. Goldberger, *ACS Nano* **7**, 4414 (2013)
 - [26] A. Acun, L. Zhang, P. Bampoulis, M. Farmanbar, A. van Houselt, A. N. Rudenko, M. Lingenfelder, G. Brocks, B. Poelsema, M. I. Katsnelson and H. J. W. Zandvliet, *J. Phys. Condens. Matter.* **27**, 443002 (2015)
 - [27] F. Zhu, W. Chen, Y. Xu, C. Gao, D. Guan, C. Liu, D. Qian, S. Zhang, and J. Jia, *Nature Mater.* **14**, 1020 (2015)
 - [28] L. Li, Y. Yu, G. Ye, Q. Ge, X. Ou, H. Wu, D. Feng, X. Chen, and Y. Zhang, *Nature Nanotech.* **9**, 372 (2014)
 - [29] Y. Saito, and Y. Iwasa, *ACS Nano* **9** (3), (2015) pp 3192–3198
 - [30] Q. Wang, K. Kalantar-Zadeh, A. Kis, J. N. Coleman, and M. S. Strano, *Nature Nanotech.* **7**, 699 (2012)
 - [31] M. Chhowalla, H. S. Shin, G. Eda, L. Li, K. P. Loh, and H. Zhang, *Nature Chemistry* **5**, 263 (2013)
 - [32] X. Xu, W. Yao, D. Xiao, and T. F. Heinz, *Nature Phys.* **10**, 343 (2014)
 - [33] D. Jariwala, V. K. Sangwan, L. J. Lauhon, T. J. Marks, and M. C. Hersam, *ACS Nano* **8**, 1102 (2014)
 - [34] C. Gong, H. Zhang, W. Wang, L. Colombo, R. M. Wallace and K. Cho, *Appl. Phys. Lett.* **103**, 053513 (2013)
 - [35] A. Splendiani, L. Sun, Y. Zhang, T. Li, J. Kim, C. Chim, G. Galli, and F. Wang, *Nano Lett.* **10** 1271 (2010)
 - [36] B. Radisavljevic, A. Radenovic, J. Brivio, V. Giacometti, and A. Kis, *Nature Nanotech.* **6**, 147 (2011)
 - [37] H. Zeng, J. Dai, W. Yao, D. Xiao, and X. Cui, *Nature Nanotech.* **7**, 490 (2012)
 - [38] K. F. Mak, K. He, J. Shan, and T. F. Heinz, *Nature Nanotech.* **7**, 494 (2012)
 - [39] T. Cao, G. Wang, W. Han, H. Ye, C. Zhu, J. Shi, Q. Niu, P. Tan, E. Wang, B. Liu,

- and J. Feng, *Nature Comm.* **3**, 887 (2012)
- [40] D. Xiao, G. Liu, W. Feng, X. Xu, and W. Yao, *Phys. Rev. Lett.* **108**, 196802 (2012)
 - [41] R. Suzuki, M. Sakano, Y. J. Zhang, R. Akashi, D. Morikawa, A. Harasawa, K. Yaji, K. Kuroda, K. Miyamoto, T. Okuda, K. Ishizaka, R. Arita, and Y. Iwasa, *Nature Nanotech.* **9**, 611 (2014)
 - [42] Y. J. Zhang, T. Oka, R. Suzuki, J. T. Ye, and Y. Iwasa, *Science* **344**, 725 (2014)
 - [43] C. H. Ahn, J. M. Triscone, and J. Mannhart, *Nature* **424**, 1015 (2003)
 - [44] C. H. Ahn, A. Bhattacharya, M. Di Ventura, J. N. Eckstein, C. Daniel Frisbie, M. E. Gershenson, A. M. Goldman, I. H. Inoue, J. Mannhart, Andrew J. Millis, Alberto F. Morpurgo, D. Natelson, and J. M. Triscone, *Rev. Mod. Phys.* **78**, 1185 (2006)
 - [45] H. T. Yuan, H. Shimotani, A. Tsukazaki, A. Ohtomo, M. Kawasaki, and Y. Iwasa, *Adv. Funct. Mater.* **19**, 1046 (2009)
 - [46] Y. Yamada, K. Ueno, T. Fukumura, H. T. Yuan, H. Shimotani, Y. Iwasa, L. Gu, S. Tsukimoto, Y. Ikumura, M. Kawasaki, *Science* **332**, 1065 (2011)
 - [47] H. Yuan, H. Liu, H. Shimotani, H. Guo, M. Chen, Q. Xue, and Y. Iwasa, *Nano Lett.* **11**, 2601 (2011)
 - [48] Y. Zhang, J. Ye, Y. Matsushashi, and Y. Iwasa, *Nano Lett.* **12**, 1136 (2012)
 - [49] K. Ueno, S. Nakamura, H. Shimotani, A. Ohtomo, N. Kimura, T. Nojima, H. Aoki, Y. Iwasa, and M. Kawasaki, *Nature Mater.* **7**, 855 (2008)
 - [50] J. T. Ye, S. Inoue, K. Kobayashi, Y. Kasahara, H. T. Yuan, H. Shimotani, and Y. Iwasa, *Nature Mater.* **9**, 125 (2010)
 - [51] K. Ueno, S. Nakamura, H. Shimotani, H. T. Yuan, N. Kimura, T. Nojima, H. Aoki, Y. Iwasa, and M. Kawasaki, *Nature Nanotech.* **6**, 408 (2011)
 - [52] J. T. Ye, Y. J. Zhang, R. Akashi, M. S. Bahramy, R. Arita, Y. Iwasa, *Science* **338**, 1193 (2012)
 - [53] M. Nakano, K. Shibuya, D. Okuyama, T. Hatano, S. Ono, M. Kawasaki, Y. Iwasa, and Y. Tokura, *Nature* **487**, 495 (2012)
 - [54] M. Yoshida, Y. Zhang, J. Ye, R. Suzuki, Y. Imai, S. Kimura, A. Fujiwara, and Y. Iwasa, *Sci. Rep.* **4**, 7302 (2014)
 - [55] M. Yoshida, R. Suzuki, Y. Zhang, M. Nakano and Y. Iwasa, *Sci. Adv.* **1**, e1500606 (2015)
 - [56] Y. Saito, Y. Kasahara, J. Ye, Y. Iwasa, and T. Nojima, *Science* **350**, 409 (2015)
 - [57] Y. Saito, Y. Nakamura, M. S. Bahramy, Y. Kohama, J. Ye, Y. Kasahara, Y. Nakagawa, M. Onga, M. Tokunaga, T. Nojima, Y. Yanase, and Y. Iwasa, *Nature*

- Physics* **12**, 144 (2016)
- [58] J. M. Lu, O. Zheliuk, I. Leermakers, N. F. Q. Yuan, U. Zeitler, K. T. Law, J. T. Ye, *Science* **350**, 1353 (2015)
 - [59] S. Jo, D. Costanzo, H. Berger, and A. F. Morpurgo, *Nano Lett.* **15** (2), (2015) pp 1197–1202
 - [60] W. Shi, J. Ye, Y. Zhang, R. Suzuki, M. Yoshida, J. Miyazaki, N. Inoue, Y. Saito, Y. Iwasa, *Sci.c Rep.* **5**, 12534 (2015)
 - [61] Y. Saito, T. Nojima, and Y. Iwasa, *Supercond. Sci. Technol.* **29**, 093001 (2016)
 - [62] X. Xi, Z. Wang, W. Zhao, J. Park, K. T. Law, H. Berger, L. Forró, J. Shan, and K. F. Mak, *Nature Phys.* **12**, 139 (2016)
 - [63] Y. Yu, F. Yang, X. F. Lu, Y. J. Yan, Y. Cho, L. Ma, X. Niu, S. Kim, Y. Son, D. Feng, S. Li, S. Cheong, X. H. Chen, and Y. Zhang, *Nature Nanotech.* **10**, 270 (2015)
 - [64] S. Iijima, *Nature* **354**, 56 (1991)
 - [65] J. Charlier, X. Blase, and S. Roche, *Rev. Mod. Phys.* **79**, 677 (2007)
 - [66] P. J. F. Harris, *Carbon Nanotube Science – Synthesis, Properties, and Applications*, (Cambridge Univ. Press, Cambridge, 2009)
 - [67] A. Bachtold, C. Strunk, J. Salvetat, J. Bonard, L. Forró, T. Nussbaumer, and C. Schönenberger, *Nature* **397**, 673 (1999)
 - [68] P. Jarillo-Herrero, S. Sapmaz, C. Dekker, L. P. Kouwenhoven, and H. S. J. van der Zant, *Nature* **429**, 389 (2004)
 - [69] W. Liang, M. Bockrath, D. Bozovic, J. H. Hafner, M. Tinkham, and H. Park, *Nature* **411**, 665 (2001)
 - [70] J. Cao, Q. Wang, M. Rolandi, and H. Dai, *Phys. Rev. Lett.* **93**, 216803 (2004)
 - [71] M. Kociak, A. Yu. Kasumov, S. Guéron, B. Reulet, I. I. Khodos, Yu. B. Gorbatov, V. T. Volkov, L. Vaccarini, and H. Bouchiat, *Phys. Rev. Lett.* **86**, 2416 (2001)
 - [72] Z. K. Tang, Lingyun Zhang, N. Wang, X. X. Zhang, G. H. Wen, G. D. Li, J. N. Wang, C. T. Chan, and P. Sheng, *Science* **292**, 2462 (2001).
 - [73] I. Takesue, J. Haruyama, N. Kobayashi, S. Chiashi, S. Maruyama, T. Sugai, and H. Shinohara, *Phys. Rev. Lett.* **96**, 057001 (2006).
 - [74] W. Shi, Z. Wang, Q. Zhang, Y. Zheng, C. Jeong, M. He, R. Lortz, Y. Cai, N. Wang, T. Zhang, H. Zhang, Z. Tang, P. Sheng, H. Muramatsu, Y. A. Kim, M. Endo, P. T. Araujo, and M. S. Dresselhaus *Sci. Rep.* **2**, 625 (2012).
 - [75] R. Levi, J. Gare, D. Teich, G. Seifert, R. Tenne, and E. Joselevich, *ACS Nano* **9**, 12224 (2015)
 - [76] R. Tenne, L. Margulis, M. Genut, and G. Hodes, *Nature* **360**, 444 (1992)

- [77] R. Tenne, *Nature Nanotech.* **1**, 103 (2006)
- [78] M. B. Sadan, L. Houben, A. N. Enyashin, G. Seifert, and R. Tenne, *PNAS* **105**, 15643 (2008)
- [79] C. Zhang, Z. Ning, Y. Liu, T. Xu, Y. Guo, A. Zak, Z. Zhang, S. Wang, R. Tenne and Q. Chen, *Appl. Phys. Lett.* **101**, 113112 (2012)
- [80] C. Zhang, S. Wang, L. Yang, Y. Liu, T. Xu, Z. Ning, A. Zak, Z. Zhang, R. Tenne and Q. Chen, *Appl. Phys. Lett.* **100**, 243101 (2012)
- [81] M. Sugahara¹, H. Kawai¹, Y. Yomogida, Y. Maniwa, S. Okada, and K. Yanagi, *Appl. Phys. Exp.* **9**, 075001 (2016)
- [82] A. Rothschild, J. Sloan, and R. Tenne, *J. Am. Chem. Soc.*, **122** 5169 (2000)
- [83] A. Zak, L. Sallacan-Ecker, A. Margolin, Y. Feldman, R. Popovitz-Biro, A. Albu-Yaron, M. Genut, and R. Tenne, *Fullerene, Nanotubes, Carbon Nanostruct.* **19**, 18 (2011)
- [84] R. Levi, O. Bitton, G. Leituss, R. Tenne, and E. Joselevich, *Nano Lett.*, **13** 3736 (2013)
- [85] O. Tevet, O. Goldbart, S. R. Cohen, R. Rosentsveig, R. Popovitz-Biro, H. D. Wagner, and R. Tenne, *Nanotechnology* **21**, 365705 (2010)
- [86] L. Margulis, P. Dluzewski, Y. Feldman, and R. Tenne, *J. of Micro.* **181**, 68 (1996)
- [87] A. Johansson, G. Sambandamurthy, D. Shahar, N. Jacobson, and R. Tenne, *Phys. Rev. Lett.* **95**, 116805 (2005)
- [88] G. L. Frey, S. Elani, M. Homyonfer, Y. Feldman, and R. Tenne, *Phys. Rev. B* **57**, 6666 (1998)
- [89] Y. Yang, H. E. Unalan, P. Hiralal, K. Chremmou, A. Teh, I. Alexandrou, R. Tenne, and G. A. J. Amaratunga, *In NANO '08. 8th IEEE Conference*, 18–21 Aug, 85 (2008).
- [90] H. E. Unalan, Y. Yang, Y. Zhang, P. Hiralal, D. Kuo, S. Dalal, T. Butler, S. N. Cha, J. E. Jang, K. Chremmou, G. Lentaris, D. Wei, R. Rosentsveig, K. Suzuki, H. Matsumoto, M. Minagawa, Y. Hayashi, M. Chhowalla, A. Tanioka, W. I. Milne, R. Tenne, and G. A. J. Amaratunga, *IEEE Trans. Electron Devices* **55**, 2988 (2008)
- [91] M. Remskar, A. Mrzel, M. Virsek, M. Godec, M. Krause, A. Kolitsch, A. Singh, and A. Seabaugh, *Nanoscale Res. Lett.* **6**, 26 (2011)
- [92] H. Yuan, M. S. Bahramy, K. Morimoto, S. Wu, K. Nomura, B. Yang, H. Shimotani, R. Suzuki, M. Toh, C. Kloc, X. Xu, R. Arita, N. Nagaosa, and Y. Iwasa, *Nature Phys.* **9**, 563 (2013)

- [93] M. Krüger, M. R. Buitelaar, T. Nussbaumer, C. Schönenberger and L. Forró, *Appl. Phys. Lett.* **78**, 1291 (2001)
- [94] M. S. Dresselhaus, and G. Dresselhaus, *Adv. Phys.* **30**, 139 (1981)
- [95] D. van Dirk, and P. Kes, *Physics Today* **63** (9), 38 (2010)
- [96] H. K. Onnes, *Commun. Phys. Lab. Univ. Leiden* 120b (April 1911), reprinted in *Proc. K. Ned. Akad. Wet.* **13**, 1274 (1911)
- [97] "The Nobel Prize in Physics 1913". Nobelprize.org. Nobel Media AB 2014. http://www.nobelprize.org/nobel_prizes/physics/laureates/1913/
- [98] E. Maxwell, *Phys. Rev.* **78**, 477 (1950)
- [99] C. A. Reynolds, B. Serin, W. H. Wright, and L. B. Nesbitt, *Phys. Rev.* **78**, 487 (1950)
- [100] J. Bardeen, L. N. Cooper, and J. R. Schrieffer, *Phys. Rev.* **108**, 1175 (1957)
- [101] W. A. Little, and R. D. Parks, *Phys. Rev. Lett.* **9**, 9 (1962)
- [102] N. Byers, and C. N. Yang, *Phys. Rev. Lett.* **7**, 46 (1961)
- [103] M. Tinkham, *Rev. Mod. Phys.* **36**, 268 (1964)
- [104] B.D. Josephson, *Phys. Lett.* **1**, 251 (1962)
- [105] B. S. Chandrasekhar, *Appl. Phys. Lett.* **1**, 7-8 (1962)
- [106] A. M. Clogston, *Phys. Rev. Lett.* **9**, 266 (1962)
- [107] J. Gittleman, *Phys. Rev.* **92**, 561 (1953)
- [108] R. A. Klemm, A. Luther, and M. R. Beasley, *Phys. Rev. B* **12**, 877 (1975)
- [109] P. Fulde, and R. A. Ferrell, *Phys. Rev.* **135**, A550 (1964)
- [110] A. I. Larkin, and Y. N. Ovchinnikov, *Sov. Phys. JETP* **20**, 762 (1965)
- [111] Y. Matsuda, and H. Shimahara, *J. Phys. Soc. Jpn.* **76**, 051005 (2007)
- [112] Y. Aharonov, and D. Bohm, *Phys. Rev.* **115**, 485 (1959)
- [113] A. Bachtold, C. Strunk, J. Salvetat, J. Bonard, L. Forró, T. Nussbaumer, and C. Schönenberger, *Nature* **397**, 673 (1999)
- [114] B. S. Deaver, Jr. and W. M. Fairbank, *Phys. Rev. Lett.* **7**, 43 (1961)
- [115] R. S. Newbower, M. R. Beasley, and M. Tinkham, *Phys. Rev. B* **5**, 864 (1972)
- [116] N. Giodano, *Physica B* **203**, 460 (1994)
- [117] S. Bose, P. Raychaudhuri, R. Banerjee, P. Vasa, and P. Ayyub, *Phys. Rev. Lett.* **95**, 147003 (2005)
- [118] S. Bose, C. Galande, S. P. Chockalingam, R. Banerjee, P. Raychaudhuri, and P. Ayyub, *J. Phys.: Condens. Matter* **21**, 205702 (2009)
- [119] G. L. Frey, S. Elani, M. Homyonfer, Y. Feldman, and Tenne, R. *Phys. Rev. B* **57**, 6666 (1998)
- [120] L. N. Cooper, *Phys. Rev. Lett.* **6**, 689 (1961)

- [121] J. Simonin, *Phys. Rev. B* **33**, 7830 (1986)
- [122] T. Schneider, Z. Gedik, and S. Ciraci, *Europhys. Lett.* **14**, 261 (1991)
- [123] V. Bruyndoncx, L. V. Look, M. Verschuere, and V. V. Moshchalkov, *Phys. Rev. B* **60**, 10468 (1999)
- [124] L. X. Benedict, V. H. Crespi, S. G. Louie, and M. L. Cohen, *Phys. Rev. B* **52**, 14935 (1995)
- [125] R. Barnett, E. Demler, and E. Kaxiras, *Phys. Rev. B* **71**, 035429 (2005)
- [126] K. G. Petzinger, and B. Tuttle, *Phys. Rev. B* **47**, 2909 (1993)
- [127] N. C. Constantinou, M. Masale, and D. R. Tilley, *J. Phys.: Condens. Matter* **4**, L293 (1992)
- [128] I. Sternfeld, E. Levy, M. Eshkol, A. Tsukernik, M. Karpovski, H. Shtrikman, A. Kretinin, and A. Palevski, *Phys. Rev. Lett.* **107**, 037001 (2011)
- [129] G. L. J. A. Rikken, and E. Raupach, *Nature* **390**, 493 (1997)
- [130] N. Berova, and K. Nakanishi, *Circular dichroism: principles and applications*. (John Wiley & Sons, 2000)
- [131] N. Nagaosa, and Y. Tokura, *Nature Nanotech.* **8**, 899 (2013)
- [132] G. L. J. A. Rikken, J. Fölling, and P. Wyder, *Phys. Rev. Lett.* **87**, 236602 (2001)
- [133] V. Krstić, S. Roth, M. Burghard, K. Kern, and G. L. J. A. Rikken, *J. Chem. Phys.* **117**, 11315 (2002)
- [134] FPop, P. Auban-Senzier, E. Canadell, G. L. J. A. Rikken, and N. Avarvari, *Nature Comm.* **5**: 3757 (2013)
- [135] L. Onsager, *Phys. Rev.* **37**, 405 (1931)
- [136] L. Onsager, *Phys. Rev.* **38**, 2265 (1931)
- [137] P. Kleindienst, and G. H. Wagnière, *Chem. Phys. Lett.* **288**, 89 (1998)
- [138] G. L. J. A. Rikken, and E. Raupach, *Phys. Rev. E* **58**, 5081 (1998)
- [139] G. L. J. A. Rikken and P. Wyder, *Phys. Rev. Lett.* **94**, 016601 (2005)
- [140] M. Musigmann, A. Busalla, K. Blum, and D. G. Thompson, *J. Phys. B: At. Mol. Opt. Phys.* **34** L79 (2001)
- [141] M.E. Pospelov, *Phys. Lett. A* **220**, 194 (1996)
- [142] D. Pekker, G. Refael, and P. M. Goldbart, *Phys. Rev. Lett.* **107**, 017002 (2011)
- [143] T. Morgan-Wall, B. Leith, N. Hartman, A. Rahman, and N. Marković, *Phys. Rev. Lett.* **114**, 077002 (2015)
- [144] S. A. Mills, J. J. Wissner, C. Shen, Z. Xu, and Y. Liu, *Phys. Rev. B* **93**, 224504 (2016)

List of Publications

Original papers

- [1] **F. Qin**, T. Ideue, W. Shi, X. –X. Zhang, M. Yoshida, A. Zak, R. Tenne, T. Kikitsu, D. Inoue, D. Hashizume & Y. Iwasa,
Diameter-Dependent Superconductivity in Individual WS₂ Nanotubes,
Nano Letters **18**, 6789-6794 (2018), [doi: 10.1021/acs.nanolett.8b02647](https://doi.org/10.1021/acs.nanolett.8b02647).
✧ Highlighted by: [Nature Nanotechnology](#).
- [2] **F. Qin**, T. Ideue, W. Shi, Y. Zhang, R. Suzuki, M. Yoshida, Y. Saito & Y. Iwasa,
Electric-field Control of Electronic States in WS₂ Nanodevices by Electrolyte Gating,
Journal of Visualized Experiments **134**, e56862, (2018), [doi:10.3791/56862](https://doi.org/10.3791/56862).
- [3] **F. Qin**, W. Shi, T. Ideue, M. Yoshida, A. Zak, R. Tenne, T. Kikitsu, D. Inoue, D. Hashizume & Y. Iwasa,
Superconductivity in a chiral nanotube.
Nature Communications **8**, 14465 (2017), [doi:10.1038/ncomms14465](https://doi.org/10.1038/ncomms14465).
✧ Highlighted by: [Azonano](#), [Phys.org](#), [Science Alert](#), [Academist Journal](#), [natureasia](#), *Superconductor week*, 日刊工業新聞, 化学工業日報.

Contributing works

- [4] Y. J. Zhang, T. Ideue, M. Onga, **F. Qin**, R. Suzuki, A. Zak, R. Tenne, J. H. Smet & Y. Iwasa,
Enhanced intrinsic photovoltaic effect in tungsten disulfide nanotubes,
Nature **570**, 349–353 (2019), [doi: 10.1038/s41586-019-1303-3](https://doi.org/10.1038/s41586-019-1303-3).
✧ Highlighted by: [Nature](#), [Azonano](#), [Phys.org](#), [AlphaGalileo](#), [Nanowerk](#), [Solar Daily](#), [NOVUS Light](#).
- [5] Y. J. Zhang, M. Onga, **F. Qin**, W. Shi, A. Zak, R. Tenne, J. Smet & Y. Iwasa,
Optoelectronic response of a WS₂ tubular p-n junction,
2D Materials **5**, 035002 (2018), [doi: 10.1088/2053-1583/aab670](https://doi.org/10.1088/2053-1583/aab670).

Curriculum Vitae

秦 峰 **Feng Qin**

Department of Applied Physics and Quantum-Phase Electronics Center (QPEC),
Graduate School of Engineering, the University of Tokyo,
Room 309, Building 8, Hongo 7-3-1, Bunkyo-ku, Tokyo 113-8656, Japan.

Date of Birth: 1991/09/13

Nationality: China

Phone: +81-80-8881-8962

E-mail: qinfeng@mp.t.u-tokyo.ac.jp

Education

- **Ph. D. candidate in Engineering (Applied Physics)** Expected: **March 2020**
Department of Applied Physics, Graduate School of Engineering, University of Tokyo,
“Gate-induced Superconductivity and Nonreciprocal Transport in Chiral Nanotubes”,
Advisor: Prof. Yoshihiro Iwasa.
- **Master degree in Engineering (Applied Physics)** **September 2016**
Department of Applied Physics, Graduate School of Engineering, University of Tokyo,
“Superconductivity in chiral WS₂ nanotube”,
Advisor: Prof. Yoshihiro Iwasa.
- **Bachelor degree in Science (Physics)** **July 2014**
Department of Physics, School of Science, Tsinghua University,
“Antiferromagnet on square-octagon lattice”,
Advisor: Prof. Zhengyu Weng.

Research Interests

- **Condensed matter physics**
Electric double layer transistor, 2D materials and VdW heterostructures, nanotube, superconductivity, nonlinear transport, photovoltaic effect, thermoelectric effect, *etc.*

Awards and Scholarship

- [1] JSPS-DC2 (2018/04-2020/03)
(Research Fellowships for Young Scientists 日本学術振興会特別研究員)
- [2] SEUT-RA Type-A (2017/10-2018/09) and Type-B (2016/10-2017/09)
(Graduate School of Engineering, The University of Tokyo Doctoral Student Special Incentives Program 博士課程学生特別リサーチ・アシスタント)
- [3] Monbukagakusho Honors Scholarship for Privately Financed International Students (2016/04-2017/03) and (2015/10-2016/03)
(文部科学省外国人留学生学習奨励費)
- [4] **Ye Qisun Award (2014)**
(The highest award for distinguished undergraduate students in Department of Physics, School of Science, Tsinghua University)
- [5] **The 1st prize in the 2nd National Competition of Physics Experiment for College Students (2013)**
(One of 3 winners from 92 participators in 46 universities over the China)
- [6] Tsinghua alumni Meng Zhaoying scholarship (2012)
- [7] Individual Scholarship (2012)
- [8] The 2nd prize in the Beijing Competition of Physics Experiment for College Students (2012)
- [9] The 3rd prize in the 3rd China Undergraduate Physics Tournament (2012)
- [10] National Encouragement Scholarship (2011)
- [11] **The 1st prize in the 26th Chinese Physics Olympiad (Finals, 2009)**
(One of 50 candidates for Chinese national team for 41th International Physics Olympiad and 11st Asian Physics Olympiad)